MOLECULAR MECHANISMS OF ENDOCYTOSIS: TRAFFICKING AND FUNCTIONAL REQUIREMENTS FOR THE TRANSFERRIN RECEPTOR, SMALL INTERFERING RNAS AND DOPAMINE TRANSPORTER

A Dissertation Presented

By

DEANNA MARIE NAVAROLI

Submitted to the Faculty of the
University of Massachusetts Graduate School of Biomedical Sciences, Worcester
in partial fulfillment of the requirements for the degree of

DOCTOR OF PHILOSOPHY

April 30, 2012

BIOMEDICAL SCIENCE

Parts of this dissertation have appeared in separate publications:

Navaroli DM, Bellvé KD, Standley C, Lifshitz LM, Cardia J, Lambright D, Leonard D, Fogarty KE, Corvera S. Rabenosyn-5 defines the fate of the transferrin receptor following clathrin-mediated endocytosis. Proc Natl Acad Sci U S A. 2012 Feb 21;109(8):E471-80. Epub 2012 Jan 30. Peer reviewed.

Navaroli DM, Stevens ZH, Uzelac Z, Gabriel L, King MJ, Lifshitz LM, Sitte HH, Melikian HE. The plasma membrane-associated GTPase Rin interacts with the dopamine transporter and is required for protein kinase C-regulated dopamine transporter trafficking. J Neurosci. 2011 Sep 28;31(39):13758-70.

Navaroli DM, Melikian HE. Insertion of tetracysteine motifs into dopamine transporter extracellular domains. PLoS One. 2010 Feb 9;5(2):e9113.

MOLECULAR MECHANISMS OF ENDOCYTOSIS: TRAFFICKING AND FUNCTIONAL REQUIREMENTS FOR THE TRANSFERRIN RECEPTOR, SMALL INTERFERING RNAS AND DOPAMINE TRANSPORTER

A Dissertation Presented

By

DEANNA MARIE NAVAROLI

The signatures of the Dissertation Defense Committee signifies completion and approval as to style and content of the Dissertation

_____

Silvia Corvera, M.D., Thesis Advisor

_____

Eric H. Baehrecke, Ph.D., Member of Committee

_____

Michael P. Czech, Ph.D., Member of Committee

_____

Timothy E. McGraw, Ph.D., Member of Committee

_____

Gregory J. Pazour, Ph.D., Member of Committee

The signature of the Chair of the Committee signifies that the written dissertation meets the requirements of the Dissertation Committee

_____

David Lambright, Ph.D., Chair of Committee

The signature of the Dean of the Graduate School of Biomedical Sciences signifies that the student has met all graduation requirements of the school.

_____

Anthony Carruthers, Ph.D.,
Dean of the Graduate School of Biomedical Sciences

Interdisciplinary Graduate Program

April 30, 2012

DEDICATION

To my loving grandparents, the people I take after most, you are always with me.

Bruno Navaroli
November 20, 1916 – November 11, 1999

Loreta (Marchetti) Navaroli
September 16, 1920 – April 4, 2004

To my amazing parents Rosalyn (Hemingway) Navaroli & Joseph Navaroli, thank you so much for all of the ways in which you have supported me through the years. Even when you did not understand or necessarily agree with my choices, you allowed me to find my own path. If every child had parents like you, what an amazing world this would be.

ACKNOWLEDGEMENTS

To my mentor, Silvia Corvera, thank you for giving me the opportunity to work in your laboratory, independently exploring this project. Thank you for applauding my successes, helping me to address and fix my failures, encouraging me, and helping me to grow as a scientist.

I would like to thank members of the Corvera and Czech laboratories, both past and present, for your helpful discussions, collaborations, and friendship. Research is always a team effort and your support, guidance, shared reagents, and helping hands were greatly appreciated throughout my graduate studies.

To my thesis committee, it has been such a pleasure to have an accomplished group of scientists show such enthusiasm about my research. I am grateful for your feedback, guidance, and encouragement.

To the biomedical imaging department, especially, Kevin Fogarty, Karl Bellvé, Clive Standley, and Larry Lifshitz, it is thanks you to that I had the technology with which to explore these research studies. Many aspects of this project could not have been investigated without you.

We have the most amazing administrative assistant. Darla Cavanaugh, thank you for bringing so much light to our graduate program. You take so much time to know each and every one of us personally and it is always a pleasure to see and talk to you. The well-organized way in which you keep our program running smoothly takes a great deal of weight off of our shoulders. We are very blessed to have you.

To my cousin and Godmother, Donna Sciabarrasi Conlon, thank you for showing me your love and passion for science. You gave me the greatest support and encouragement in pursuing this degree and career path.

Dr. Teresa Barlozzari, thank you for your inspiration, to be the best that I can be and to share what I learn with others. From day one, you showed me that work can be something to look forward to and a place where amazing people, and science, can be found.

An extra special thank you to those friends and family dearest to me. It is through your love, encouragement, and faith that I found the desire to continue with this degree. I have always been able to depend on you, your constant encouragement, love, and friendship through the years. The Lord has blessed me through all of you, may those blessings return to you a thousand fold. ΙΧΘΥΣ for abounding grace, truth, love, peace, comfort, faithfulness, and guidance as I find my path in life.

ABSTRACT

Endocytosis is an essential function of eukaryotic cells, providing crucial nutrients and playing key roles in interactions of the plasma membrane with the environment. The classical view of the endocytic pathway, where vesicles from the plasma membrane fuse with a homogenous population of early endosomes from which cargo is sorted, has recently been challenged by the finding of multiple subpopulations of endosomes. These subpopulations vary in their content of phosphatidylinositol 3- phosphate (PI3P) and Rab binding proteins. The role of these endosomal subpopulations is unclear, as is the role of multiple PI3P effectors, which are ubiquitously expressed and highly conserved. One possibility is that the different subpopulations represent stages in the maturation of the endocytic pathway. Alternatively, endosome subpopulations may be specialized for different functions, such as preferential trafficking of specific endocytosed cargo. To determine whether specific receptors are targeted to distinct populations of endosomes, we have built a platform for total internal reflection fluorescence (TIRF) microscopy coupled with structured illumination capabilities named TESM (TIRF Epifluorescence Structured light Microscope). In this study, TESM, along with standard biochemical and molecular biological tools, was used to analyze the dynamic distribution of two highly conserved Rab5 and PI3P effectors, EEA1 and Rabenosyn-5, and systematically study the trafficking of transferrin. Rabenosyn-5 is necessary for proper expression of the transferrin receptor as well as internalization and recycling of transferrin-

transferrin receptor complexes. Results of combining TIRF with structured light Epifluorescence (SLE) indicate that the endogenous populations of EEA1 and Rabenoysn-5 are both distinct and partially overlapping.

The application of antisense oligonucleotides as potential therapeutic agents requires effective methods for their delivery to the cytoplasm of target cells. In collaboration with RXi Pharmaceuticals we show the efficient cellular uptake of the antisense oligonucleotide sd-rxRNA® in the absence of delivery vehicle or protein carrier. In this study TIRF, SLE, and biochemical approaches were utilized to determine whether sd-rxRNA traffics and functions along specific endosomal pathways. Sd-rxRNA was found to traffic along the degradative pathway and require EEA1 to functionally silence its target. These new findings will help define the cellular pathways involved in RNA silencing.

Neurotransmitter reuptake and reuse by neurotransmitter transport proteins is fundamental to transmitter homeostasis and synaptic signaling. In order to understand how trafficking regulates transporters in the brain and how this system may be disregulated in monoamine-related pathologies, the transporter internalization signals and their molecular partners must be defined. We utilized a yeast two-hybrid system to identify proteins that interact with the dopamine transporter (DAT) endocytic signal. The small, membrane associated, GTPase Rin was determined to specifically and functionally interact with the DAT endocytic signal, regulating constitutive and protein kinase C (PKC) – stimulated DAT endocytosis. The results presented in this study provide new insights into

functions and components of endocytosis and enhance the understanding of endocytic organization.

TABLE OF CONTENTS

LIST OF FIGURES

LIST OF TABLES

ABBREVIATIONS

ADHD	Attention Deficit Hyperactivity Disorder
Ago2	Argonaute-2
APPL1	Adaptor protein phosphotyrosine interaction
Baf	Bafilomycin A1
CaMKII	Calcium/calmodulin-dependent kinase II
CCPGCC	Tetracysteine
Clath	Clathrin
CNS	Central nervous system
DA	Dopamine
DAT	Dopamine transporter
DOG	Difference of Gaussians
dsRNA	Double stranded RNA
EEA1	Early endosomal autoantigen 1
EGF	Epidermal growth factor
EGFR	Epidermal growth factor receptor
EHD	Eps homology domain
EL	Extracellular loop
Epi	Epifluorescence
ESCRT	endosomal sorting complex required for transport
ESL	Epifluorescence Structured Light
FRET	Fluorescence Resonance Energy Transfer
GAP	GTPase activating protein
GEF	Guanine nucleotide exchange factors
H^+	Hydrogen
^3H	Tritium
Hrs	Hepatocyte growth factor-regulated tyrosine kinase substrate
LDL	Low-density lipoprotein
LDLR	Low-density lipoprotein receptor
M4K4	MAP4Kinase4
MIP	Maximum intensity pixel
miRNA	Micro RNA
mRNA	Messenger RNA
MVB	Multivesicular body
P-body	Processing body aka GW-body
PH	Pleckstrin homology
PI(3)P	Phosphatidylinositol 3-phosphate
PKC	Protein Kinase C
PX	PHOX homology
Rbsn	Rabenosyn-5
Rin	Ras-like in neurons
RISC	RNA induced silencing complex
RNAi	RNA interference

SARA	Smad2 Anchor for Receptor Activation
Sc	Scrambled siRNA oligonucleotide
shRNA	Short hairpin RNA
Si	siRNA oligonucleotide
SID-1	Systemic RNAi defective-1
siRNA	Small interfering RNA
TESM	TIRF Epifluorescence Structured light Microscope
tetraCys	Tetracysteine
TIRF	Total Internal Reflection Fluorescence
Tf	Transferrin
TfR	Transferrin receptor
UTR	Untranslated region
WDFY2	WD repeat and FYVE domain-containing protein 2

PREFACE

The majority of the work presented in Chapter II has been published in a peer-reviewed journal (Navaroli *et al*. 2012). TIRF Epifluorescence Structured Illumination Microscope (TESM) optical system and imaging hardware and software were designed by Drs. Clive Standley and Karl Bellvé, respectively. Calibration of z-map position from dual and tri labeled beads was performed by Kevin Fogarty. The kinetic model curves of ratio data and rates was fit and generated by Kevin Fogarty. Data Analysis and Visualization Environment (DAVE) software platform developed and maintained by Dr. Lawrence Lifshitz. Rabenosyn-5 rescue experiments were performed by Dr. Deborah Leonard. Protein for antibody production was provided by Dr. David Lambright. Rabenosyn-5 and EEA1 siRNA oligos were designed by Dr. James Cardia.

The experimental work in Chapter III is being prepared as a manuscript for publication at the time of this thesis preparation. MAP4K4 qRT-PCR was performed by Dr. Matthieu Prot. Sd-rxRNA oligos were designed and provided by RXi Pharmaceuticals.

The work presented in Chapter IV has been published in a peer-reviewed journal (Navaroli & Stevens *et al*. 2011). Dr. Haley Melikian performed the yeast 2-hybrid screen and *in vitro* GST pulldowns. Zeljko Uzelac and Dr. Harald Sitte performed FRET studies and analysis. Immunofluorescence was performed by Zachary Stevens. Zachary Stevens, Luke Gabriel, and Michael King performed internalization and dopamine uptake assays. Dr. Lawrence Lifshitz assisted statistical analysis of DAT and Rin colocalization.

The work presented in the Appendix has been published in a peer-reviewed journal (Navaroli & Melikian 2010).

CHAPTER I

INTRODUCTION

The internalization and subsequent sorting of endocytosed macromolecules is an important determinant in processes like cellular development, immunological response, neurotransmission, cell-cell communication, signal transduction and homeostasis [1,2]. Uptake into cells can be classified based on the type of internalization including pinocytosis, phagocytosis, clathrin-mediated and clathrin-independent endocytosis and endocytosis through lipid rafts. Eukaryotic cells are highly compartmentalized structures with functionally distinct membrane-bound compartments. Proteins and other macromolecules are targeted to specific intracellular routes through plasma membrane-derived transport vesicles that are directed to recycling or degradation compartments. For example, the epidermal growth factor (EGF) receptor (EGFR), upon binding its ligand, EGF, is internalized and shuttles through the early endosome to lysosomes for degradation. Conversely, the transferrin (Tf) receptor (TfR) is constitutively internalized through the early endosome to the recycling endosome and back to the cell surface. Therefore, the intracellular fate of a protein molecule is primarily dictated by its endocytic route. The mechanism by which these sorting decisions are made is an

important question in membrane trafficking with implications for understanding pathogen invasion of host cells.

Aberrant trafficking and disease

The endocytosis and trafficking of membranes and proteins is a fundamental cellular process that impacts human diseases. Mutations that affect trafficking of receptors are associated with disease, for example mutations in the low-density lipoprotein (LDL) receptor (LDLR) that impair its function lead to familial hypercholesterolemia [3,4]. LDL is the carrier by which cholesterol is safely transported through the circulatory system. High blood cholesterol levels increase the formation of arterial plaques that cause heart attacks and stroke thereby necessitating the removal of excess cholesterol from circulation. High affinity for LDL as well as the ability to internalize and recycle LDL renders the LDLR essential for the cellular metabolism of cholesterol. At the cell surface, the LDLR binds LDL from the blood plasma at neutral pH (7.4). Once internalized, the acidic pH of endosomes (5.5) causes release of the LDL from its receptor. The receptor recycles to the plasma membrane while the LDL is degraded [5]. Patients with familial hypercholesterolemia suffer from early onset coronary heart disease and atherosclerosis [6]. The J D mutation, a class IV mutation found in familial hypercholesterolemia patients, in the LDLR is a single tyrosine to cysteine point mutation at position 807 of the cytoplasmic domain of the receptor. This mutation inhibits the recruitment of clathrin and prevents the endocytic

machinery from interacting with the receptor thereby impeding LDLR-LDL internalization [7]. Aberrant transport processes are found in a number of other diseases such as tuberculosis infection [8], non-insulin dependent diabetes mellitus [9], Alzheimer's disease [10], and cancer [11,12].

Small GTPases

Two fundamental molecules in endocytic trafficking are small molecular weight GTP-binding proteins (GTPases) and phosphoinositides [13-17]. The nature of these molecules bring both molecular specificity and plasticity to endosomal membranes, thereby distinguishing various endocytic membranes and allowing endocytic material to traffic to specific cellular destinations (Figure 1.1). Small GTPases act as molecular switches regulating the steps involved in vesicle carrier formation, movement, and fusion with target membranes. GTP binding proteins cycle between the GDP-bound inactive state and the GTP-bound active state. This process is catalyzed by guanine nucleotide exchange factors (GEFs) and GTPase-activating proteins (GAPs), respectively, and allows for the activation of GTPases specifically at sites where their function is required. Members of the Rab family of small GTPases are master regulators of protein trafficking that coordinate vesicular transport between different endocytic organelles. Distinct Rab proteins have been identified that are specifically associated with a particular organelle or pathway. These small GTP binding proteins regulate vesicular membrane transport in both the endo- and exo-cytic

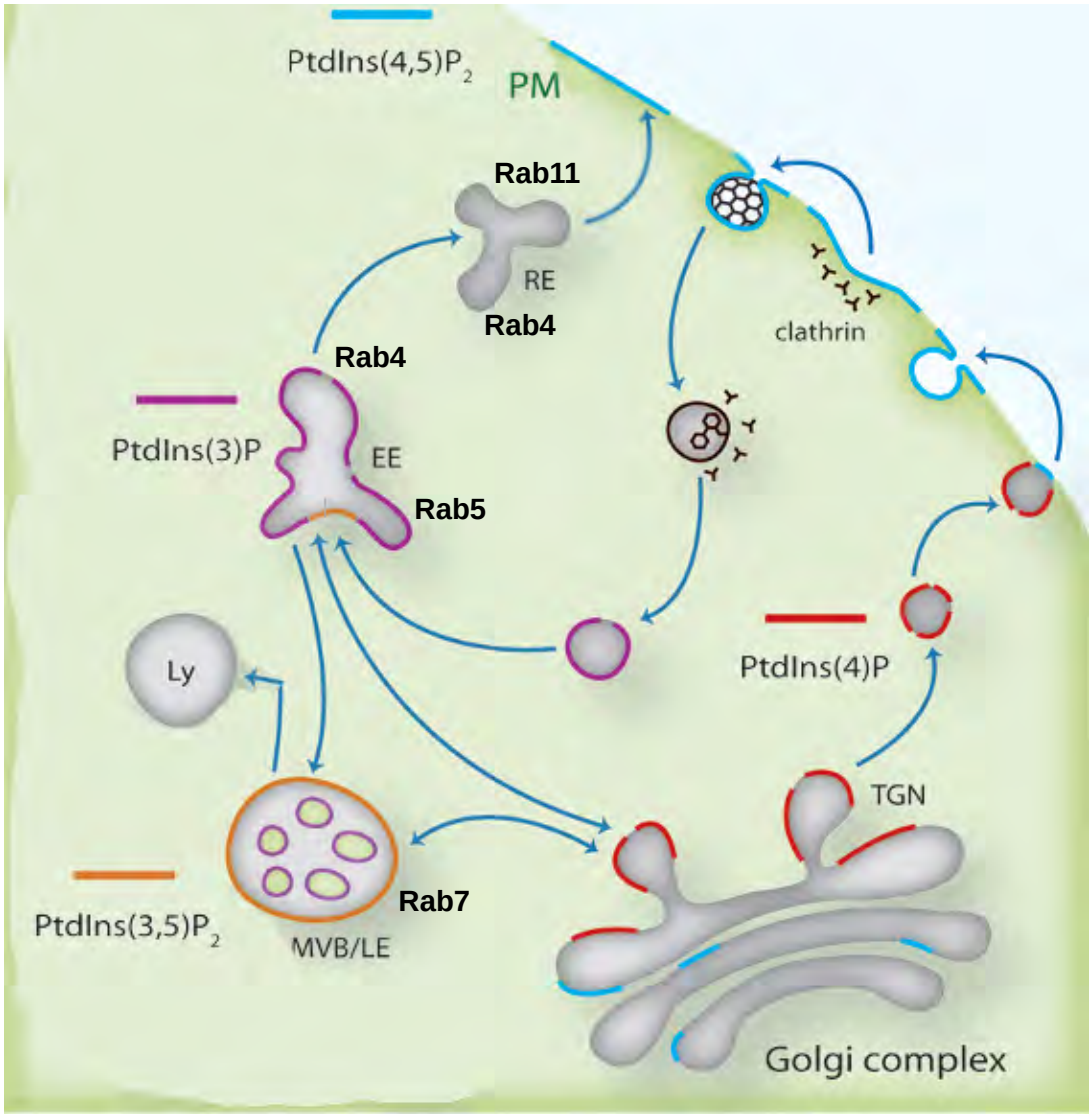

Figure 1.1. Organelle specific distribution of Rab proteins and phosphoinositides. PI(4)P is present at the Trans Golgi Network (TGN) and plasma membrane. PI(4,5)P_2 is present on the plasma membrane (PM) and on invaginating clathrin-coated pits. PI(3)P is specifically present on early endosomes (EE). PI(3,5)P_2 is present on late endosomes (LE). Rab5 and Rab4 are localized to early endosomes. Recycling endosomes (RE) are a collection of Rab4 and Rab11 positive tubules. Late endosomes are recognized by the presence of Rab7. Figure modified from **Vicinanza *et al.* Cell Mol Life Sci. 2008 Sep;65(18):2833-41. Review.**

pathways. Their active forms serve in cargo selection as well as in the formation of scaffolds for vesicle budding, cytoskeletal transport, and targeted membrane fusion. For instance, Rab5 is localized to early endosomes and is essential for plasma membrane to early endosomal transport as well as early endosome fusion [18-21], while Rab7 regulates the transport from early to late endosomes and from late endosomes to lysosomes, and Rab11 is enriched in recycling endosomes [17,22] while Rab4 controls recycling from the early endosome directly to the plasma membrane [23-25]. Three major populations of early endocytic Rab microdomains have been observed by electron and fluorescent microscopy [26]. These three domains are Rab5 positive, Rab5/Rab4 positive, and Rab4/Rab11 positive and are the major regulators of the endocytic recycling pathway [26].

Specific kinases can phosphorylate phosphatidylinositol at the 3, 4, or 5 positions of the inositol ring to generate different phosphoinositide species. Phosphoinositide species are relegated to distinct subcellular compartments through both localized synthesis and rapid turnover, brought about through specific kinases and phosphatases, respectively [27,28]. Different phosphoinositide species bind specific phosphoinositide binding domains including FYVE, pleckstrin homology (PH), and PHOX homology (PX) domains. Found in 40 mammalian proteins, several of which are implicated in membrane trafficking [29], the conserved FYVE domain was named after the first four proteins discovered to contain this motif: Fab1, YOTB, Vac1, and EEA1 [30].

The FYVE domain is characterized for its ability to bind PI3P, the phospholipid enriched on early endocytic membranes. Phosphoinositides function as cellular compartment identifying molecules while also providing the means to alter compartment identity. Other proteins facilitate the spatial and temporal regulation of phosphoinositide conversion. For example, Rab5 regulates phosphatases that convert PI(4,5)P_2, on vesicles internalized from the plasma membrane, to phosphatidylinositol 3-phosphate (PI(3)P) on early endosomes [31]. This process facilitates membrane transport while maintaining compartment identity.

Rab5 effector proteins

The function of Rab5 in regulating organelle motility and fusion between clathrin coated vesicles and early endosomes (heterotypic fusion) and fusion between early endosomes (homotypic fusion) occurs through recruitment of effector proteins. In many cases Rab effector proteins are evolutionarily conserved such as the mammalian Rab5 effectors Rabenosyn-5 and EEA1 [32]. Upon Rab5 activation, its effector hVps34 results in localized production of PI(3)P. The increase in PI(3)P concentration through its synthesis by the Rab5 effector hVps34, a class III PI3-kinase [15,33], generates the lipid environment necessary for the recruitment of downstream effector proteins containing FYVE or PX domains such as EEA1 [30,34], Rabenosyn-5 [32], and Rabankyrin-5 [35-37], that can interact with PI(3)P on endosomal membranes [38-40]. The

concomitant presence of activated Rab5 and PI(3)P is essential for recruitment of FYVE-finger domain containing Rab5 effectors and tethering factors like EEA1 and Rabenosyn-5 which require PI(3)P for localization and subsequent recruitment of SNARE proteins for fusion of endosomal vesicles [32,41,42]. These complexed local events provide the functional platform for homotypic and heterotypic fusion events and the presence of numerous effector proteins with multiple Rab binding capabilities may provide a mechanism for sorting internalized cargo to distinct cellular compartments. In conjunction with the FYVE-finger containing PI(3)P effector Smad2 Anchor for Receptor Activation (SARA), a functional platform is generated which mediates signal transduction events. SARA, by interacting with internalized TGFβ-Receptor-II, is necessary to phosphorylate Smad2, subsequently propagating the TGFβ signal. [43].

EGFR and TfR trafficking

Current models of endocytic trafficking suggest that internalized cargo (receptors, nutrients, pathogens, growth factors) is incorporated into vesicles formed at the plasma membrane. These vesicles may form via clathrin or non-clathrin mediated endocytosis. Once internalized, these cargo-containing vesicles fuse with a homogenous population of early endosomes marked by EEA1. The early endosome is the intracellular location at which cargo is then sorted for lysosomal degradation or delivery to the plasma membrane [44-48]. TIRF microscopy, in conjunction with molecular and biochemical techniques,

were utilized by our laboratory to examine the sorting and early stages of endocytosis of two classically trafficking ligands, EGF and Tf, to determine the mechanism by which these molecules sort to their respective fates at the level of the early endosome [49]. The EGFR is a transmembrane glycoprotein receptor widely expressed in many cells types and responsible for growth, proliferation, differentiation, and other biological responses [12,50-53]. EGF ligand binding to the EGFR induces receptor dimerization and activates EGFR through tyrosine transphosphorylation [54] and stimulates its internalization. Activated EGF-EGFR complexes are trafficked through a series of endocytic compartments and finally the lysosome for degradation [2,55,56]. Studies on the TfR, with its unique internalization and recycling, have advanced understanding of the intricacies of the sorting pathways of endocytosed molecules. Cells utilize the iron bound to Tf circulating in blood plasma upon Tf internalization. At neutral extracellular pH (7.4), di-ferric-Tf binds to its receptor, internalizes through clathrin coated pits, and fuses with an endosome. The acidic environment of the endosome (pH 5.5) causes the release of iron from the Tf while the apo-Tf remains bound to its receptor [57]. The intact apoTf-TfR complex is efficiently recycled from endosomes to the cell surface via the juxtanuclear recycling endosome or by direct recycling from early endosomes [58] where, at neutral pH, apo-Tf is released and the TfR is free to bind more di-ferric-Tf [59]. Wortmannin treatment results in partial inhibition of TfR recycling [60,61] possibly because the recycling endosomal pathway requires PI3-K while the fast recycling pathway does not.

The endocytic system is energetically essential. Cells internalize greater than 25% of their plasma membrane per hour [62]. Tf cycles from and back to the extracellular space in 2-3 minutes [63] and more LDL particles are internalized from the extracellular space and degraded than can be accounted for by new LDLR protein synthesis [64]. Thus the endocytic system allows for the remodeling and reuse of membranes that could not be otherwise reconstituted by de novo synthesis.

Under physiological conditions, simultaneous addition of EGF and Tf to COS cells resulted in low levels of associated cargo molecules as observed by TIRF microscopy [49]. EGF and Tf bind to their receptors located in distinct plasma membrane regions and are incorporated into different endocytic vesicles [49]. EGF enters the cell through small, peripheral structures (Figure 1.2). The internalized EGF rapidly and specifically associates with EEA1 within 4-5 minutes of EGF addition to cells regardless of signal intensity (Figure 1.3B) [49]. In contrast, Tf enters the cell through concentrated patches found throughout the cell membrane in addition to areas of diffuse signal and rapidly traffics to the juxtanuclear region (Figure 1.2). These results strongly indicate that different machineries exist to control internalization and sorting occurs not only at the level of the endosome, but also the plasma membrane [49]. These and other findings support the notion that endosomes exist as functionally distinct heterogeneous populations [26,65-67]. It has been suggested that PI3K utilizes different effectors at apical and basolateral endosomes in polarized cells [68]. In

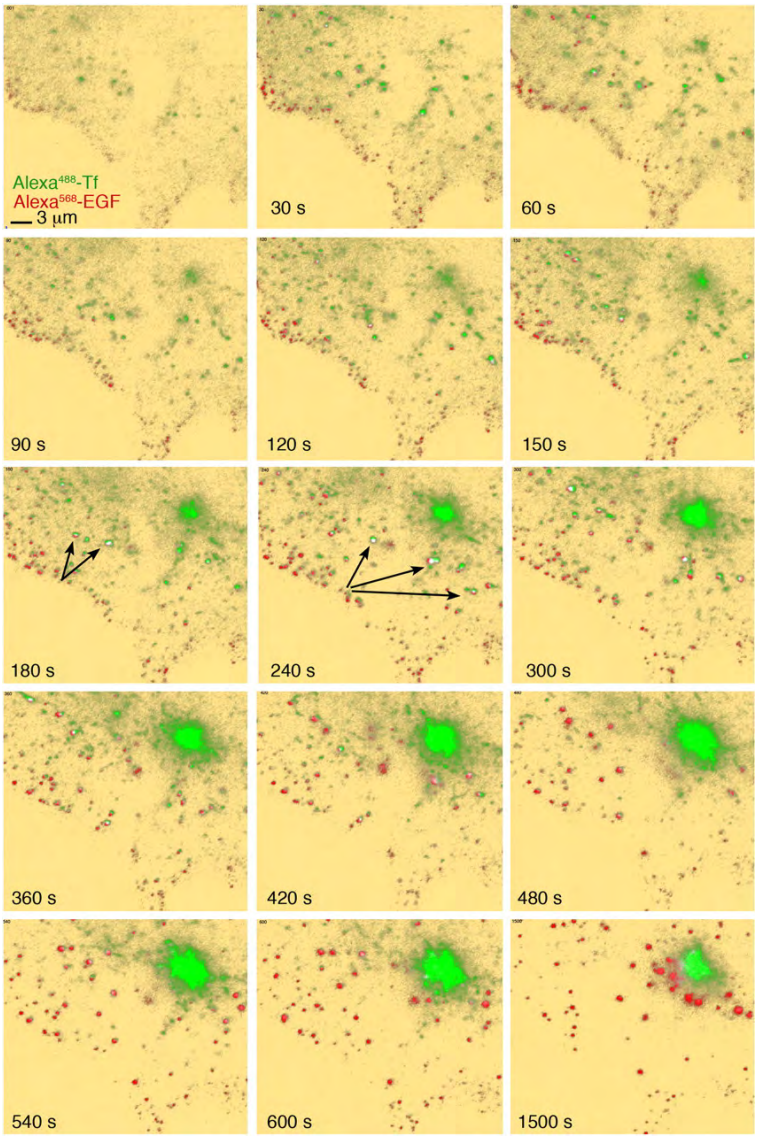

Figure 1.2. Binding and internalization of EGF and Tf in COS-7 cells. COS-7 cells grown on coverslips were placed in KRH buffer at 35°C, and exposed to 50ng/ml Alexa-Fluor^{568}-EGF and 20µg/ml Alexa-Fluor^{488}-Tf. Image capture was started immediately after ligand addition. Background is pseudo colored in yellow to enhance low level signal. Colocalized signal (arrows) is pseudo colored in white. Figure from **Leonard D et al. J Cell Sci 2008;121:3445-3458.**

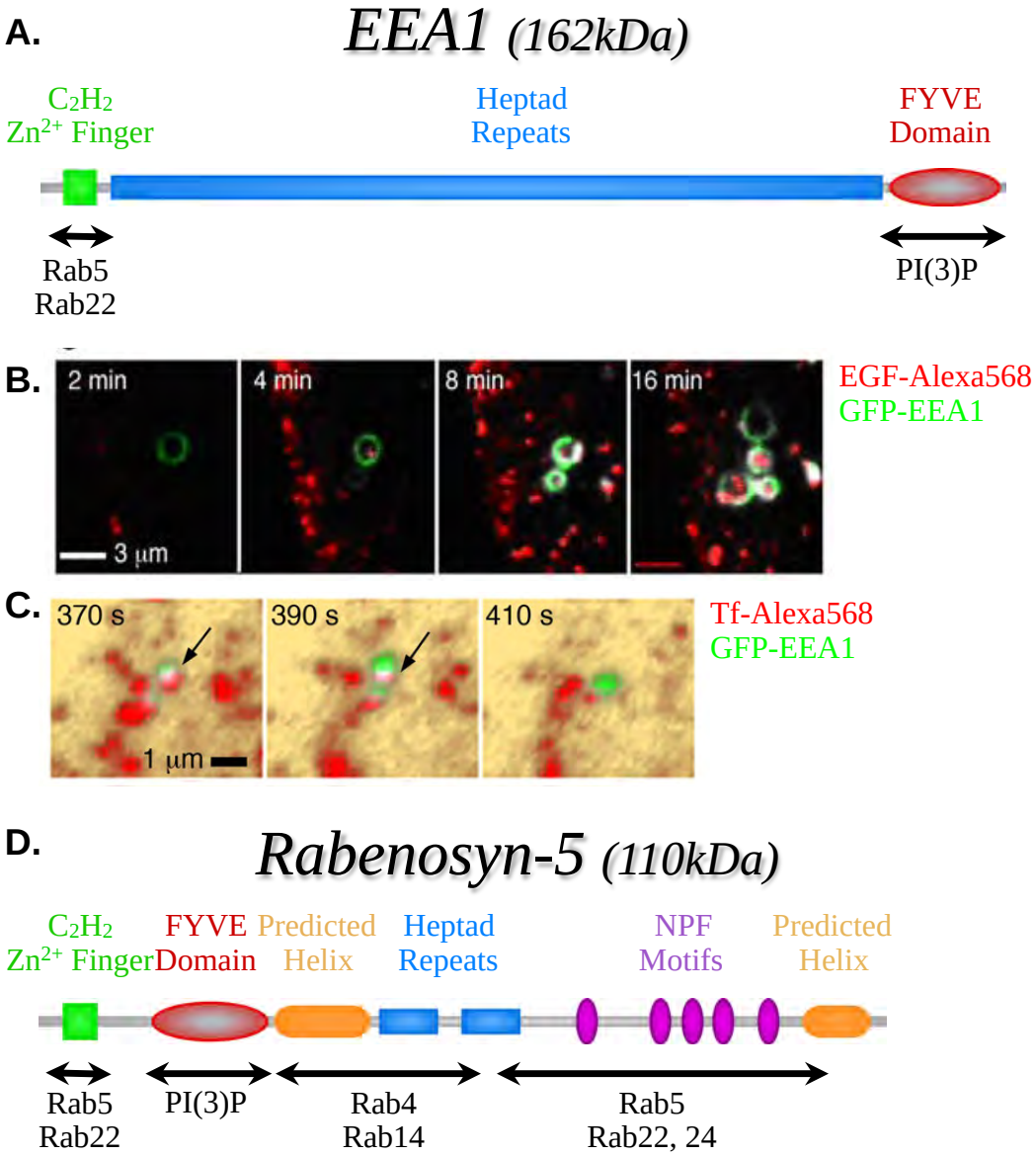

Figure 1.3. EEA1 and Rabenosyn-5 schematic. **A.** Topology and selected effector binding regions of EEA1. **B.** COS-7 cells expressing GFP-EEA1 were imaged by TIRF microscopy during continuous incubation with 50ng/ml Alexa^{568}-EGF for the times indicated. Depicted is the specific colocalization of EGF with EEA1. Image from **Mechanisms of Endocytic Sorting: a dissertation by Deborah Marie Leonard 2006**. **C.** COS-7 cells expressing GFP-EEA1 were imaged by TIRF microscopy during continuous incubation with 10μg/ml Alexa^{568}-Tf for the times indicated. Depicted is the transient nature of the colocalization of Tf with EEA1. Image from **Leonard *et al*. J Cell Sci 2008;121:3445-3458.** **D.** Topology and selected effector binding regions of Rabenosyn-5.

polarized *Drosophila* wing cells, Rabenosyn-5 is required for the formation of actin bundles at the apical membrane, while in the basolateral region it is required for the formation of large endosomes [68]. In MDCK cells, EEA1 is found localized to basolateral endosomes where it may confer directionality of fusion events [69] suggesting functional differences between endosomal populations.

Given that Tf-TfR containing vesicles do not show a rapid, specific interaction but rather a minor transient association with EEA1 (Figure 1.3C) [49] and only 20% localization with WDFY2, another PI(3)P binding FYVE domain protein localized to endosomes proximal to the plasma membrane [65], we chose to examine the role of another FYVE domain protein in early endocytosis, Rabenosyn-5 (Figure 1.3D). Rabenosyn-5 has been suggested to interact with Eps homology domain (EHD) proteins and promote endosomal recycling to the plasma membrane, however its role in endocytosis has not been investigated [70]. Given that Rabenosyn-5 is first recruited through its Rab5 and FYVE binding domains, this data suggests that Rabenosyn-5 has the potential to be recruited to early endosomes where it receives cargo then transitioned to the endocytic recycling compartment. Specifically Rabenosyn-5 has been implicated in bridging the transition from Rab5 to Rab4 compartments in the recycling of the TfR [41]. Given that Rabenosyn-5 is an effector protein capable of forming multivalent interactions and that transport of cargo along the endocytic pathway could be mediated by coordinated and sequential action of discrete Rab

membrane domains, Rabenosyn-5 may help to coordinate the transport of cargo along the endocytic recycling pathway.

High resolution population based studies

In recent years, microscopy techniques such as TIRF have allowed simultaneous imaging of two fluorophores in real time. TIRF has been particularly important in elucidating cellular processes of endo- and exocytosis. With the advent of TIRF, for the first time, an approximately 300nm depth from the coverslip could be selectively illuminated without exciting fluorophores in the entire three dimensional volume of the cell [71]. The caveats of TIRF microscopy systems are 1) that most offer two wavelength excitation and 2) positional relationships between structures cannot be determined. Due to the former caveat, the systematic analysis of multiple endosomes with respect to a ligand or multiple ligands with respect to endosomes has been absent. The latter caveat is a result of the brightness of an object in the TIRF zone being due to either its size or its distance from the coverslip.

While high capture rates and non-invasive imaging makes wide field fluorescence light microscopy highly advantageous, a disadvantageous aspect of light microscopy is the limitation imposed by the diffraction limit of light. Light can only be focused to a diameter of approximately half the wavelength of the emitted light. Visible light wavelengths range from 400-700nm meaning the diffraction limit for imaging under these conditions is 200-350nm. With the diffraction limit of

approximately 200nm, significantly larger than subcellular structures, multiple objects less than 200nm apart appear as one. Thus, in order to visualize and systematically analyze the transfer of endocytic cargo from one compartment to another within the early endocytic pathway we developed a three fluorophore TIRF system. To provide the spatial resolution required to identify the topological organization of endocytic intermediates or compartments involved in cargo transfer, we coupled epifluorescence structured light (ESL) to this TIRF system. Structured-illumination microscopy is a method of wide field fluorescence microscopy that achieves resolution beyond the diffraction limit of light [72]. By combining TIRF and ESL we will be able to determine the position of endosomes relative to the cell surface. The microscopy platform we have developed allows the detection of the precise position of endosomes relative to the plasma membrane during the uptake of cargo. Axial resolution is maximized by concurrently applied TIRF and ESL allowing us to address the fundamental question of whether different internalization mechanisms deliver cargo into distinct subsets of early endosomes. Chapter 2 utilized this new microscopy platform, TESM (TIRF Epifluorescence Structured light Microscope, illustrated in Figure 1.4), to investigate the endocytosis of the transferrin receptor with respect to endocytic domains in real time.

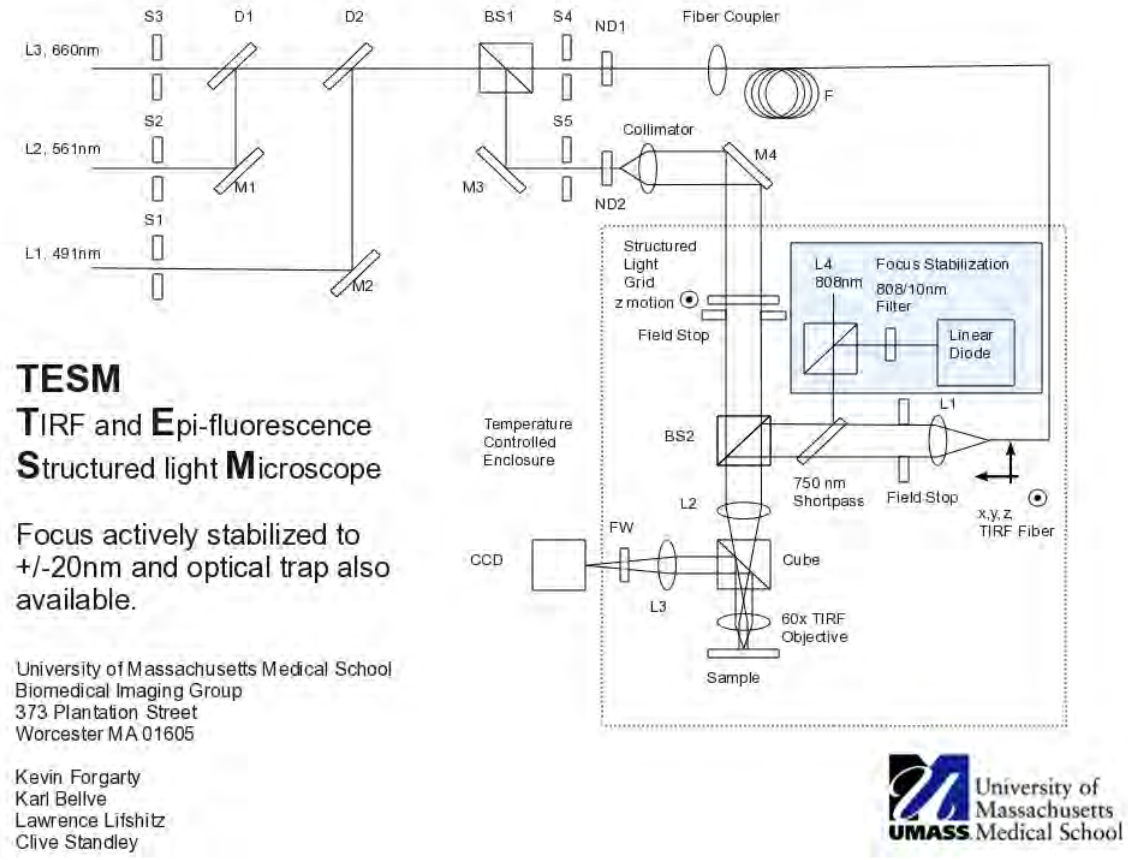

Figure 1.4. Overview and schematic of TIRF and Epifluorescence Structured light Microscope (TESM). Instrument layout showing four lasers (L1, 491nm; L2, 561nm; L3, 660nm; L4, 808nm), shutters (S1, S2, S3, S4) mirrors (M1, M2, M3, M4) and dichroic mirrors (D1, D2), beam splitters (BS1, BS2), neutral density filters on the TIRF beam path (ND1) and the epifluorescence beam path (ND2), lenses (L1, L2, L3), and filter wheel (FW).

Trafficking of self-delivering small interfering RNA

RNA interference (RNAi) is a naturally occurring cellular process in eukaryotes affecting post-transcriptional gene silencing. The multi-step RNAi pathway is initiated by double stranded RNA (dsRNA) and results in sequence-specific mRNA degradation. A crucial component of the immune response to foreign genetic material such as bacteria and viruses is RNAi. The endosomal pathway could link RNAi machinery to innate immunity. Non-cell autonomous gene silencing is a novel mechanism of intracellular communication and, potentially, viral defense that requires RNAi silencing signals to travel between cells. Many [73-75] but not all [76,77] organisms can communicate RNAi silencing between cells. One possible evolutionary advantage of systemic RNAi is an antiviral defense. It is known that systemic RNAi acts as an antiviral defense mechanism in plants and recently HIV-1 was shown to elicit nucleic acid-based immunity in human cells [78]. In addition to the naturally occurring process, short duplexes (21 nucleotides) of chemically synthesized siRNAs introduced into mammalian cells also result in efficient sequence-specific gene silencing [79]. Conversely, long dsRNA, those greater than 30 nucleotides, elicit an interferon mediated anti-viral response in mammalian cells [80]. The ability of siRNA to induce targeted silencing of genes has the potential to be harnessed to treat human diseases by specifically silencing genes that lead to disease.

Challenges to any RNAi therapeutic model include successful delivery and entry of siRNAs into a cell type of interest. RXi Pharmaceuticals developed a

novel class of self delivering RNAi compounds (sd-rxRNA®) that do not require a delivery vehicle for cellular uptake. Sd-rxRNA is a hydrophobically modified hybrid of conventional RNAi and antisense compounds resulting in a unique class of RNAi compounds with improved drug-like properties compared to traditional siRNAs with the potential to be utilized as therapeutics. A detailed understanding of the mechanism of sd-rxRNA uptake will allow the development of RNAi compounds that target tissues of interest with efficient intracellular uptake. Within Chapter 3 I investigate the endocytic route utilized by sd-rxRNA following exposure to cells and components of the endocytic pathway required for functional silencing by targeted sd-rxRNA.

Molecular mechanisms of dopamine transporter trafficking

Dopaminergic neurotransmission plays a pivotal role in motor control, cognition, and rewarding behaviors in the central nervous system. Synaptic dopamine (DA) levels are stringently controlled by DA reuptake mediated by the sodium- and chloride- dependent plasma membrane DA transporter (DAT). DAT is potently inhibited by psychostimulants, and blocking DA uptake with these agents increase extracellular DA levels and enhances postsynaptic signals [81,82]. Consequently, the number of active DATs at the plasma membrane is directly linked to the efficacy of DA signaling and psychoactive drug targeting. Extensive evidence demonstrates that DAT is not a static membrane protein; rather, it robustly traffics to and from the cell surface via the endocytic pathway

[83-86]. Moreover, DAT surface levels are dynamically regulated by altering transporter trafficking kinetics through both protein kinase C (PKC) activation and exposure to amphetamine [81,87-89]. To date, the molecular mechanisms governing DAT endocytic trafficking are not well defined.

We recently reported that DAT carboxy terminal residues 587-596 encode endocytic signals required for basal and PKC-accelerated DAT endocytosis [90,91]. We sought to identify proteins that interact with the DAT endocytic signal and may play a role in basal and PKC-accelerated DAT internalization. We utilized the hSOS rescue yeast two-hybrid system, which allows bait-target interactions at or near the plasma membrane, mimicking the expected interactions of proteins with DAT during endocytic events. Using the DAT 587-596 domain as bait in a screen against the human substantia nigra library, we identified the small plasma membrane associated GTPase, Rin/Rit2, as a candidate DAT-interacting protein. Rin is a 25kDa GTPase that directly binds the C-terminal domain of calmodulin and may play a role in activation of PKC through interactions with the PDZ binding domain of Par6 [92,93]. Given that DAT activity is regulated by both PKC and CamKII [94], and that Rin is coupled to both of these pathways, it is likely that Rin could play a role in PKC-regulated DAT trafficking. As discussed in Chapter 4, cellular, in vitro, and biochemical approaches were utilized to investigate the role of Rin in DAT trafficking.

CHAPTER II

RABENOSYN-5 DEFINES THE FATE OF THE TRANSFERRIN RECEPTOR FOLLOWING CLATHRIN-MEDIATED ENDOCYTOSIS

ABSTRACT

Cell surface receptors and other proteins internalize through diverse mechanisms at the plasma membrane, and are sorted to different destinations. Different subpopulations of early endosomes have been described, raising the question of whether different internalization mechanisms deliver cargo into different subsets of early endosomes. To address this fundamental question we developed a microscopy platform to detect the precise position of endosomes relative to the plasma membrane during the uptake of ligands. Axial resolution is maximized by concurrently applied total internal reflection fluorescence (TIRF) and epifluorescence structured light. We found that transferrin receptors are selectively delivered from clathrin-coated pits on the plasma membrane into a specific subpopulation of endosomes enriched in the multivalent Rab and phosphoinositide binding protein Rabenosyn-5. Depletion of Rabenosyn-5, but not of other early endosomal proteins such as EEA1, resulted in impaired transferrin uptake and lysosomal degradation of transferrin receptors. These studies reveal a critical role for Rabenosyn-5 in determining the fate of transferrin receptors internalized by clathrin-mediated endocytosis, and more broadly, a

mechanism whereby the delivery of cargo from the plasma membrane into specific early endosome sub-populations is required for its appropriate intracellular traffic.

INTRODUCTION

The endocytic pathway is known principally for its role in the uptake of receptors and ligands [47,95-97] and increasingly is being recognized as critical in other aspects of cell physiology. For example, the control of cellular growth through mammalian target of rapamycin signaling involves associations with late endosomal membranes [98,99], and microRNA regulatory mechanisms are associated with endosomal/lysosomal membranes [100-102]. Thus, it is necessary to understand how the distinct membrane compartments of the endocytic pathway form, traffic internalized ligands, and serve as scaffolds for the assembly of regulatory complexes.

In the classical view of the endocytic pathway [44-48], internalizing cargoes are incorporated into vesicles formed by clathrin-mediated or other mechanisms of endocytosis at the plasma membrane. These vesicles fuse with a homogenous population of early endosomes from which cargo then is sorted to different destinations. However, recent results demonstrate that genetic networks involved in the early trafficking of the transferrin (Tf) and EGF receptors (TfR and EGFR, respectively) differ from each other substantially [103] and find that EGF and Tf populate different subsets of vesicles almost immediately after

addition to live cells at physiological temperature [49]. Further evidence for early endosome heterogeneity is found in studies in which endosomes display different motilities and different phosphoinositide effector complements [65,66,104]. These results suggest that different populations of early endosomes exist, raising the possibility that different ligands may be directed specifically from the plasma membrane into particular early endosome classes rather than internalizing into a common early endosome.

The TfR has been studied extensively to define mechanisms involved in receptor-mediated endocytosis [47,105]. This receptor concentrates in clathrin-coated membrane regions [106], from which it enters the endosomal system. Iron bound to Tf is released at the low pH of the endosomes, and the TfR recycles to the plasma membrane and releases iron-free Tf. To visualize directly the movement of TfRs from clathrin-coated membrane structures into specific early endosome subpopulations, we developed a microscopy platform capable of simultaneously detecting three different fluorophores using total internal reflection fluorescence (TIRF). Because TIRF images confound intrinsic fluorescence brightness with axial position, the true position of an endosome relative to the plasma membrane can be obtained only if its actual brightness is known. Thus, we concurrently determined the in focus brightness of the endosomes in the TIRF field using Epifluorescence structured light (ESL) [107,108]. The combination of TIRF and ESL microscopy (TESM) provides the precise localization of endosomes relative to the cell surface.

Among key endosomal components implicated in early endosome fusion are proteins such as early endosome antigen 1 (EEA1) [109,110], adaptor protein phosphotyrosine interaction (APPL1) [67], and Rabenosyn-5 [32]. Their function is controlled by small GTPases, such as Rab4 and Rab5, and lipids such as phosphatidylinositol 3-phosphate [31,38,111]. To determine the role of endosomes containing these proteins, we imaged each one simultaneously with clathrin and Tf. We found distinct endosome subpopulations enriched in these markers residing at different regions within the TIRF zone. Tf is internalized from clathrin-coated regions at the plasma membrane into endosomes containing Rabenosyn-5. Depletion of Rabenosyn-5, but not of EEA1, results in TfR missorting and extensive degradation, coupled with alterations in clathrin dynamics. These results reveal the importance of Rabenosyn-5 in early endosomal trafficking of cargo internalized through clathrin-mediated mechanisms and suggest that specific endosome populations are involved in the trafficking of cargo entering through distinct plasma membrane internalization pathways.

RESULTS

Flux of Tf from the Plasma Membrane through the Endosomal System

To visualize the movement of Tf from clathrin-enriched plasma membrane regions into the endosomal system, Tf-DyLight-649 was added to cells cotransfected with TagRFP-T-clathrin and EGFP-tagged Rabenosyn-5, APPL1,

or EEA1. Cells were imaged at 1 Hz (one frame/s) continuously for 15 min: 5 min before the addition, 5 min in the presence, and 5 min after the removal of Tf-DyLight-649. Figure 2.1A illustrates one time frame of the resulting 900-image set, taken 1 min after the addition of Tf. To analyze these complex time-lapse image sets systematically, we used the method illustrated in Figure 2.1B and further described in Experimental Procedures. This method identifies all individual structures within the image and measures the relative amount of Tf specifically associated with them at each time point. In this example, images of TagRFP-T-clathrin (Figure 2.1B, Top, Unprocessed) are first convolved using a difference of Gaussians (DOG) filter to eliminate the diffuse signal originating from out of focus or auto fluorescence (Figure 2.1B, Top, DOG). The pixel of highest intensity within each region is identified (Figure 2.1B, Top, MIP) and is mapped on the unprocessed clathrin image (Figure 2.1B, Middle Left). A 5 × 5 pixel square (25 pixels) surrounding this pixel is outlined (Figure 2.1B, Middle Right), and its mean intensity [clathrin (in)] is recorded. From this value, the mean intensity of a one-pixel-wide frame (24 pixels) surrounding the square (Figure 2.1B, Middle Right, hatched regions) is subtracted [clathrin (out)], thus subtracting the local background. The positions of the maximum intensity pixels (MIPs) derived from the clathrin image are mapped onto the corresponding unprocessed Tf image (Figure 2.1B, Bottom), and the same calculation is performed. Thus, Tf has a positive value only if the signal detected within the 5 × 5 pixel region is higher than that of the immediate surrounding region. The ratio

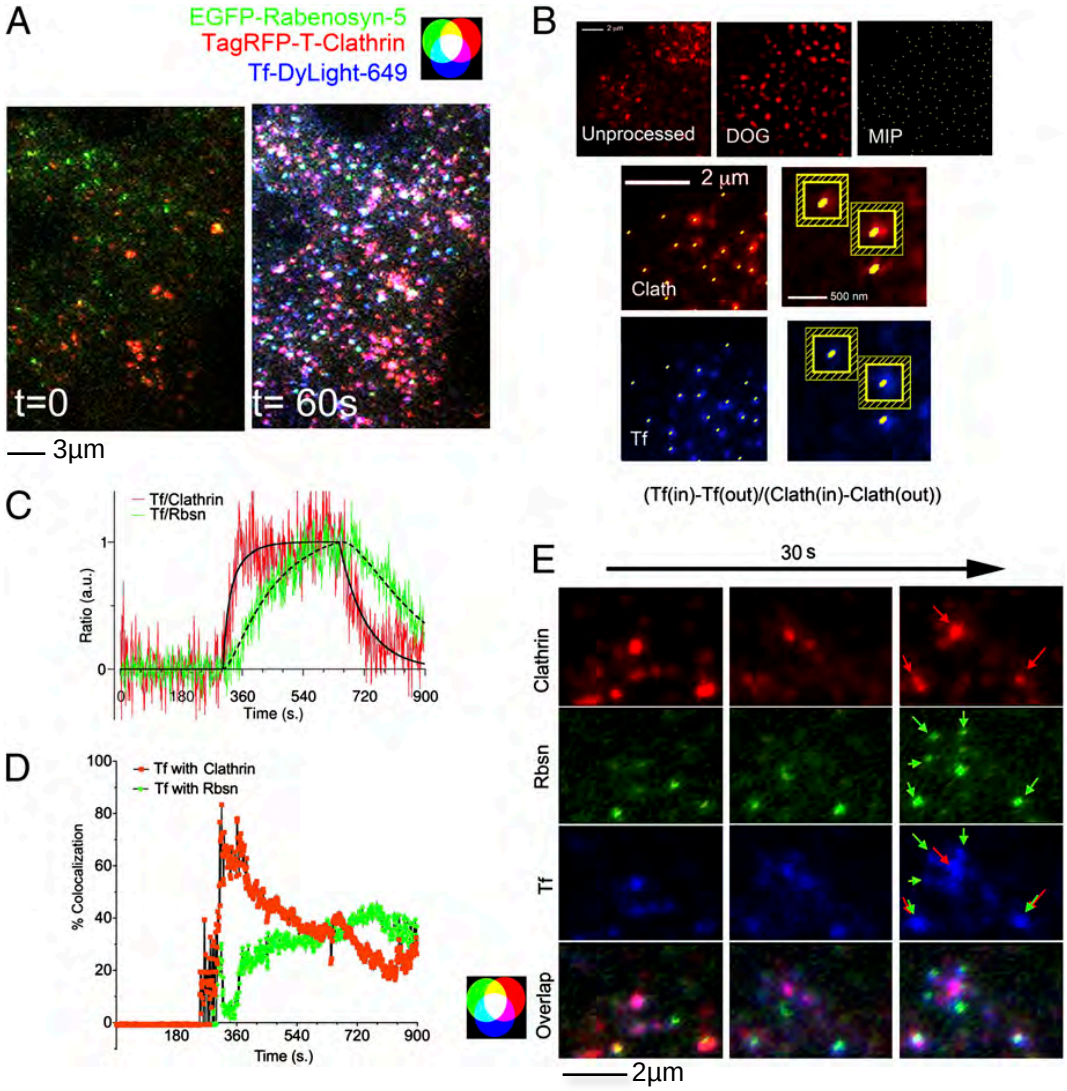
A
EGFP-Rabenosyn-5
TagRFP-T-Clathrin
Tf-DyLight-649
t=0
t= 60s
3µm
B
Unprocessed
DOG
MIP
2 µm
Clath
500 nm
Tf
(Tf(in)-Tf(out)/(Clath(in)-Clath(out))
C
Tf/Clathrin
Tf/Rbsn
Ratio (a.u.)
Time (s.)
D
Tf with Clathrin
Tf with Rbsn
% Colocalization
Time (s.)
E
30 s
Clathrin
Rbsn
Tf
Overlap
2µm

Figure 2.1. Dynamics of Tf flux into Rabenosyn-5 enriched endosomes. A. Cells co-expressing EGFP-Rabenosyn-5 (green) and TagRFP-T-Clathrin (red) were exposed to Tf-DyLight-649 (blue). Representative frames of images taken immediately before (t=0) and 60 seconds after addition of Tf (t=60s). **B**. A representative unprocessed image (top, left) of TagRFP-T-Clathrin was smoothed using a difference of Gaussians as described in the Methods (DOG, top, center), and the maximum intensity pixel (MIP) of each region identified (MIP, top, right) and mapped onto the unprocessed Clathrin (Clath, center, left) and Transferrin (Tf, bottom left) images. Areas of 5x5 pixels (in) and a surrounding 1 pixel-wide frame (out) were delineated around each MIP in each image (center and bottom right). **C**. The average ratio of (Tf(in) - Tf (out))/ (Clath(in) - Clath(out)) and (Tf(in) - Tf (out))/(Rbsn(in) - Rbsn(out)) of all maximum intensity pixels at each time point was calculated and normalized to a maximum of 1. **D**. Percent of Tf pixels colocalized with Clathrin (red) or Rabenosyn-5 (green) over time. Spikes seen upon addition and removal of Tf are due to temporary focus shifts, which recover rapidly. This experiment was repeated 4 times with similar results (Table. 2.1). **E**. Representative images showing Tf associating with clathrin-enriched regions (red arrows) and subsequently with Rabenosyn-5 endosomes (green arrows).

of the values obtained [Tf (in) − Tf (out)/clathrin (in) − clathrin (out)] for each region then is calculated, and the mean of all regions in the image is plotted for each time point (Figure 2.1C). In the same cell, the trafficking of Tf into Rabenosyn-5–containing endosomes is measured similarly. The data (Figure 2.1C) are fit into a kinetic model, described in detail in the experimental procedures "Curve Fits to Ratio Data" section, that incorporates known constants for Tf binding to the TfR, the concentration of free ligand, and the amount of Tf associated with clathrin.

Tf associates rapidly and saturably with clathrin-containing regions, displaying kinetic constants consistent with binding to the TfR (Table 2.1) [112-114]. Interestingly, Tf is detected almost immediately within Rabenosyn-5–enriched regions, with virtually no time elapsing between the detection of Tf in clathrin-coated regions and its detection in Rabenosyn-5 endosomes, and continues to accumulate in these endosomes as long as free Tf is present. When Tf is removed from the medium, it disappears rapidly from clathrin-enriched regions because of transfer into the endosomal pathway (Table 2.1). Strikingly, the rate of exit of Tf from clathrin-containing membrane regions (0.0053 ± 0.002/s, mean ± SEM, n = 4), is indistinguishable from its rate of entry into Rabenosyn-5–enriched endosomes (0.0037 ± 0.002/s, mean ± SEM, n = 4) (Table 2.1), implying that Tf internalized via clathrin-coated pits could be delivered almost directly into Rabenosyn-5–containing endosomes.

We then calculated the net amount of Tf colocalizing with clathrin and

Table 2 1. Kinetic constants for transferrin trafficking through Clathrin and Rabenosyn-5

	Tf/clathrin				
experiment	**t1**	**t2**	**A1**	**Tfconc**	**k(empty)**
1	303	647	0.19534	7.18E-08	0.01062
2	297	622	0.11696	4.44E-08	0.00534
3	316	664	0.56492	1.51E-08	0.00123
4	296	624	0.22226	2.67E-08	0.00407
mean	303.6	637.2	0.24078	6.32E-08	0.00538
std.err.	3.6	8	0.08408	2.55E-08	0.00152
tau(sec.)					185.9

	Tf/rabenosyn			
experiment	**B1**	**k(in)**	**k(empty)**	**k(fill)**
1	2.5159	0.00593	0.00681	0.00037639
2	0.4234	0.10487	0.03356	0.00136871
3	2.9916	0.01162	0.0055	0.00897243
4	5.5213	0.01227	0.00589	0.00406776
mean	2.86305	0.03367	0.01294	0.00369632
std.err.	1.04703	0.02377	0.00688	0.00192386
tau(sec.)			77.3	270.5

Rabenosyn-5 over time (Figure 2.1D). Approximately 70– 80% of Tf colocalized with clathrin within 2 min of exposure and then decreased because of increasing accumulation in endosomes. The amount of Tf colocalizing with Rabenosyn-5 increased in parallel, reaching ~40% of the signal, such that >80% of Tf can be accounted for as colocalizing with either clathrin or Rabenosyn-5 4–5 min after addition. Thus, both the kinetics (Figure 2.1C) and the net amount measured (Figure 2.1D) indicate that the majority of Tf proceeds from clathrin-coated pits/vesicles into Rabenosyn-5– containing endosomes. Visual inspection of the images reveals numerous events consistent with this model, where Tf is seen moving from clathrin-enriched regions of the plasma membrane into endosomes containing Rabenosyn-5 localized in the immediate vicinity (Figure 2.1E).

If indeed Tf can be delivered preferentially and rapidly to Rabenosyn-5-enriched endosomes, there may be a high degree of proximity between clathrin-coated plasma membrane regions and Rabenosyn-5-containing endosomes. TIRF imaging alone cannot be used to determine the positional relationship between these structures, because the brightness of an object can result from either its size or its distance from the cell surface (coverslip). Thus, to determine the topological relationship between clathrin-coated regions and endosomes, we concurrently obtained ESL images, which provide the actual intensity of fluorescent structures within the field. TIRF (Figure 2.2A, TIRF) and ESL (Figure 2.2A, ESL) images of GFP-clathrin and endogenous Rabenosyn-5 were obtained and were used to derive high-resolution 3D maps (TESM) of the position of

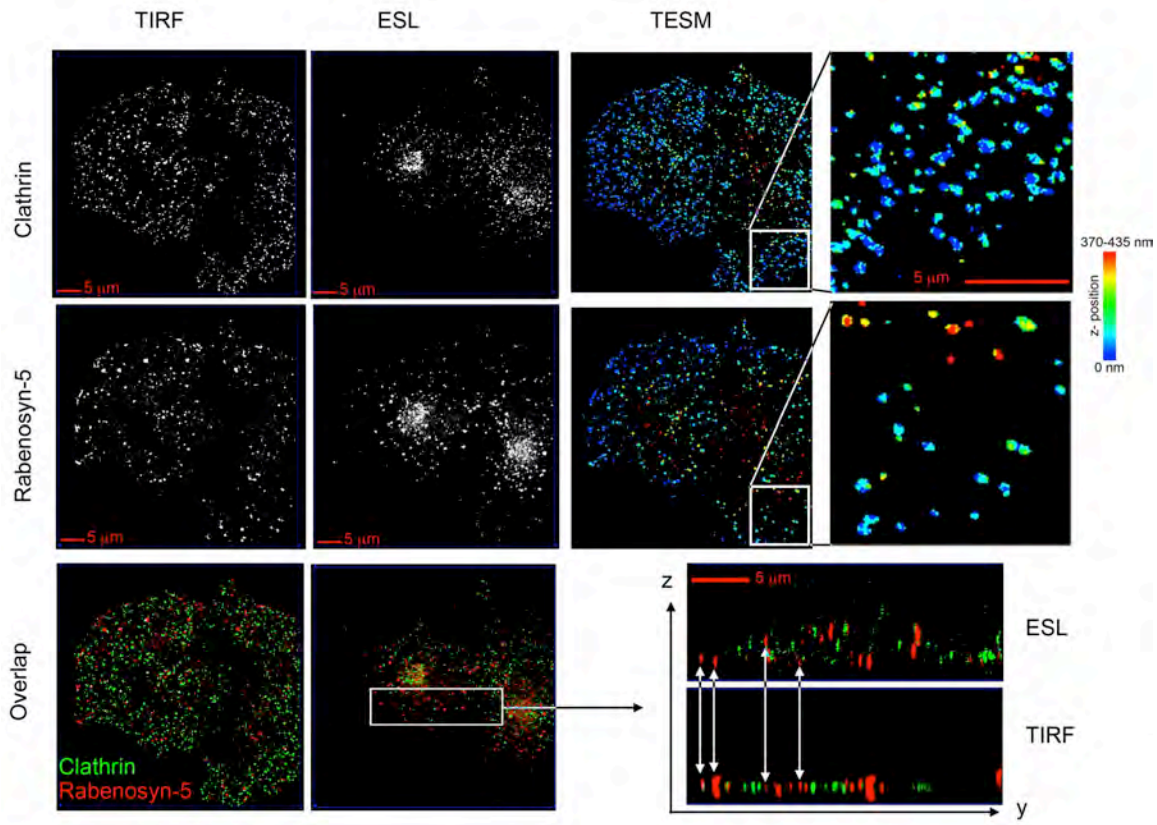

Figure 2.2. Localization of Rabenosyn-5 enriched endosomes and Clathrin relative to the cell surface. COS-7 cell expressing EGFP-Clathrin and stained with antibodies to endogenous Rabenosyn-5 imaged with TIRF and epifluorescence structured light (ESL), and the resulting z-maps derived by TESM. Rightmost panels are enlargements of the section indicated. Lower panels are the overlapped images of Clathrin (green) and Rabenosyn-5 (red), displayed in XY orientation, and YZ orientation of the section indicated. Arrows indicate the differing depths within the cell at which Rabenosyn-5 containing endosomes detected in the TIRF zone are found.

endosomes relative to the cell surface, as described in detail in Experimental Procedures. In these images, objects closest to the plasma membrane are displayed as blue, and those furthest away from the plasma membrane are displayed in red. Numerous endosomes containing Rabenosyn-5 are as proximal as clathrin-enriched regions to the cell surface. Similar information was obtained when clathrin and Rabenosyn were compared directly in overlapped TIRF and ESL images displayed in XZ orientation. Bright objects visible in ESL often are less visible in TIRF because of their distance from the cell surface, and objects highly visible in TIRF actually may be dimmer objects that are very close to the cell surface. These images demonstrate that Rabenosyn-5–enriched endosomes are in close proximity to clathrin-enriched regions at the cell surface, indicating that the topological organization of this pathway could accommodate a transfer from clathrin-coated pits/vesicles into these endosomes.

To determine whether the delivery of Tf into Rabenosyn-5-containing endosomes is specific, we analyzed the relationship between Tf internalization and other endosome classes. Recently it has been shown that in cells expressing the constitutively active V12G mutant of H-Ras, clathrin-mediated endocytosis gives rise to a set of endosomal intermediates containing the protein APPL1 [104]. As others have reported previously [67,104], we found APPL1 on small vesicles at the periphery of the cell image, whereas clathrin-enriched regions are present throughout (Figure 2.3A, Upper). Several of the APPL1-containing structures localize close to clathrin (Figure 2.3A, Lower), consistent

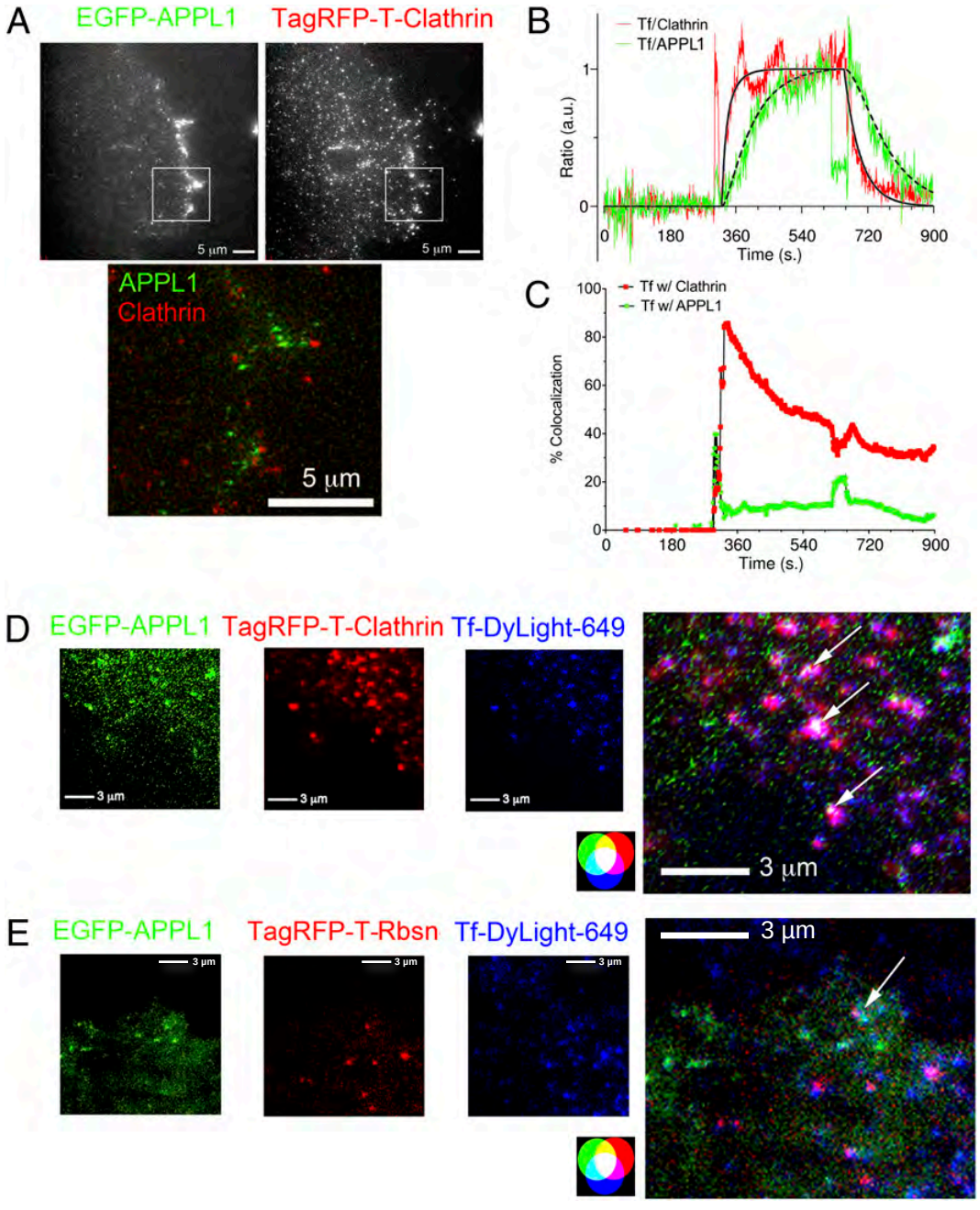
A
EGFP-APPL1
TagRFP-T-Clathrin
5 μm
5 μm
APPL1
Clathrin
5 μm
B
Tf/Clathrin
Tf/APPL1
Ratio (a.u.)
1
0
0
180
360
540
720
900
Time (s.)
C
Tf w/ Clathrin
Tf w/ APPL1
% Colocalization
100
80
60
40
20
0
0
180
360
540
720
900
Time (s.)
D
EGFP-APPL1
TagRFP-T-Clathrin
Tf-DyLight-649
3 μm
3 μm
3 μm
3 μm
E
EGFP-APPL1
TagRFP-T-Rbsn
Tf-DyLight-649
3 μm
3 μm
3 μm
3 μm

Figure 2.3. Tf flux into APPL1-enriched endosomes. **A**. Epifluorescence images of COS-7 cells co-expressing EGFP-APPL1 (green) and TagRFP-T-Clathrin (red). Region of the cell showing APPL1 localizing to small vesicles at the cell periphery in proximity to clathrin. **B**. Quantification of the ratio of (Tf(in) - Tf (out))/(Clath(in) - Clath(out)) and (Tf(in) - Tf (out))/(APPL(in) - APPL(out)) plotted as the mean of all regions at each time point over time. Spikes seen upon addition and removal of Tf are due to temporary focus shifts, which recover rapidly. **C**. Quantification of Tf colocalization with clathrin (red) or APPL1 (green) over time, n=3. **D**. Representative image at 5 minutes following addition of Tf. Arrows in the overlapped image indicate the areas where clathrin, APPL1, and Tf colocalize. **E**. Representative image of EGFP- APPL1 and TagRFP-T-Rabenosyn-5 co-expressing COS-7 cell 5 minutes following addition of Tf. Arrow in overlapped image indicates the area where APPL1, Rbsn, and Tf colocalize.

Table 2.2. Kinetic constants for transferrin trafficking through Clathrin and APPL1

	Tf/clathrin				
experiment	**t1**	**t2**	**A1**	**Tfconc**	**k(empty)**
1	316.733	623.785	0.33306	2.89E-08	0.0039488
2	322.342	656.389	0.17782	1.06E-07	0.0207115
3	313.38	621.008	0.12156	2.83E-07	0.0097476
4	298.298	629.488	0.41734	5.46E-09	0.0043682
mean	312.688	632.667	0.26244	1.06E-07	0.009694
std.err.	5.14	8.101	0.0683	6.28E-08	0.0039025
tau(sec.)					103.2

	Tf/APPL1			
experiment	**B1**	**k(in)**	**k(empty)**	**k(fill)**
1	2.37253	0.0140693	0.0078423	0.00375113

with the hypothesis [104] that APPL1-containing endosomes are derived from clathrin-coated vesicles. Tf occupied APPL1-containing structures at a rate similar to the rate at which it entered Rabenosyn-5 endosomes (Figure 2.3B and Table 2.2), but the net amount of Tf localizing to APPL1-enriched endosomes was almost negligible (Figure 2.3C). In addition, only APPL1 endosomes closest to clathrin colocalized with Tf (Fig. 3D, overlap, white pixels), and these endosomes also contained Rabenosyn-5, as visualized in cells coexpressing EGFP-APPL1 and TagRFP-T-Rabenosyn-5 (Figure 2.3E). Thus, Tf does not internalize through endosomes containing only APPL1.

Functional Role of Rabenosyn-5 in TfR Internalization

To examine the function of Rabenosyn-5 in Tf trafficking, we analyzed the effects of siRNA-mediated depletion. Rabenosyn-5 protein decreased 48 h after transfection and was undetectable after 72 h (Figure 2.4A, Top). Surprisingly, TfR levels were decreased markedly in response to Rabenosyn-5 knockdown, with the decline beginning 48 h after transfection (Figure 2.4A, Middle). This effect was specific to the TfR, because GAPDH (Figure 2.4 A and B), or other elements of the endocytic pathway, such as clathrin, EEA1, and APPL1, and other receptors, such as the EGFR, were not affected (Figure 2.4B). To determine whether other components of the early endocytic pathway would lead to similar changes in TfR levels, we compared the effects of Rabenosyn-5 and EEA1 depletion. Depletion of EEA1 did not result in TfR degradation; instead, a

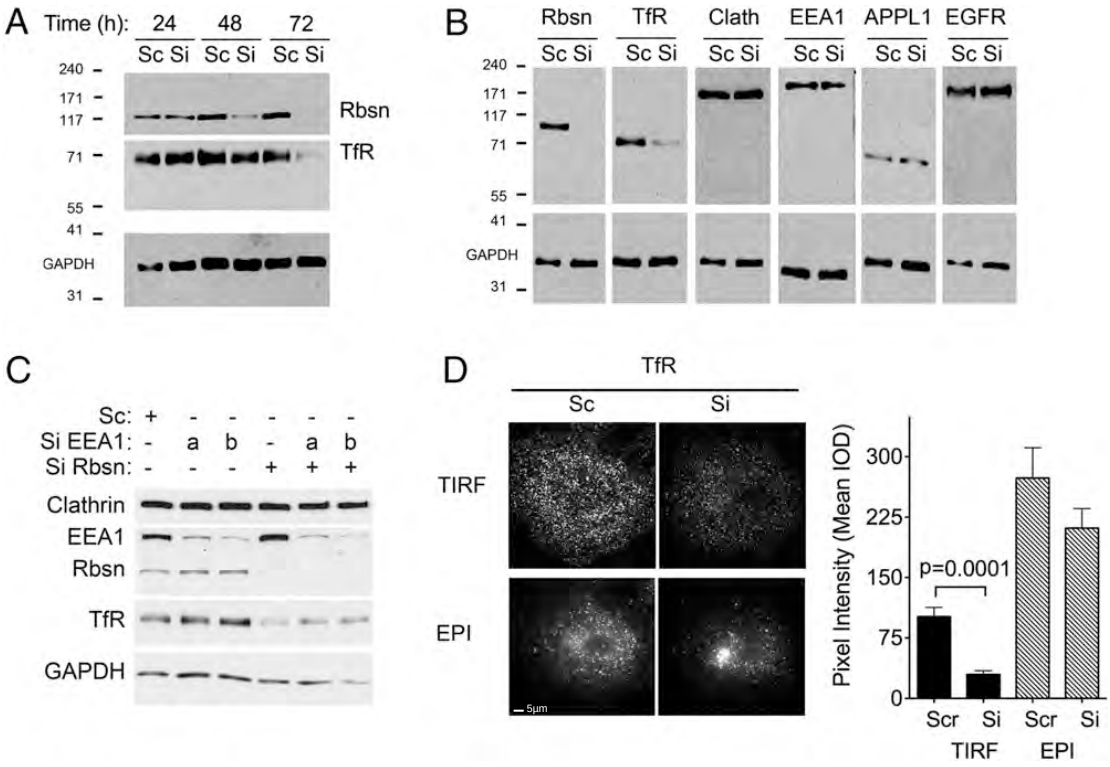

Figure 2.4. Time course and effect of Rabenosyn-5 depletion on levels of endocytic proteins. A. Cells were transfected with scrambled (Sc) or Rabenosyn-5-directed (Si) oligonucleotides, and at the time points indicated or at 72 h and (**B**) analyzed by western blotting for the proteins indicated (Rabenosyn-5 = Rbsn; Transferrin receptor = TfR; Clathrin heavy chain = Clath; EGF Receptor = EGFR). **C**. Cells were transfected with scrambled (Sc), two different EEA1-directed (SiEEA1 a,b) oligonucleotides, or Rabenosyn-5-directed (Si Rbsn) and at 72 h analyzed by Western blotting for the proteins indicated. **D**. Representative TIRF (top panels) and epifluorescence (EPI, bottom panels) images of endogenous TfR in cells transfected with scrambled (Sc) or Rabenosyn-5- directed (Si) oligonucleotides for 72 hours. Epifluorescence images are auto scaled for illustration purposes to reveal the region of maximal TfR concentration. d. Quantification of the mean intensity of endogenous TfR in TIRF and EPI images.

small but detectable increase in TfR levels was observed (Figure 2.4C). These results demonstrate that Rabenosyn-5 and EEA1 have fundamentally different roles in Tf trafficking and are consistent with a previously proposed role of EEA1 in trafficking toward the lysosomal pathway [49]. To determine whether Rabenosyn-5 depletion would, in addition to decreasing total levels, affect the cellular distribution of the TfR, we performed immunofluorescence analysis. A marked decrease in endogenous TfR levels was visible in the TIRF zone (Figure 2.4D, Upper Left), with remaining receptors detected by epifluorescence in the juxtanuclear region (Figure 2.4D, Lower Left). Quantification of the image intensity revealed a 75% decrease in TfR intensity in TIRF. These results reveal that the absence of Rabenosyn-5 results in a depletion of the TfR population found in the cell periphery at steady state.

To examine further how Rabenosyn-5 depletion affects TfR trafficking, we examined its internalization and recycling rates. Tf internalization was reduced markedly in cells depleted of endogenous Rabenosyn-5, and this defect could be rescued by transfection of exogenous EGFP-tagged Rabenosyn-5 (Figure 2.5). The binding of Tf to the cell surface (Figure 2.6A) and the net amount internalized (Figure 2.6B) were decreased significantly in cells depleted of Rabenosyn-5, consistent with the decrease in total and surface TfR levels detected by Western blotting and TIRF imaging. However, the rate of individual receptor internalization, assessed from the ratio of bound to internalized Tf (Figure 2.6C), was not significantly different, suggesting that the lack of

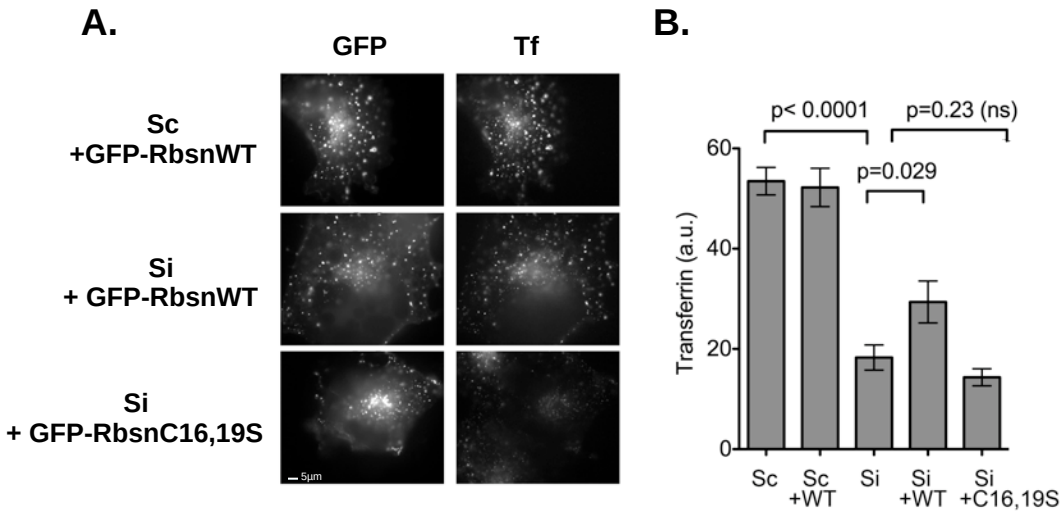

Figure 2.5. Inhibition of Tf uptake by Rabenosyn-5 knockdown is rescued by wild-type EGFP-Rabenosyn-5 expression. Cells were exposed to scrambled (Sc) or Rabenosyn-5 directed siRNA oligonucleotides (Si) for 72 hr, without or with co-transfection of non-siRNA resistant wild-type EGFP-tagged Rabenosyn-5 (RbsnWT) or a mutant in which the C2H2 N terminal zinc finger was disrupted by mutation of Cysteine residues 16 and 19 to serine (RbsnC16,19S). Transferrin was added for 10 min, and cells fixed and imaged. **A.** Representative cells. **B.** Quantification of average Tf fluorescence intensity in 10 fields of cells acquired with a 20x objective. Statistical analysis was done using two tailed student t- tests

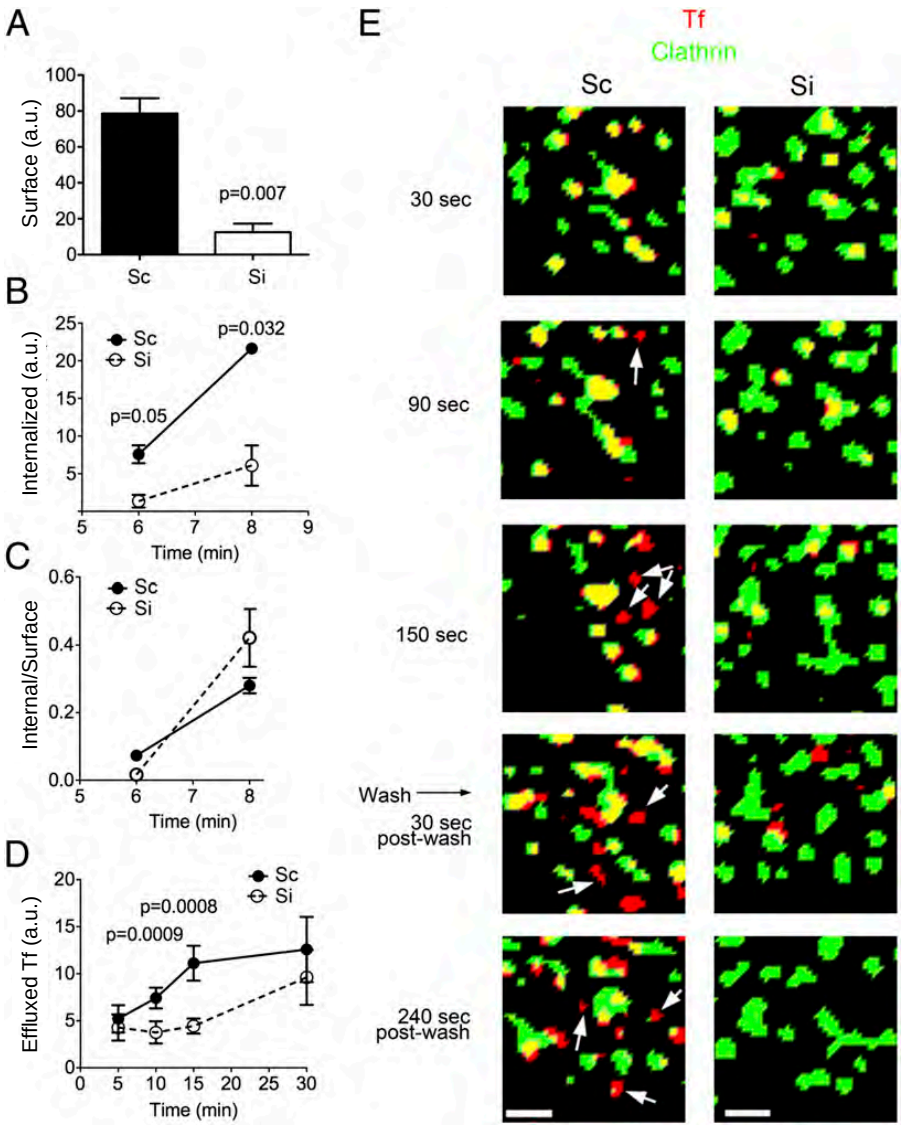

Figure 2.6. Effect of Rabenosyn-5 depletion on Tf trafficking. Cells were transfected with scrambled (Sc) or Rabenosyn-5-directed (Si) oligonucleotides, and at 72 h the cell surface binding (**A**), internalization (**B**) internalization rate (**C**) and recycling rate (**D**) were measured using HRP-labeled Tf and chemiluminescence as described in the Experimental Procedures. Plotted are the means and SEM of three experiments. Statistical significance was calculated using two-tailed Student t-test for each time point as indicated. **E**. Cells were transfected with EGFP-clathrin and treated with scrambled (Sc) or Rabenosyn-5 siRNA (Si) for 72 hr. Tf-DyLight-649 was added and removed 300s later, and shown are images obtained at the time points indicated. Images were smoothed as described in Figure 2.1, and binary renditions generated to visualize all signal present. Pixel overlap is rendered in yellow. Arrows point to structures containing transferrin but devoid of clathrin.

Rabenosyn-5 does not directly impair the very early steps of TfR recruitment into clathrin-coated vesicles. In contrast, the recycling of TfR to the plasma membrane, assessed by the release of previously internalized Tf (Figure 2.6D), was markedly decreased by Rabenosyn-5 depletion. The major difference in recycling rate was seen in the first 15 min, suggesting that the rapid recycling pathway of the TfR [47] is affected preferentially. To compare the biochemical results to events at the single-cell level, Tf uptake and recycling were visualized by TIRF in cells expressing GFP-clathrin (Figure 2.6E). In both control and Rabenosyn-5–depleted cells, Tf associates immediately with clathrin-enriched regions of the membrane, such that at early time points (0–30 s) virtually all the Tf signal colocalizes with clathrin (Figure 2.6E, Top, yellow). Subsequently, vesicular structures appear that contain Tf but lack clathrin (Figure 2.6E, arrows, red). At 30 s after washing these structures are likely to represent both uncoated internalizing vesicles and vesicles involved in rapid recycling of Tf; the latter gradually predominate with increasing time following removal of Tf from the medium (Figure 2.6E, t = 240 s after washing). Recycling vesicles were greatly reduced in cells depleted of Rabenosyn-5, consistent with the finding of a slowed rapid recycling rate seen in the cell population (Figure 2.6D).

To begin to define the mechanisms by which Rabenosyn-5 depletion leads to a decrease in TfR levels, we first examined whether its effects were exerted at the transcriptional or post-transcriptional level. Translation of the TfR is regulated through sequences in the 3′ and 5′ untranslated regions (UTRs) of its

mRNA. To study the regulation of TfR levels independently of translational control, we measured the levels of TfR-EGFP expressed from a plasmid lacking the regulatory sequences present in the endogenous TfR mRNA (Figure 2.7A). Endogenous and GFP-tagged expressed TfR levels were reduced equally in response to Rabenosyn-5 depletion, ruling out an effect of this protein on transcriptional or translational control of TfR expression. Although the majority of the TfR undergoes recycling after internalization, a larger proportion may be targeted to the lysosome for degradation in the absence of Rabenosyn-5 [115]. Consistent with this possibility, exposure of cells to Bafilomycin A1, an inhibitor of acidification and lysosomal degradation, resulted in increased TfR levels (Figure 2.7B), and this effect was more pronounced in Rabenosyn-5–depleted cells. Together these results suggest a model in which, in the absence of Rabenosyn-5, the TfR is missorted into endosomes that direct cargo toward lysosomal degradation (Figure 2.7C).

In addition to decreased TfR levels and Tf recycling, Rabenosyn-5-depleted cells also displayed alterations in clathrin dynamics. Both the number of GFP-clathrin regions detected by TIRF (Figure 2.8A) and their average size (Figure 2.8B) were significantly greater in cells depleted of Rabenosyn-5. Analysis of endogenous clathrin was consistent with the results seen for GFP-clathrin, revealing an increase in the intensity of clathrin signal in the TIRF zone and the perinuclear region (Figure 2.8 C and D). Because no difference in total clathrin was detected by Western blotting (Figure 2.4B), and there is a significant

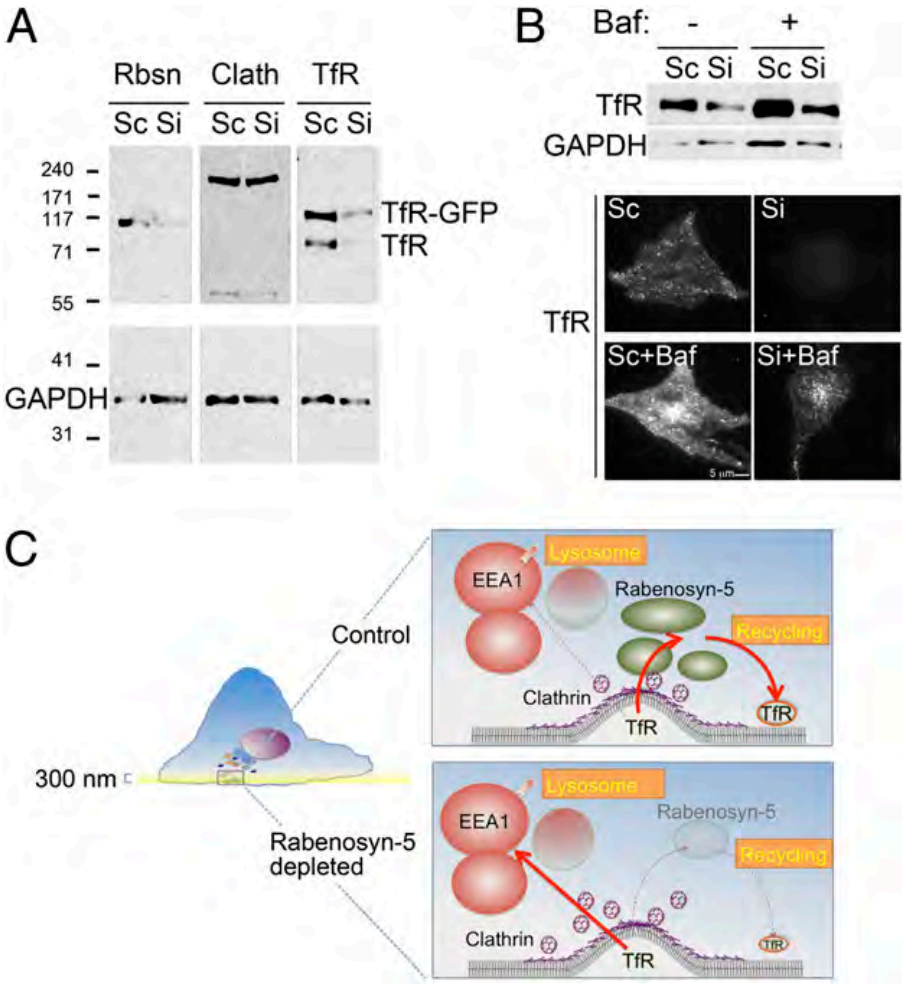

Figure 2.7. Mechanism of TfR loss in response to Rabenosyn-5 depletion. A. Western blotting of TfR in cells transfected with TfR-GFP and treated with scrambled (Sc) or Rabenosyn-5 siRNA (Si) for 72 hr after transfection. GAPDH is used as a loading control. **B**. Cells were transfected with scrambled (Sc) or Rabenosyn-5-directed (Si) oligonucleotides, and at 48 hr treated with or without 100nM Bafilomycin A1 (Baf). After 24 hr lysates were harvested and analyzed by Western blotting and immunofluorescence for the TfR. **C**. In this model, TfR is internalized into endosomes marked by Rabenosyn-5, which are juxtaposed to clathrin-coated plasma membrane regions, from which it is rapidly recycled to the plasma membrane. A small fraction of TfR may be directed into EEA1-enriched endosomes, which are destined for lysosomal degradation. In the absence of Rabenosyn-5, clathrin-coated structures accumulate and their cargo enters lysosome- directed pathways, resulting in low recycling rates.

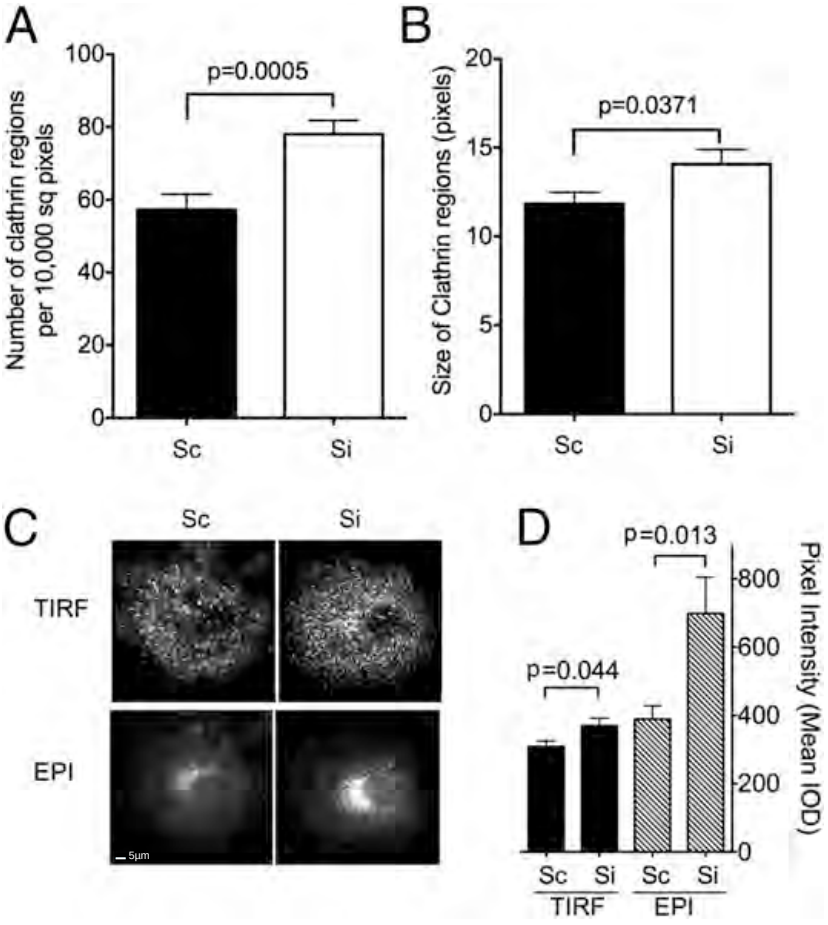

Figure 2.8. Effect of Rabenosyn-5 depletion on Clathrin Distribution. Cells were transfected with EGFP-clathrin and treated with scrambled (Sc) or Rabenosyn-5 siRNA (Si) for 72 hr. The number (**A**) and size (**B**) of clathrin regions in the TIRF zone was determined from binary renditions of smoothed images such as those depicted in Figure 2.6E. Results are the means and SEM of regions from 8-10 cells. **C**. Representative TIRF (top panels) and epifluorescence (bottom panels) images of endogenous clathrin in cells transfected with scrambled (Sc) or Rabenosyn-5- directed (Si) oligonucleotides for 72 hours. **D**. Quantification of the mean intensity of endogenous clathrin in TIRF and epifluorescence (EPI) images. Results are the means and SEM of 8-10 cells. Statistical significance was calculated using two-tailed Student t-test.

pool of cytoplasmic unassembled clathrin in these cells (not illustrated), these results suggest that Rabenosyn-5 depletion leads to an increase in the proportion of total cellular clathrin assembled on both the plasma membrane and the trans-Golgi network. Although more work is required to understand their mechanistic basis, these findings further suggest a possible direct interaction between clathrin, or associated molecules, and Rabenosyn-5 on endosomes, possibly facilitating the delivery of cargo to the specific endosome subpopulation containing this protein.

We and others have previously found that the EGF receptor, which is largely degraded after internalization, quantitatively enters EEA1-enriched endosomes [49,116], suggesting that these endosomes are part of an endocytic route directing ligands to the lysosome for degradation. As suggested by knockdown of EEA1 (Figure 2.4C) and treatment with Bafilomycin A1 (Figure 2.7B) a significant amount of TfR appears to be targeted for degradation, therefore we asked the question of whether a fragment of internalized Tf might be directed into endosomes containing EEA1. Analysis of Tf uptake was performed in cells co-expressing EGFP-Rabenosyn-5 and TagRFP-T-EEA1. The rate with which Tf enters EEA1-enriched endosomes is slower than that at which it enters Rabenosyn-5 containing endosomes (Figure 2.9C), and the amount of Tf associated with EEA1-enriched endosomes was significantly smaller than that associated with Rabenosyn-5 enriched endosomes at any time point analyzed (Figure 2.9B). Images obtained from these cells were consistent

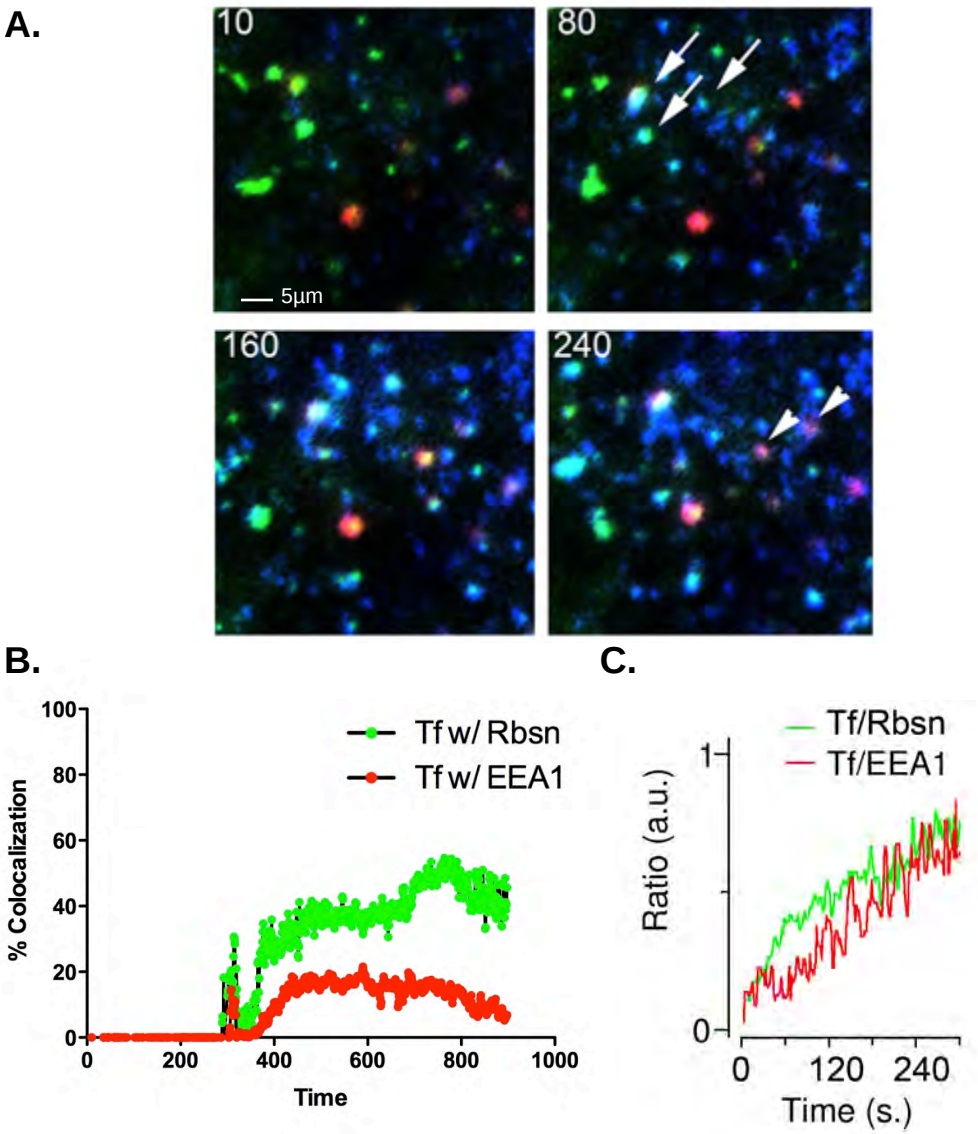

Figure 2.9. Relative flux of Tf through EEA1-enriched and Rabenosyn-5-enriched endosomes. A. Representative images of Tf-DyLight-649 uptake into cells co-expressing EGFP-Rabenosyn-5 (green) and TagRFP-T-EEA1 (red). Arrows depict Rabenosyn-5 endosomes co-localizing with Tf, arrowheads depict EEA1 endosomes co-localizing with Tf at times following addition of Tf indicated in seconds. **B.** Quantification of the percent of Tf co-localized with endosomes containing Rabenosyn-5 (green) and EEA1 (red). **C.** Quantification of the ratio of [Tf(in)-Tf(out)]/[Rbsn(in)-Rbsn(out)] and [Tf(in)-Tf(out)]/[EEA1(in)-EEA1(out)] plotted as the mean of all regions at each time point over time from cells co-expressing EGFP-Rabenosyn-5 and TagRFP-T-EEA1.

with the quantitative analysis; as seen before, Tf accumulated in Rabenosyn-5 labeled endosomes rapidly (Figure 2.9A, arrows), while EEA1-containing endosomes remained unoccupied. At later time points, Tf was found to colocalize with EEA1-containing endosomes (Figure 2.9A, arrowheads). These results indicate that a small but significant amount of Tf traffics into EEA1 endosomes, possibly reflecting the fragment of the receptor population being targeted for lysosomal degradation at steady state.

Topological organization of endosomes containing EEA1 and Rabenosyn-5

Several lines of evidence presented here and published by others suggest that EEA1 and Rabenosyn-5 mediate different endocytic trafficking functions. For example, knockdown of Rabenosyn-5 [70], but not of EEA1 [49], affects Tf recycling, and knockdown of EEA1 impairs EGF degradation. Data presented in Figure 2.2 shoes that Rabenosyn-5 enriched endosomes are juxtaposed to clathrin enriched regions at the cell surface and the evidence presented in Figure 2.9 suggests the potential for a topological relationship whereby EEA1 enriched endosomes are more distal from Rabenosyn-5 enriched endosomes. While overexpressed Rabenosyn-5 and EEA1 co-localize extensively under conditions where Rab5 is simultaneously over expressed [32] to our knowledge an analysis of the distribution of endogenous EEA1 and Rabenosyn-5 in the absence of Rab overexpression has not been performed. To obtain the topological relationship between Rabenosyn-5 endosomes and EEA1 endosomes we simultaneously

obtained TIRF and ESL images. Figure 2.10 illustrates the distribution of EEA1-containing and Rabenosyn-5 containing endosomes in the TIRF zone (Figure 2.10, TIRF) and in the three dimensional volume of the cell using ESL (Figure 2.10, ESL). By combining the TIRF and ESL images (Figure 2.10, TESM), a three dimensional map of the position of these endosomes within ~400nm from the plasma membrane was generated. These images reveal a population of endosomes containing Rabenosyn-5 but no EEA1 localized close to the plasma membrane (Figure 2.10, blue objects) compared to endosomes containing EEA1. When EEA1 and Rabenosyn-5 are expressed as fusion proteins with either EGFP or TagRFP-T, the distinct identity of endosomes containing these markers is also apparent (Figure 2.11). Both TIRF and ESL projected images reveal the presence of endosomes containing EEA1, Rabensoyn-5, or both. TESM also reveals Rabenosyn-5 enriched endosomes localized closer to the plasma membrane, as seen for the endogenous protein. Thus, expression of the tagged version of these molecules mimics their endogenous distribution. These studies suggest the Rabenosyn-5 endosomes are part of an endocytic route directing cargo for recycling. These pathways also appear to be spatially separated with Rabenosyn-5 endosomes residing closer to the plasma membrane than EEA1 endosomes. The results shown here suggest that sorting of internalized cargo proceeds through the delivery of cargo from the plasma membrane into specialized endosomal populations characterized by their topological organization relative to the plasma membrane.

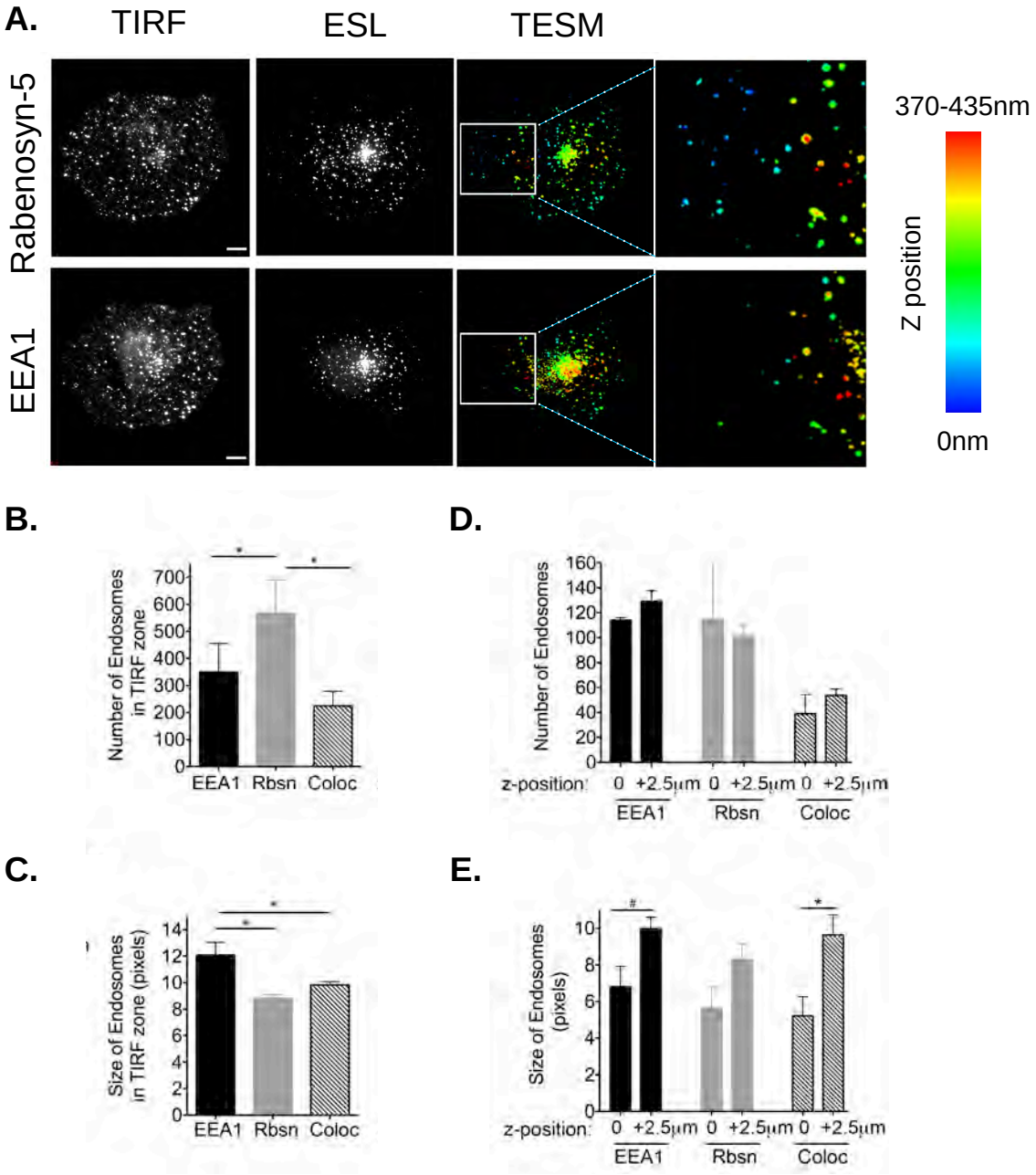

Figure 2.10. Topology of Rabenosyn-5 and EEA1-enriched endosomes. A. COS-7 cell stained with antibodies to endogenous Rabenosyn-5 and EEA1 imaged with TIRF, epifluorescence structured light (ESL), and TESM. *Right,* Enlarged image of section indicated. **B.** and **C.** The number and size, respectively, of endosomes containing EEA1, Rabenosyn-5 (Rbsn) or both (coloc) in the TIRF zone*p >0.05, n=5 cells. **D.** and **E.** The number and size, respectively, of endosomes containing EEA1, Rbsn or both (coloc) found by SLE at proximal (0) and distal (+2.5µm) points relative to the plasma membrane *p >0.05, n=5, two-tailed student t-test. #p>0.05, n=5, one-tailed student t-test.

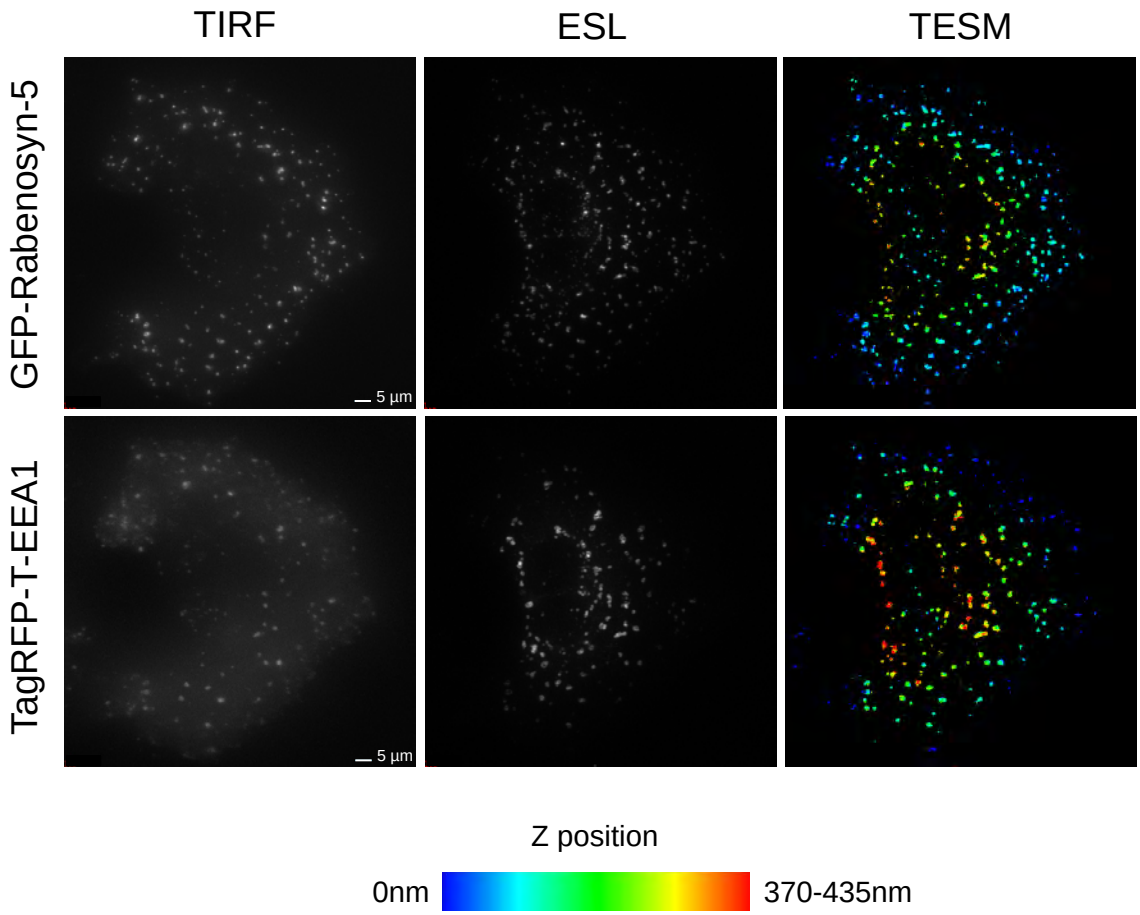

Figure 2.11. Topology of Expressed Rabenosyn-5 and EEA1-enriched endosomes. COS-7 cell co-expressing EGFP-Rabenosyn-5 and TagRFP-T-EEA1 analyzed by TIRF, ESL, and TESM.

DISCUSSION

A large amount of evidence has demonstrated that internalization from the plasma membrane proceeds through clathrin-dependent and -independent mechanisms [95] and that variation exists within these mechanisms, whereby, for example, certain subpopulations of clathrin-coated pits may capture different receptor types preferentially [114,117]. Until recently it was thought that these diverse internalization mechanisms delivered cargo into a homogenous population of early endosomes from which sorting to different destinations occurred. However, recent genetic and imaging results have suggested that early endosomes may not be functionally homogeneous, displaying differences in composition, cargo enrichment, and motility [49,65,66,103,104]. The findings of varied internalization mechanisms at the plasma membrane and of different endosome subpopulations raise the question of whether different internalization mechanisms are associated with distinct endosome subtypes.

To address this question, we investigated whether the TfR, internalized through clathrin-mediated endocytosis, would be delivered to a specific endosome subpopulation. This investigation required the use of a platform that could detect three fluorophores simultaneously with high temporal and spatial resolution in live cells and analytical methods to generate quantitative models from resulting complex images. By simultaneously monitoring clathrin and early endosome markers, it was possible to visualize Tf internalizing from clathrin-coated membrane structures into endosomes containing specific markers. The

resulting images and kinetic models derived from quantitative analysis indicated that Tf enters endosomes containing Rabenosyn-5 almost immediately following its entry through clathrin-coated structures. By enhancing axial resolution in the TIRF zone by combining TIRF and ESL, it was found that Rabenosyn-5–enriched endosomes reside closest to clathrin-enriched structures at the plasma membrane, providing a topological framework for delivery of Tf into this specific endosome population.

The results discussed above led us to test the hypothesis that Rabenosyn-5 might be functionally involved in the movement of TfR from clathrin-coated structures into endosomes. Biochemical and morphological analysis revealed impairment in rapid TfR recycling following internalization and a marked increase in TfR degradation. In conjunction, the dynamics of clathrin at the plasma membrane appear altered, with the size and number of clathrin-enriched regions being increased. Clathrin-enriched regions at the plasma membrane are larger than individual clathrin-coated pits and vesicles and are likely to represent areas of enhanced formation of these structures [106,112,114]. Thus, an increase in their size and number may reflect a delay in the movement of clathrin-coated vesicles away from the plasma membrane or a delay in their uncoating and fusion with endosomes (Figure 2.6C). These results are consistent with previous findings of impaired formation of early endosomes in *Drosophila* and *Caenorhabditis elegans* lacking Rabenosyn-5 [118,119] and with previous results in mammalian cells indicating a role for this protein in receptor recycling

[32,70,106]. Moreover, a direct role of Rabenosyn-5 in clathrin-mediated internalization may explain the mechanism by which dominant negative mutants of Rab5, which interacts with Rabenosyn-5 [120], impair Tf uptake [19].

Beyond identifying Rabenosyn-5 as an important regulator of TfR entry into the endosomal pathway, the data shown here suggest that sorting in general may occur through delivery of cargo into specific endosome subpopulations that maintain a defined topological organization relative to sites of endocytosis. Results by others also are consistent with the concept that diverse endocytic mechanisms are associated with specific endosomal subtypes. For example, work by Zoncu *et al*. [104] indicates that EGFR is internalized via macropinosomes that rapidly acquire APPL1 and subsequently acquire WD repeat and FYVE domain-containing protein 2 (WDFY2) and EEA1. We [49] and others [116] also have observed that EGF is internalized from the plasma membrane into EEA1-containing endosomes and have found relatively low colocalization of internalizing Tf with EEA1 [49,105,121]. Moreover, knockdown of EEA1 leads to a detectable increase in TfR levels (Figure 2.4) and to an impairment of EGFR degradation [49], in stark contrast to the effect of Rabenosyn-5 knockdown in decreasing TfR levels. These results support a model in which EEA1 and Rabenosyn-5 have fundamentally different roles in endosomal traffic: Endosomes containing EEA1 appear to capture cargo destined to lysosomes, whereas endosomes containing Rabenosyn-5 capture cargo destined for recycling (Figure 2.6C).

Despite these different functions, many endosomes containing both Rabenosyn-5 and EEA1 are found deeper within the cell [41], but how these endosomes arise is not clear. In one possible model, endosomes formed from larger portions of the membrane, such as EGF-containing macropinosomes that acquire EEA1 [104,122], also may acquire Rabenosyn-5 in conjunction with endosomal clathrin for the purpose of fully retrieving cargo that is not destined for the lysosomal pathway, as has been shown to occur for E-cadherin [123]. Alternatively, EEA1 may associate with Rabenosyn-5– enriched endosomes to retrieve cargo destined for degradation. This association is likely to vary with the levels of phosphatidylinositol 3-phosphate and Rab5 unoccupied by Rabenosyn-5. Thus, cargoes such as EGF, which increase the activity of PI3 kinases and activate Rab5 [124], would be expected to promote binding of EEA1 to Rabenosyn-5–containing endosomes. Activation of Rab5 also would be expected to result in enhanced EEA1 binding and more extensive colocalization of Rabenosyn-5 and EEA1 on the same endosomal surface, as indeed is observed in cells over-expressing wild-type or persistently active Rab5 [41].

In summary, the visualization of the initial steps of endocytosis using a multimodal imaging platform that improves axial resolution in TIRF and the use of analysis protocols that generate quantitative models from complex imaging data have identified Rabenosyn-5 as a key element in clathrin-mediated endocytosis and the initial node of Tf sorting. Further experiments with additional ligands and endosomal components will allow generation of quantitative, testable models for

the molecular mechanisms underlying receptor internalization into the endocytic pathway.

EXPERIMENTAL PROCEDURES

Cell culture and transfection – COS-7 cells were maintained in DMEM (Invitrogen) supplemented with 100U/ml penicillin streptomycin (Invitrogen), 0.1 mg/ml normocin (InvivoGen) and 10% fetal bovine serum (Atlanta Biologicals) at 37°C 5% CO_2. Cells were plated at a density of $1x10^5$ cells per well of a 6 well cell culture plate and grown for 24 hours. These cells were transfected with 1µg DNA using calcium phosphate and grown for 24 hours, plated on glass coverslips (Thomas Scientific 25 circle #1.5), grown for an additional 24 hours. Live imaging was done in KRH buffer (125M NaCl, 5mM KCl, 1.3mM $CaCl_2$, 1.2mM $MgSO_4$, 25mM HEPES, 2.5% BSA and 2mM sodium pyruvate) pH 7.4.

RNAi – Rabenosyn-5 and EEA1 RNAi duplexes with a sense sequence of 5'UUUGAUGUCACUGCCAACCAAAGAA 3' and 5' AGGACCAAAAGAUCCAGAACCUUGA 3', respectively, were designed and synthesized by RXi Pharmaceuticals. A second oligonucleotide to EEA1, with the sense sequence 5′-AACUUGCUACUGAAAUUGCAGUU-3′ (designated "a" in Figure 2.6D) was obtained from Dharmacon. One day before transfection cells were plated in antibiotic-free medium in a six-well cell-culture plate at a density of $1×10^5$ cells per well. Cells were transfected using 5µL of Lipofectamine

RNAiMAX (Invitrogen) according to the manufacturer's instructions with a final concentration of 10 nM siRNA.

Reagents – Polyclonal EEA1 antibody was produced in chickens by injecting N-terminal 6-His-tagged fusion protein of human EEA1 residues 32-218. Polyclonal clathrin antibody was produced in rabbits by injecting the last 15 amino acids of the clathrin heavy chain. Polyclonal Rabenosyn-5 antibody was produced in rabbits by injecting residues 137-784 of human Rabenosyn-5. Additional antibodies were obtained as follows: APPL1 and GAPDH from Cell Signaling Technologies; TfR from Invitrogen, and EGFR from Millipore. Unconjugated, DyLight-649– and DyLight-488–conjugated human Tf were obtained from Jackson Immunoresearch.

Plasmids – TagRFP-T in pcDNA3 and TagRFP-T-clathrin were gifts from Roger Y. Tsien (University of California at San Diego, La Jolla, CA) and Michael W. Davidson (Florida State University, Tallahassee, FL), respectively. The TagRFP-T expression vector was constructed as described [125]. GFP-clathrin was a gift from J. H. Keen (Thomas Jefferson University, Philadelphia, PA). The cDNA clone 40034008 for human Rabenosyn-5 was obtained from American Tissue Culture Collection and was cloned in frame with EGFP or TagRFP-T at the N terminus of the protein using standard techniques. GFP-EEA1, from which TagRFP-T-EEA1 was subcloned, was described previously [126]. APPL1 [127]

was cloned in frame with EGFP and TagRFP-T at the N terminus of the protein using standard techniques. Human TfR in plasmid cDNA was a gift from Tim McGraw (Weill-Cornell Medical College, New York, NY). Human TfR cDNA was subcloned in frame with EGFP in the Clontech pEGFP-N1 vector at the XhoI and BamHI restriction sites.

TIRF/Epi-fluorescence Structure-illumination Microscope (TESM) optical system – A custom- built microscope system, TESM, simultaneously combines Total Internal Reflection Fluorescence and wide-field epifluorescence modes and incorporates structured illumination in the epi mode for fast optical sectioning and enhanced spatial resolution. Briefly, two Cobolt diode pumped solid state (DPSS) 100mW lasers produce 491 nm and 561 nm light. A 120mW diode laser from Blue Sky Laser produces 660 nm light. The three beams were combined using mirrors and dichroics before being split by a 50/50 beam cube and coupled into a single mode fiber for the TIRF illumination path and a beam expander for the epi-illumination path. The output of the lasers and the epi and TIRF channels was controlled by a set of five computer-controlled shutters. The output of the TIRF fiber was collimated by a lens and the fiber was positioned using a 3 axis translation stage to adjust focus and input TIRF angle. The epi beam passed through a Ronchi ruling that was moved by a computer controlled Physik Instruments translation stage. A modified Olympus IX71 microscope was used and the TIRF and epi beams were combined and directed into the microscope

using a 50/50 beam splitter at the lower illumination port. TIRF illumination was introduced though the edge of an Olympus TIRF 60X objective with an NA of 1.49 at an angle set to visualize 100-200 nm from the coverslip. A Physik Instruments PIFOC was used for fine focus control. The Ronchi ruling in the epi path was positioned so that the internal optics of the microscope and the 60X objective formed an image of the ruling at the sample. Light is collected and relayed through a triple bandpass filter cube and an output filter wheel onto a 1004x1002 Andor iXon 885 emCCD camera, which was binned at 2x2. The electron multiplier gain was set at 10. The Olympus IX71 microscope was contained in a heated chamber held at 35°C.

TESM imaging hardware and software – TESM acquisition system uses the following components: Super Micro workstation (SYS-7045A-WTB, San Jose, CA) with two 2.33GHz E5410 Xeon processors with 16GB of ram running Fedora 13x86_64; Instrutech ITC-18 data acquisition system with a USB-18 adapter (Heka, NY); 250GB system drive (ST3250310NS, Seagate), two 750GB data drives (ST3750330NS, Seagate) and one 1TB backup drive (ST31000340NS, Seagate). The two 750GB drives are in a RAID-0 configuration. mManager by USCF (http://www.micro-manager.org/) was used as the acquisition software. mManager was extended with three additional hardware device adapters developed or modified by the UMass Medical Biomedical Imaging Group. The Andor camera device adapter was ported to the 64 bit Linux operating system. A

new Cobolt adapter (https://valelab.ucsf.edu/~nico/MMwiki/index.php/Cobolt) controls the laser power and other settings. A new ITC18 adapter (https//valelab.ucsf.edu/~nico/MMwiki/index.php/ITC18), controls the ITC18 (Heka, NY) (http://www.heka.com/physio/equipment/interfaces/itc18.html). All changes and new software was contributed back to mManager. The ITC18 adapter is the heart of the imaging system and allows for high speed triggering of the camera in synchronization with 5 shutters (2 x UniBlitz VMM-D3, Vincent Associates, Rochester, NY), 1 filter wheel (Lambda 10-2, Sutter, Novato, CA), and 2 pifocs (Physik Instrumente, Irvine, CA).

TIRF time series imaging – The TIRF time series protocol used three lasers emitting at 491 nm and 561 nm, with 525/50- and 590/50-nm emission filters, respectively, and 660 nm, with >690 nm emission. By using four-color (blue, green, orange-red, far-red) 0.2-µm TetraSpeck microspheres (Invitrogen), it was determined that the focus (and magnification) of the green (525 nm) and red (590 nm) emission were identical, whereas the far-red (690 nm) focus was shifted by 500 nm. Correspondingly, the focus of the microscope was shifted by this amount using a PIFOC objective scanner (Physik Instruments) when acquiring the far-red images.

TESM 3-D imaging – The same lasers and emission filters were used in the TESM imaging protocol as in TIRF alone. Typically, each set of images

contained one TIRF image followed by three structured light images. The grating was moved by one-third of a period (~2 ms) between each image. The period of the grating was 500 line-pairs/in; with the 60X objective, the first-order period at the specimen was measured to be 0.456 microns, and no higher orders were observable. The focus was adjusted by 0.1 microns between every set of images for a total range of 10 microns.

TIRF image analysis – For quantitative image analysis, TIRF time series images were first smoothed by performing a temporal running average of three time points to reduce noise with a negligible effect on data. Next, the background fluorescence for each image was calculated as the mean intensity in a region of interest (typically 21x21 pixels) outside the cell and subtracted from all pixels.

Segmentation of vesicles from background. To generate images in which vesicles or other fluorescence structures can be analyzed without interference from diffuse fluorescence, images then were convolved with a DOG filter consisting of (i) a small 2D Gaussian spot with a unit area (σ = 150 nm) that acted as a vesicle-matched detector (i.e., an approximation to a near-diffraction limited spot) and (ii) a larger, inverted 2D Gaussian spot (σ = 300 nm) with negative unit area that estimated and subtracted the local background. The Gaussian smoothed images were thresholded visually (global threshold) to select for pixels belonging to objects (e.g., vesicles) and to eliminate areas devoid of

signal but containing noise.

Colocalization. For colocalization analysis, image sets dual labeled or triple labeled with Tf-DyLight 649 were processed as above. For each label, its globally thresholded image was used to generate a binary image by setting the intensity of all positive-value pixels to one and all other pixels to zero. Colocalization was determined by two-way or three-way binary image overlap among the labels. Colocalization values are reported as the percent of pixels that are colocalized with a given label. Given a pair of 2D binary images of labels “A” and “B,” the colocalization of B with A at time t is

$100 \cdot \Sigma_x \Sigma_y (A(x,y,t) \cdot B(x,y,t)) / \Sigma_x \Sigma_y B(x,y,t)$

Images of two-way and three-way colocalization are displayed using the running-averaged, background-subtracted images (colored as green and red or as green, red, and blue), with the colocalized pixels (defined above) shown as white, as indicated by the accompanying color wheels (Figures 2.1 and 2.3) [128].

Transferrin Trafficking. To analyze the trafficking of Tf, the thresholded-DOG time series image of an endocytic marker (clathrin, Rabenosyn-5, APPL, EEA1) was analyzed to identify individual objects (spots, vesicles) and their central (x,y,t) positions in every time point by finding all 2D intensity maxima (pixels brighter than their eight neighbors) and thresholding the maxima to eliminate spurious peaks. The average local fluorescence within a 5x5 pixel region

centered at each (x,y,t) position was obtained in both the running- averaged, background-subtracted endocytic marker image and the corresponding Tf image. From this value, the average fluorescence of a one-pixel- wide frame surrounding the 5x5 pixel region was subtracted (e.g., Figure 2.1B). The fluorescence ratio of Tf to endocytic marker was calculated for each object position, and the mean ratio and SE for each time point was calculated (typically there were hundreds of objects in each time point) and plotted (e.g., Figures 2.1C and 2.3B). The fluorescence ratio was used as an estimate of the (relative) Tf concentration associated with each object (both signals should be in roughly some proportion to the amount of surface membrane) while also correcting for the exponential decrease in fluorescence brightness with increasing depth in TIRF. Additionally, the kinetics of trafficking of Tf through clathrin, Rabenosyn-5, and APPL1 were modeled, and the models were fit to the ratio time-course data to determine rates of entry/filling and exiting/emptying of Tf for each endocytic marker. Details of the kinetic models and fitting are given in the curve fits to ratio data below.

Curve fits to ratio data – The Tf/Clathrin ratio data were fit with a simple kinetic model:

$$\text{Tf} + \text{clathrin} \underset{k_{on}}{\overset{k_{off}}{\leftrightarrow}} \text{Tf-clathrin} \xrightarrow{k_{empty}} ?$$

The TfR is modeled as having two binding sites for Tf, one low affinity and one high affinity. TfRs are assumed to be in instantaneous, steady-state colocalization with clathrin, independent of binding Tf, therefore clathrin is a

proxy for TfR. Tf/Clathrin is [Tf-Clathrin] (times a scale factor). The extracellular [Tf] is stepped from zero to a constant concentration, and the increase in the total Tf-TfR, and therefore Tf-clathrin, is proportional to $1-e^{-k\cdot t}$ where k is the sum of the on and off rates for Tf plus a rate k_{empty}, the rate at which Tf apparently disassociates from clathrin objects. This may be because Tf in fact disassociates from a clathrin object, or a Tf-clathrin object disappears from the TIRF imaging zone (and is replaced by a clathrin-alone object, preserving the steady state). Conversely when the [Tf] is stepped back to zero, the Tf-clathrin decreases as $e^{-k\cdot t}$ where $k_{on}\cdot[Tf]$ is now zero since [Tf] is zero. The two Tf binding sites are assumed to be independent, so the equations for the ratio, $R(t)_{clathrin}$ are:

$$R(t \le t_{add})_{clathrin} = 0$$

$$R(t_{add} < t \le t_{wash})_{clathrin} = A\cdot\{(1-e^{-k1\cdot t}) + (1-e^{-k2\cdot t})\}/2$$

$$R(t > t_{wash})_{clathrin} = R(t_{wash})_{clathrin}\cdot\{e^{-k1\cdot t} + e^{-k2\cdot t}\}/2$$

where A is an arbitrary constant to match the ratio data amplitude, and

$$k1 = k^1_{on}\cdot[Tf] + k^1_{off} + k_{empty}$$

$$k2 = k^2_{on}\cdot[Tf] + k^2_{off} + k_{empty}$$

The equations for $R(t)_{clathrin}$ were fit to the ratio data using a Levenberg–Marquardt least-squares fit algorithm, with t_{add}, t_{wash}, [Tf], A, and k_{empty} as parameters. [Tf] is either a constant ($t_{add} < t < t_{wash}$) or 0. Tf binding rate constants used are $k^1_{on}=1.0\cdot10^5\ M^{-1}s^{-1}$ and $k^1_{off}=3.2\cdot10^{-3}\ s^{-1}$, and $k^2_{on}=8.3\cdot10^5\ M^{-1}s^{-1}$ and $k^2_{off}=1.0\cdot10^{-3}\ s^{-1}$ [129].

The Tf-rabenosyn (or Tf-APPL) ratio data were fit with a similar model, except

that for the association of Tf with rabenosyn-5, we assume that the Tf must pass through the clathrin pathway to be available to taken up in rabenosyn-5 vesicles.

$$\text{Tf-clathrin} + \text{Rbsn} \xrightarrow{k_{fill}} \text{clathrin} + \text{Tf-Rbsn} \xrightarrow{k_{empty}} ?$$

where $k_{fill} = k_{on} \cdot [\text{Tf-clathrin}] \cdot [\text{Rbsn}]$

This yields the differential equations for the change in rabenosyn-5

$$d[\text{Rbsn}]/dt = k_{empty} \cdot [\text{Tf-Rbsn}] - k_{on} \cdot [\text{Rbsn}] \cdot [\text{Tf-clathrin}]$$

$$d[\text{Tf-Rbsn}]/dt = k_{on} \cdot [\text{Rbsn}] \cdot [\text{Tf-clathrin}] - k_{empty} \cdot [\text{Tf-Rbsn}]$$

$[\text{Rbsn}]+[\text{Tf-Rbsn}]$ is assumed to be constant. We used $R(t)_{clathrin}$ (see above) as the [Tf-clathrin] driving the association with rabenosyn-5 at time t , yielding

$$d[\text{Rbsn}]/dt = k_{empty} \cdot [\text{Tf-Rbsn}] - k_{on} \cdot [\text{Rbsn}] \cdot R(t)_{clathrin}$$

$$d[\text{Tf-Rbsn}]/dt = k_{on} \cdot [\text{Rbsn}] \cdot R(t)_{clathrin} - k_{empty} \cdot [\text{Tf-Rbsn}]$$

[Tf-Rbsn](t) is related to the observed ratio by an unknown scale factor, i.e., $R(t)_{rabenosyn} = B \cdot [\text{Tf- Rbsn}](t)$. The system of ordinary differential equations was numerically integrated (for a given B, k_{on} and k_{empty}) using the ODE function of Scilab (http://www.scilab.org/) producing [Tf-Rbsn], and hence $R(t)_{rabenosyn}$. Initial conditions were [Rbsn] =1 and [Tf-Rbsn]=0.This function was fit to the Tf-rabenosyn-5 ratio data using the L-M method, with B, k_{on} and k_{empty} as parameters (i.e., the ODE solver was called interatively with different values for B, k_{on} and k_{empty} until $R(t)_{rabenosyn}$. matched the Tf/rabenosyn-5 ratio data sufficiently closely.

For each 3-color experiment (Tf, clathrin, rabenosyn-5 or APPL), the ratio time courses of Tf/clathrin and Tf/rabenosyn-5 were calculated as describe above.

First, $R(t)_{clathrin}$ was fit to the Tf/clathrin ratio. Then $R(t)_{rabenosyn}$ was fit to the Tf/rabenosyn ratio using the resulting $R(t)_{clathrin}$. While $R(t)_{clathrin}$ is not a concentration, it is only the product k_{fill} (not k_{on}) that matters. As k_{fill} is not constant over time, for each experimental data set a "near-steady-state" value of k_{fill} was calculated at $t=t_{wash}$.

TESM 3-D image analysis – Optical sectioned images of epifluorescence were produced from the structured illumination data sets according to the method of Tony Wilson [108]. Briefly, at each focal position and for each emission wavelength, a single optical section image, I, was computed from a triplet of images acquired sequentially with the illumination grating shifted by one-third period each time ($I_{0/3}$, $I_{1/3}$, $I_{2/3}$) as

$$I = [(I_{0/3} - I_{1/3})^2 + (I_{1/3} - I_{2/3})^2 + (I_{2/3} - I_{0/3})^2]^{1/2}$$

Colocalization. Optical section images of endogenous proteins (antibody-labeled and fixed) were convolved with a 2-dimensional DOG filter with the positive unit area Gaussian sigma = 75nm, and the negative unit area Gaussian sigma=150 nm. Selected focal positions of the DOG images were used to generate binary images as described above. Colocalization between proteins was determined by two or three way binary image overlap.

TESM Z-position maps. False colored maps of axial (z) position of fluorescence

were created from the combination of TIRF and optical section images. TIRF images confound “intrinsic” fluorescence brightness with axial position. If the actual brightness is known then the axial position can be recovered. The Epifluorescence- structured illumination optical section images were used as indicators of actual in-focus fluorescence brightness. Briefly, the 3-D TIRF images of both 491 and 561 nm illuminations were inspected to determine a single, nearest to the coverslip (in 100 nm steps) plane of best focus, z0, of all the visible structures. The TIRF and the optical section image stacks at both wavelengths were then segmented to span from z0-2 to z0+4, or 700 nm of depth, and a single “extended focus” image of both TIRF and epifluorescence was made by maximum intensity projection of these 7 planes, yielding a set of four images [$^{491}I_{TIRF}$, $^{491}I_{epi}$, $^{561}I_{TIRF}$, $^{561}I_{epi}$]. These images were thresholded to excluded areas devoid of signal.

Because there is a microscope system dependent and illumination wavelength (λ) dependent difference in excitation efficiency between the TIRF and epi-illumination paths (the emission path is the same), there is a scale factor $^{\lambda}K$ relating the intensity of the TIRF image $^{\lambda}I_{TIRF}$ to the epi image $^{\lambda}I_{epi}$. If the e^{-1} penetration distance d of the TIRF evanescent field is known, then image Z of axial positions of fluorescent sources in the field can be calculated as

$$Z=-^{\lambda}d\cdot\ln[^{\lambda}K\cdot{}^{\lambda}I_{TIRF}/{}^{\lambda}I_{epi}]$$

$$Z=-^{\lambda}d\cdot\ln[^{\lambda}I_{TIRF}/{}^{\lambda}I_{epi}] + (-d\cdot\ln[^{\lambda}K])$$

$$Z=-^{\lambda}d\cdot\ln[^{\lambda}I_{TIRF}/{}^{\lambda}I_{epi}] + {}^{\lambda}z_0$$

The value of z_0 depends on d and K and is constant as long as the microscope set up is constant. There is an axial apparent offset between the wavelengths $\Delta Z = ({}^{491}Z_0 - {}^{561}Z_0)$. This offset was determined empirically using dual-color microspheres and is described below in calibration of TESM using dual labeled beads.

Calibration of TESM using dual labeled beads –To validate the combined use of SLE and TIRF to determine the position of endosomes within the depth of the TIRF zone (z-map), apparent differences in z-position due to wavelength differences in the TIRF vs. SLE between the green and red excitation and emission paths must be distinguished from real positional differences. To determine the differences in z-position attributable to specific fluorophore wavelengths, dual (green/red) labeled beads (Tetraspec, Invitrogen) were embedded in agarose and dried onto the coverslip, mimicking a cell milieu with fluorescent vesicles at different positions. Beads were then imaged in TIRF and SLE, identified in the SLE reconstruction, and processed to calculate their z-position as $z = -d * \ln [I(TIRF) / I(SLE)]$, using d=132 nm for green and d=150 nm for red. These values were derived from the emission wavelengths (~530 nm and ~590 nm) and the setting of the TIRF angle micrometer.

Figure 2.12 shows the positions of the beads calculated using the fluorescence in red vs the fluorescence in green. Larger z (to the right and up) is farther from the coverslip. The slope of the data was 0.99, indicating that the relative d values

TIRF angle	64 degree
depth constant (d)	132.5 nm
Fig 1 z-map max (red)	398 nm

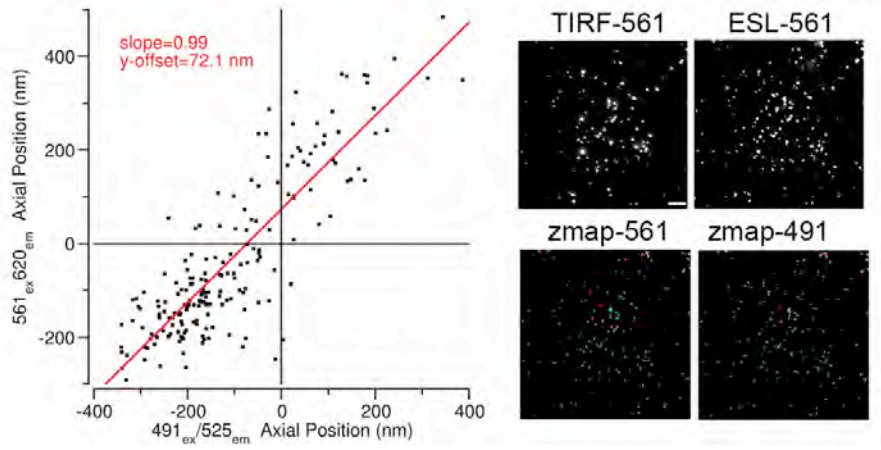

Figure 2.12. Calibration of z-map position using dual labeled beads. The zmap images of the cel s were obtained by taking the -d * ln [I(TIRF) / I(SLE)] in the whole image calculated pixel by pixel and masked by thresholding the SL(561) image. The calibration of the z-depth colorbar was based on the use of a ~64 degree TIRF angle. The calculation of the depth penetration of TIRF is

d = wl / [4*pi* sqrt(n1^2 sin()^2 - n2^2)]

where wl is the emission wavelength center (520nm) and n1 = 1 52 (glass) and n2 = 1.33 (water).

are correct. The intercept is the offset between the colors attributable to wavelength. The TIRF and ESL images of beads in the 561 wavelength are shown on the right. The raw images in the 491 wavelength were virtually indistinguishable, and the obtained z- maps of the same beads reveal very good correspondence between the two wavelengths when the offset is incorporated into the calculation.

Biochemical measurement of Tf trafficking – Cells were treated with scrambled (control) or Rabenosyn-5 siRNA as described. At 48 hours knockdown cells were replated on black 96 well plates at a density of $1.5x10^4$ cells per well and cultured for an additional 24 hours at 37°C 5% CO_2. Serum Tf was removed by incubation in DMEM (Invitrogen) supplemented with 1% ovalbumin (Sigma) for 1 hour at 37°C 5% CO_2. To determine the number of TfR on the cell surface, cells were incubated on ice with DMEM supplemented with 1% ovalbumin containing 10µg/ml peroxidase-conjugated human transferrin (Tf-HRP) (Jackson ImmunoResearch). After 2 hours cells were washed and peroxidase activity was detected using SuperSignal ELISA Pico Chemiluminescent Substrate (Pierce) using a Tecan Safire2. To measure internalization rates, cells were incubated at 37°C with DMEM containing 1% ovalbumin and 10µg/ml Tf-HRP. At the times indicated in each figure cells were placed on ice and washed three times with chilled PBS supplemented with 5% ovalbumin and three times with neutral pH buffer supplemented with 1% ovalbumin. Half the wells were then exposed to

chilled pH 2.0 buffer (500mM NaCl, 0.2N glacial acetic acid, pH 2.0) for 5 minutes at 4°C. Cells were washed twice with neutral pH buffer and once with PBS, and chemiluminescence detected as described above. Internalized Tf was defined as the difference in signal between acid washed (internalized) and non-acid washed (total) wells. To measure recycling rates, cells were incubated at 37°C 5% CO_2 for 2 hours in DMEM supplemented with 1% ovalbumin containing 10µg/ml Tf-HRP. Cells were washed once with PBS supplemented with 5% ovalbumin and incubated in pH 5.0 butter (150mM NaCl, 50mM MES, pH 5.0) at room temperature for 2 minutes. Cells were washed three times with prewarmed efflux media (DMEM supplemented with 100µM desferoxamine and 10µg/ml human transferrin). At the times indicated media was removed and chemiluminescence in the media detected as described above. In each experiment values obtained in the presence of a 200-fold excess of unconjugated human transferrin were subtracted to obtain specific signal. Means and SEM are for three independent experiments performed in quadruplicate.

CHAPTER III

ROUTES OF SIRNA INTERNALIZATION AND ENDOSOMAL COMPONENTS REQUIRED FOR SILENCING

ABSTRACT

Effective intracellular delivery of siRNA is a major obstacle in antisense oligonucleotide drug development. Using chemically modified and phosphorothioated sd-rxRNA®, we describe the efficient delivery and identify the endocytic mechanisms of a proprietary self-delivering siRNA. Sd-rxRNA is actively internalized into Rabenosyn-5 and EEA1 positive endosomes and knockdown of EEA1 inhibits sd-rxRNA silencing indicating EEA1 plays a crucial role in the initial uptake of self delivering siRNA. The sd-rxRNA enter and function through the lysosomal degradative pathway and remain separate from the endocytic recycling pathway. Taken together, these data suggest that sd-rxRNA is internalized into specific populations of endosomes and the presence of EEA1 is required for silencing of the sd-rxRNA target.

INTRODUCTION

RNA interference (RNAi) is a naturally occurring cellular process in eukaryotes whereby double stranded RNA (dsRNA) association with the RNA induced silencing complex (RISC) targets complementary messenger RNA

(mRNA) sequences and silences target genes. RNAi is regarded as a revolutionary discovery in biology, jointly awarding scientists Craig C. Mello and Andrew Z. Fire the Nobel Prize in Physiology or Medicine in 2006. RNAi is a naturally occurring, highly conserved, cellular process in eukaryotes by which short dsRNA results in sequence-specific gene silencing through mRNA degradation [130,131]. The RNAi pathway (Figure 3.1) is first initiated by Dicer, an enzyme that cleaves dsRNA into shorter dsRNA fragments known as small interfering RNAs (siRNAs) [132]. The approximately 20 nucleotide length siRNA is composed of guide strand, which is incorporated into RISC, and a passenger strand that is degraded [133]. The catalytic component of the RISC complex is Argonaute-2 (Ago2). Ago-2 will cleave guide strand RNA complementarily paired to mRNA. The cleavage of mRNA prevents this mRNA from being translated, thereby silencing the gene. Cytoplasmic bodies, also called processing bodies (P-bodies) and GW-bodies, are the specific sites of mRNA degradation where Ago-2 and GW182 are localized [134]. GW182 is required for P-body stability and RNAi gene silencing as knockdown of GW182 disrupts P-body formation and impairs silencing by siRNA [135]. The discovery that small chemically synthesized siRNAs introduced into mammalian cells also results in efficient sequence-specific gene silencing [79] launched the potential for this process to be harnessed as a therapeutic. While the use of RNAi as a therapeutic strategy is intellectually exciting, successful RNAi compound delivery faces many clinical obstacles.

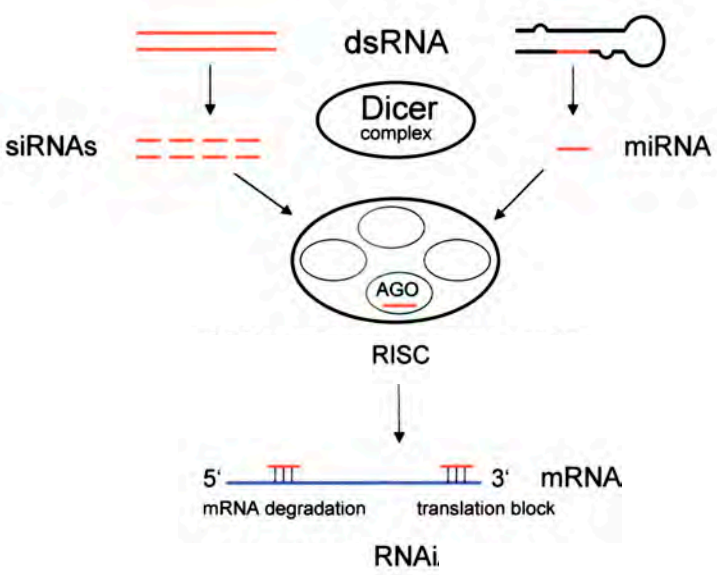

Figure 3.1. RNA mediated silencing. Short RNAs derived from Dicer cleavage of dsRNA are incorporated into multiprotein effector complex, RISC, to target mRNA degradation (RNAi). Argonaute (AGO) proteins bind short RNAs and 'shepherd' them to appropriate effector complexes. Target nucleic acids are shown in blue, short RNAs in red, proteins and enzyme complexes as ovals. Figure modified **from Matzke & Matzke PLoS Biol. 2004 May;2(5):E133. Epub 2004 May 11.**

Successful delivery to and entry into the cells of interest are major challenges in the use of siRNA as a therapeutic. Potential caveats of systemically administered siRNA therapies are degradation by nucleases found in blood, clearance of siRNA from circulation by the kidneys, cellular targeting, passing through the plasma membrane into the cytoplasm, and uptake by RNAi machinery. The negative charge of siRNA molecules means that the negatively charged cell membrane poses a great barrier for siRNA uptake. As a result, lipid carriers, nanoparticles, cholesterol modifications, antibodies, or other methods must overcome the barrier of the plasma membrane. Once a delivery vehicle has promoted cellular uptake of siRNA, the siRNA must then be able to associate with RNAi machinery.

In plants RNAi is initiated by dsRNA [136] that can be transported to distant cells through the phloem [137]. Studies in *Drosophila* S2 cells show that when scavenger receptors are knocked down, internalization of dsRNA decreases by over 90% [138]. Further evidence for dsRNA internalization by scavenger receptors comes from expression studies in CHO cells. CHO cells stably expressing *Drosophila* scavenger receptors were able to take up substantially more dsRNA than control cells [138]. These studies indicate that scavenger receptors could be mediating endocytosis of dsRNA, however dsRNA associating with a lipid or growth factor and being internalized through a carrier's endocytic pathway has not been ruled out.

Systemic RNAi defective-1 (SID-1) is a transmembrane protein in *C. elegans* that localizes to the cell periphery and is necessary for cells to import dsRNA and for silencing by external dsRNA [139]. Studies of exogenous SID-1 expressed in *Drosophila* S2 cells confirmed that SID-1 mediates cellular uptake of dsRNA at a much lower dsRNA concentration than these cells are normally able to internalize [140]. A mammalian homolog of *C. elegans* SID-1, SidT1, when overexpressed has been shown to localize to the cell membrane and enhance siRNA uptake and increases gene silencing in human pancreatic ductoral adenocarcinoma cells [141]. Knockdown of endogenous SidT1 resulted in decreased lipoprotein-associated cholesterol-siRNA uptake in primary mouse hepatocytes [142].

A genetic screen in Drosophila S2 cells revealed that components of RNAi and endocytic machinery are required for uptake and processing of dsRNA [143]. Genes required for RNAi silencing include Dicer, Argonaute-2 (Ago-2), clathrin heavy chain, Rab7, and vacuolar H^+-ATPase [143]. Dicer and Ago-2 are both part of the RNAi machinery. Dicer specifically cleaves dsRNA to generate microRNA and it has been shown that knocking out Dicer impairs microRNA processing [144,145]. Ago-2 is an essential component of RISC involved in mRNA cleavage and RNAi is impaired in cells lacking Ago-2 [146]. The surprising results of this screen were the components of the endocytic machinery. Clathrin heavy chain is required for clathrin mediated endocytosis while Rab7 is a known regulator of late endocytic traffic [147]. The vacuolar H+-

ATPase is required for maturation of multivesicular bodies (MVB) [148], late endosomes whose membranes have internally budded resulting in the accumulation of multiple luminal vesicles.

MVBs can proceed along the degradative pathway and fuse with lysosomes, degrading their cargo. Alternatively, MVBs can fuse with the plasma membrane, releasing their accumulated luminal vesicles as exosomes [149]. Exosomes have been shown to contain functional microRNAs (miRNAs) [150,151] that can be taken up by other cells [151], suggesting a role for MVBs in the RNAi pathway.

A potential functionally important link between the RNAi machinery and the endosomal pathway was published in back-to-back manuscripts in 2009 [100,101]. Membrane fractionation of monocytes on density gradients found GW182, Ago-2, and a mature miRNA localized to the MVB fraction [100]. Additionally, knockdown of hepatocyte growth factor-regulated tyrosine kinase substrate (Hrs), a component of the endosomal sorting complex required for transport (ESCRT) pathway, which blocks MVB formation, inhibited miRNA silencing [100,101].

Taken together this data suggests that the RNAi machinery is localized to multivesicular endosomes found within the degradative pathway. In order to function, siRNA must reach the cell of interest, cross the plasma membrane, and traffic into the degradative pathway where it can be loaded into RISC to function. Utilizing a fluorescently tagged self-delivering siRNA we employed TIRF

microscopy and biochemical techniques to define the endosomes through which siRNA traffics and if the presence of those endosomal populations is required for functional silencing.

RNAi technology can be utilized to treat human diseases by shutting down genes that are known to lead to disease. RXi Pharmaceuticals is a pharmaceutical company pursuing the development and commercialization of RNAi based therapeutics for the treatment of human diseases. RXi Pharmaceuticals developed a novel class of self-delivering RNAi compounds (sd-rxRNA®) that is a proprietary technology that enables efficient cellular uptake in the absence of a delivery vehicle. Sd-rxRNA are chemically modified asymmetric RNA duplexes with a short duplex region of 11-15 base pairs and a fully phosphorothioated single stranded tail (Figure 3.2).

RESULTS

Utilizing TIRF microscopy sd-rxRNA was added to COS-7 cells and imaged at 1 Hz (one frame/second) continuously for 20 minutes. Figure 3.3A illustrates a time series from the image set. Within minutes of exposure to sd-rxRNA the cells have internalized the oligo into punctate structures. A caveat to previous studies of oligo transport has been the question of whether or not oligos are internalized through interactions with lipid binding proteins in the medium. To test whether or not sd-rxRNA requires the presence of a carrier protein for internalization we added it to COS-7 in a buffered solution lacking carrier

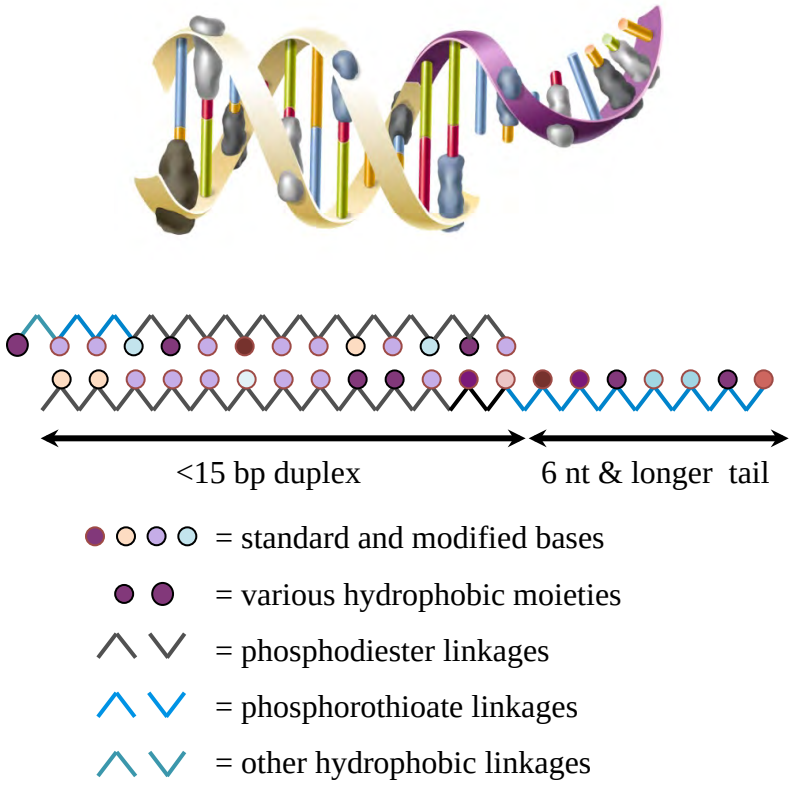

Figure 3.2. sd-rxRNAs are chemically modified to improve cellular uptake. The favorable pharmacokinetic (PK) properties of antisense oligonucleotides (ASOs) are believed to be based on the ability of a fully phosphorothioated single-stranded oligonucleotide to bind proteins and enter cells and tissues. Use of minimal length asymmetric RNAi compounds enable merging favorable PK properties of ASOs with the potency and duration of effect advantages, resulting from an RNAi mechanism of action. These compounds usually have a guide strand of 19 nucleotides and a passenger strand of 11-15 nucleotides, thus making an asymmetric compound with a 6-12 nucleotide single-stranded phosphorothioate tail. In addition, sd-rxRNA compounds are heavily modified with stabilizing and hydrophobic modifications (e.g. sterol), which confer stability, reduced inflammatory response and efficient cellular uptake . This complex chemical structure is essential for cellular delivery but does not interfere with the ability of the oligonucleotides to be efficiently recognized by the RNA Induced Silencing Complex (RISC) and induce RNAi. **Figure provided by RXi Pharmaceuticals.**

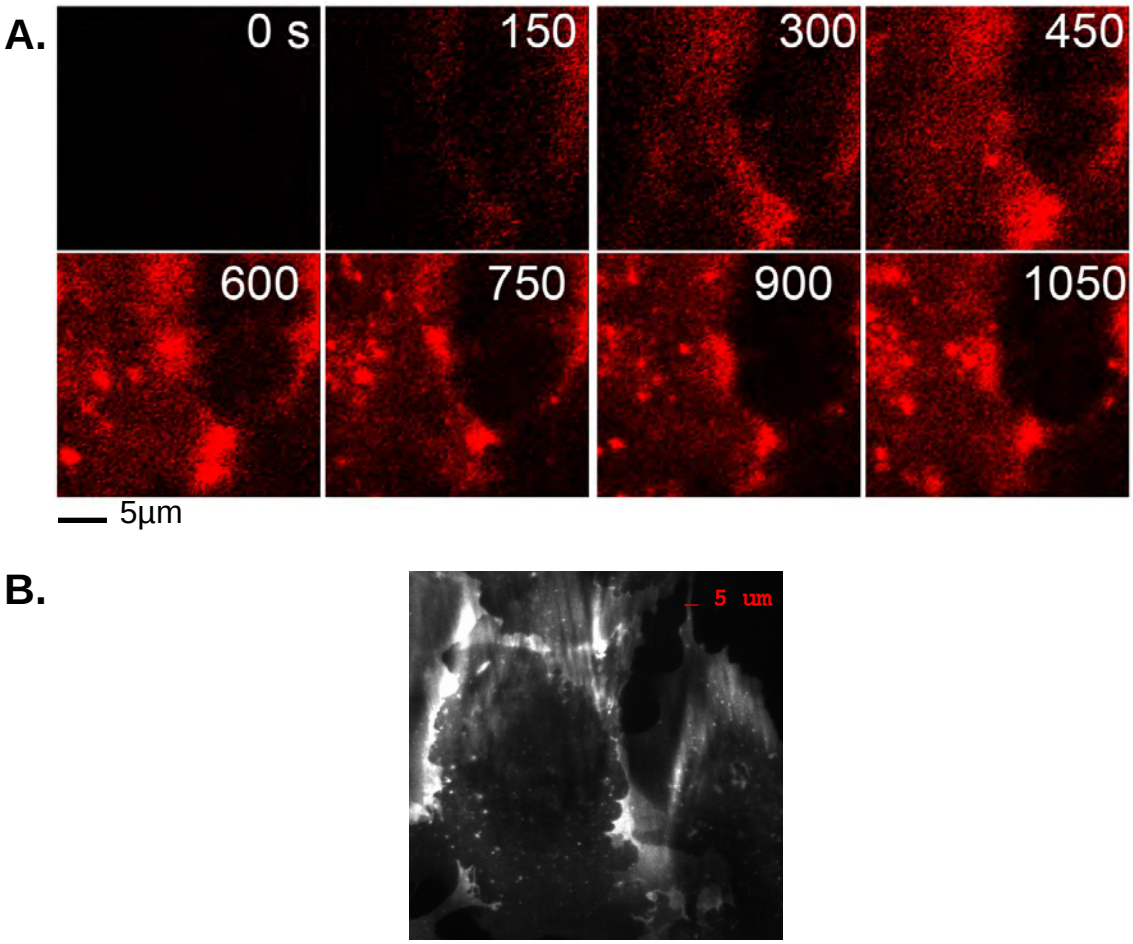

Figure 3.3. Efficient cellular uptake of sd-rxRNA by COS-7 cells. COS-7 cells were imaged by TIRF microscopy in the presence of 0.25µM sd-rxRNA. **A.** Time course demonstrates that sd-rxRNA is internalized in punctate structures within 10 minutes of exposure. **B.** Sd-rxRNA is efficiently internalized in the absence of any carrier proteins.

proteins. Figure 3.3B demonstrates that there was no change in sd-rxRNA internalization in the absence of carrier protein. To determine that internalization of sd-rxRNA is a specific endocytic process, we compared uptake of sd-rxRNA with that of the membrane dye FM4-64. FM4-64 is a lipophilic styryl, membrane selective, dye used as a marker for endocytosis [152,153]. As shown in Figure 3.4 FM4-64 is enriched in vesicles lacking sd-rxRNA. Given that sd-rxRNA is hydrophobically modified, this data suggests that sd-rxRNA is not being internalized by pinocytosis or fluid phase uptake at fatty areas of the membrane.

To address the question of which components of the endosomal system traffic sd-rxRNA, we added it to cells transfected with GFP-EEA1, GFP-Rabenosyn-5, GFP-APPL1, or GFP-WDFY2. Cells were imaged at 1 Hz continuously for 15 minutes. After 5 minutes of exposure to sd-rxRNA any unbound oligo was washed out of the bath. Figure 3.5A illustrates the same time frame of the resulting image set. While no association was found between sd-rxRNA and APPL1, and minimal between sd-rxRNA and WDFY2, significant amounts of the oligo were found in both EEA1 and Rabenosyn-5 enriched regions (Figure 3.5B).

Recent data from our laboratory indicate that Rabenosyn-5 is a crucial component of the endocytic recycling system involved in determining the recycling versus degradation fate of cargo internalized through clathrin coated pits while EEA1 captures cargo destined for lysosomal degradation [49,154]. In light of these findings we visualized the uptake of sd-rxRNA in conjunction with

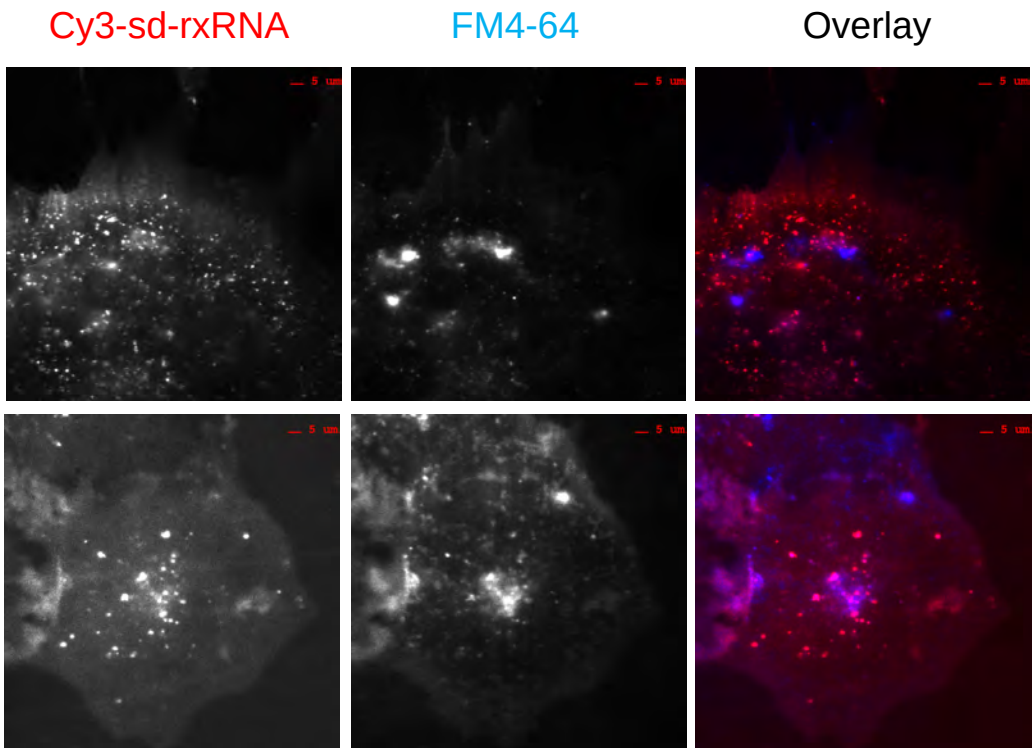

Figure 3.4. Cellular uptake of sd-rxRNA by COS-7 differs from fluid phase uptake. COS-7 were simultaneously exposed to 0.25µM sd-rxRNA (red) and 0.5µg/ml FM4-64 (blue) and imaged by TIRF microscopy.

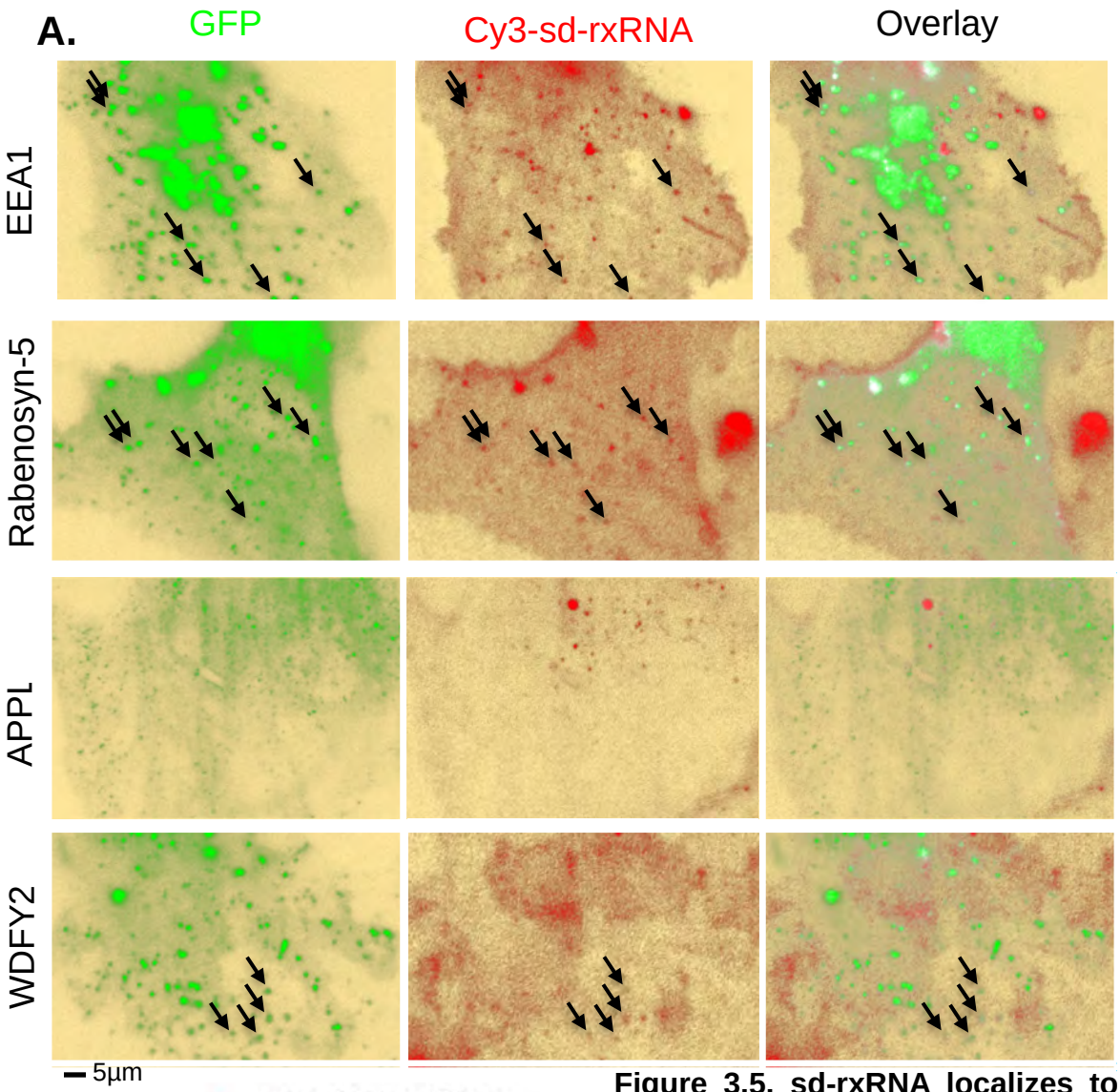

Figure 3.5. sd-rxRNA localizes to specific endosomal populations. **A**. COS-7 cells expressing GFP-EEA1, GFP-Rabenosyn-5, GFP-APPL1, or GFP-WDFY2 were exposed to 0.25µM sd-rxRNA and imaged by TIRF microscopy. Background has been pseudo colored yellow. Arrows highlight areas of colocalization. **B.** Quantification of sd-rxRNA colocalized with Rabenosyn-5 (red) or EEA1 (green) over time. n=4

the recycled ligand transferrin (Tf) and the degraded ligand epidermal growth factor (EGF). As depicted in the single frames of Figure 3.6, sd-rxRNA associates specifically with EGF while there is virtually no sd-rxRNA found in Tf positive regions. Given the abundance of the Tf signal in these cells, the association between sd-rxRNA and Tf was more closely examined by structured light Epifluorescence (SLE). With standard Epifluorescence in Figure 3.7 there is association between Tf and sd-rxRNA within the out of focus signal in the perinuclear region. When this signal is removed by imaging with high resolution SLE there is a negligible association between sd-rxRNA and Tf (Figure 3.7, insert). Conversely to the Tf data, when EGF and sd-rxRNA are added to COS-7 cells and imaged over time, the uptake of these two compounds is quite similar and shows specific overlap (Figure 3.8). This data suggests that sd-rxRNA follows an endocytic route similar to that of EGF, which is known to specifically and rapidly associate with EEA1 positive endosomes (Figure 3.9A). Closer of examination of sd-rxRNA internalization into GFP-EEA1 transfected cells reveals that the vast majority of punctate internalized oligo localizes to EEA1 positive endosomes (Figure 3.9B). Consistent with sd-rxRNA trafficking along the EGF positive EEA1 positive degradative pathway, sd-rxRNA is found localized to acidified vesicular structures as indicated by positive association with Lysotracker (Figure 3.10).

To examine the function of EEA1 in sd-rxRNA trafficking, we analyzed the effects of siRNA-mediated EEA1 depletion. COS-7 cells were treated with

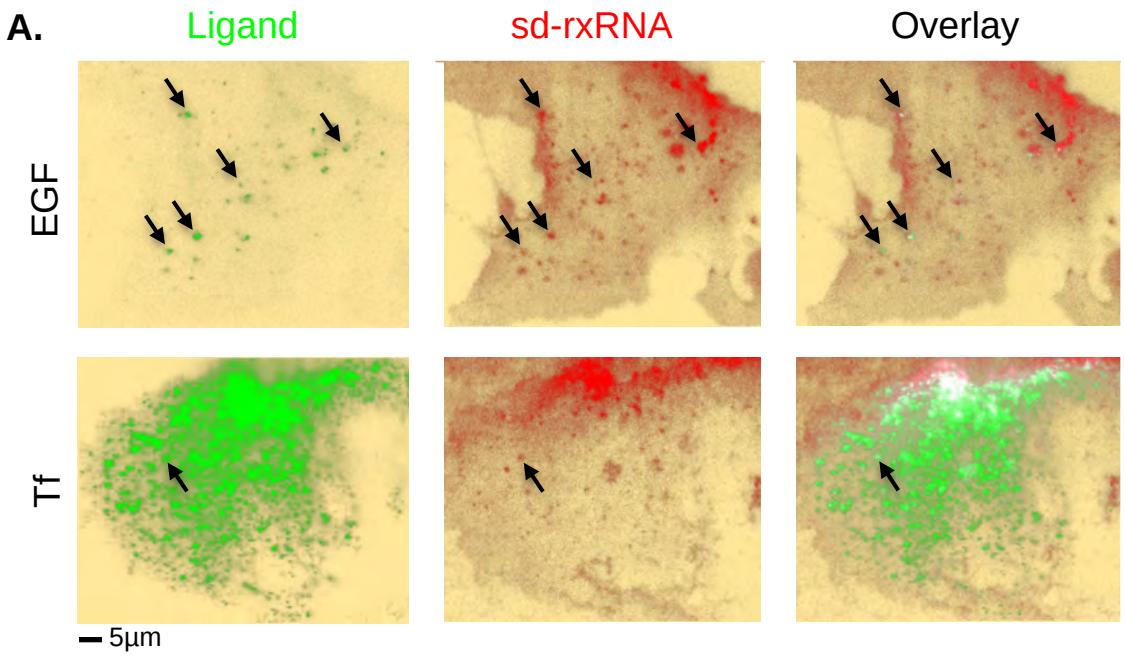

Figure 3.6. sd-rxRNA localizes EGF positive endosomes. A. COS-7 cells were simultaneously exposed to 0.25µM sd-rxRNA and 50ng/ml Alexa^{488}-EGF or 0.25µM sd-rxRNA and 10µg/ml Tf-DyLight-488 and imaged by TIRF microscopy. Background has been pseudo colored yellow. Arrows highlight areas of colocalization. **B.** Quantification of sd-rxRNA colocalization with EGF (black) or Tf (grey) over time. n=3-8

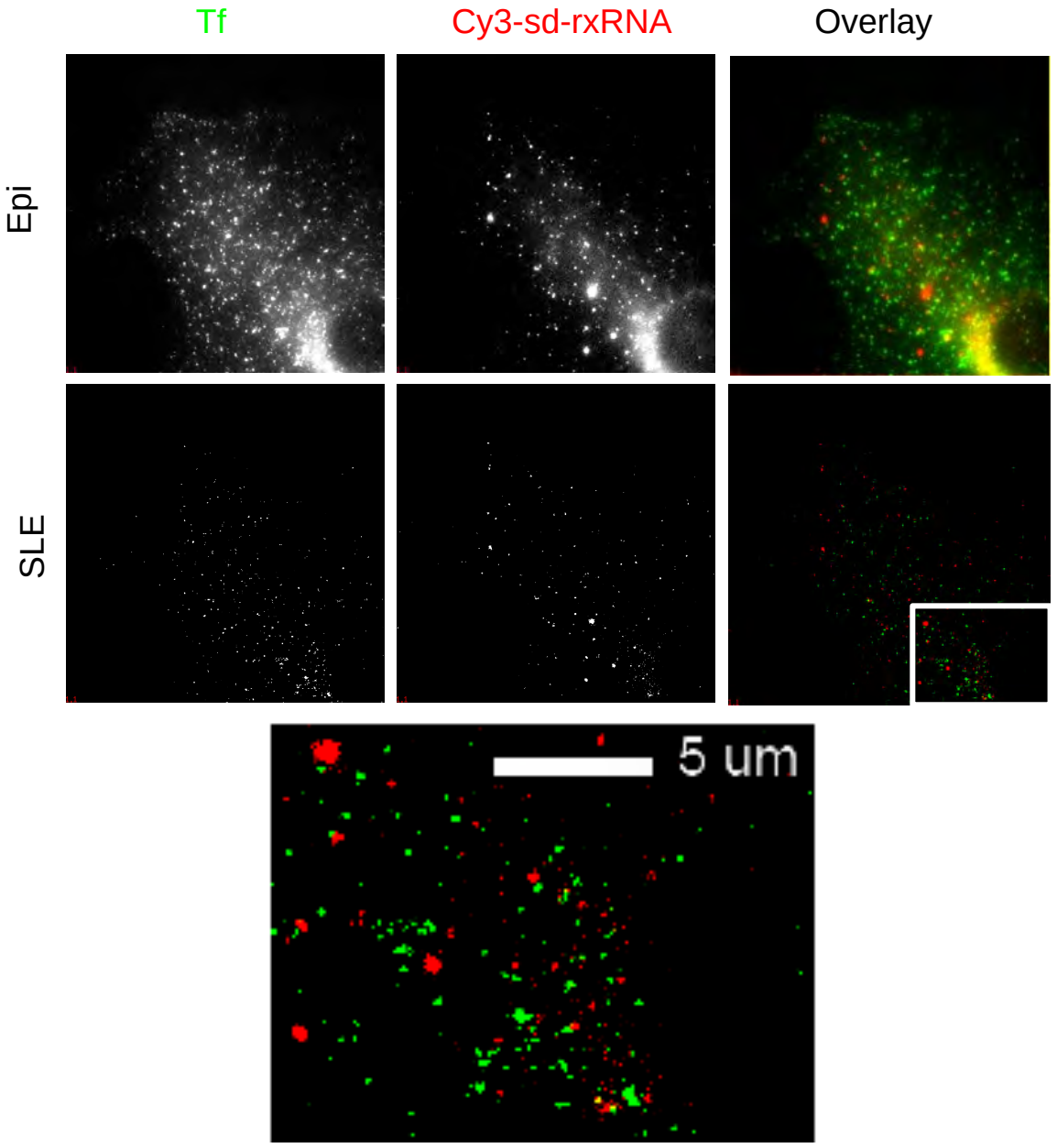

Figure 3.7. Transferrin and sd-rxRNA trafficking pathways differ. COS-7 cells treated with 0.25μM sd-rxRNA and 10μg/ml Tf and imaged by epifluorescence and structured light epifluorescence. Yellow pixels indicate colocalization.

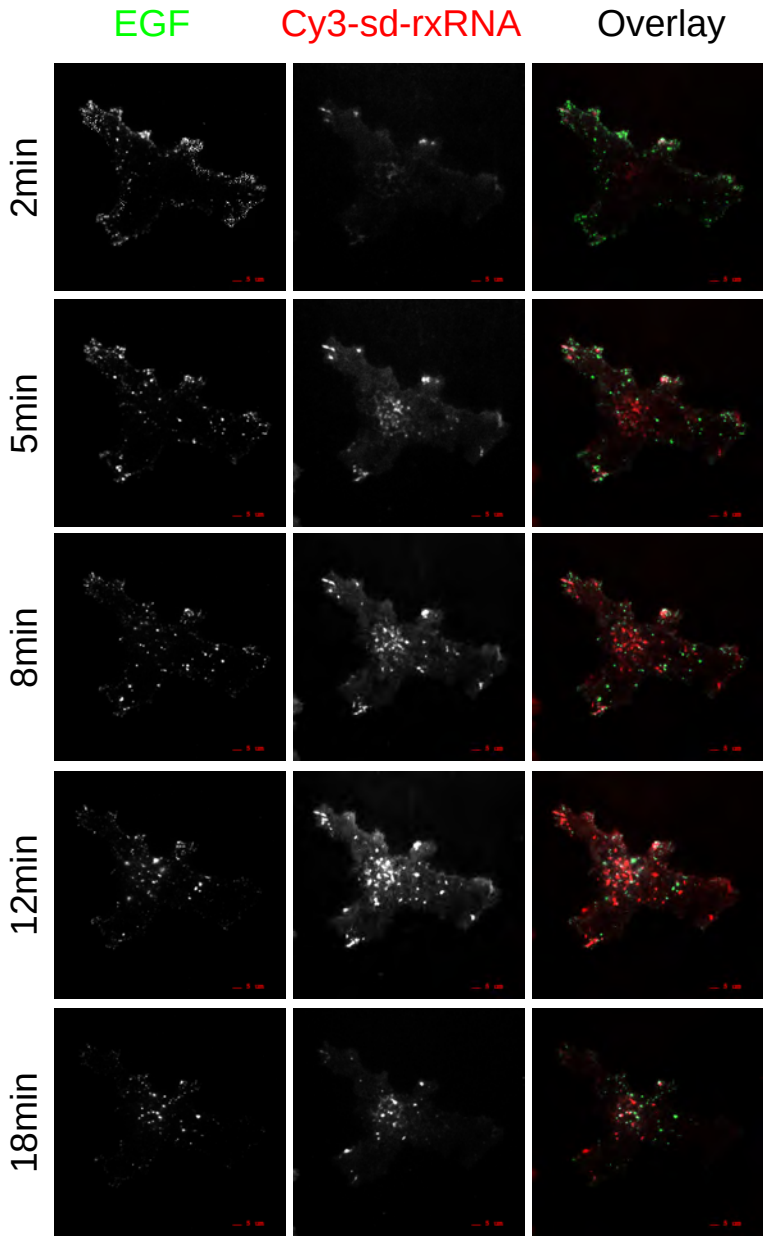

Figure 3.8. EGF and sd-rxRNA trafficking pathways are similar. COS-7 cells were simultaneously exposed to 0.25μM sd-rxRNA and 50ng/ml Alexa^{488}-EGF and imaged by TIRF microscopy. White pixels indicate colocalization.

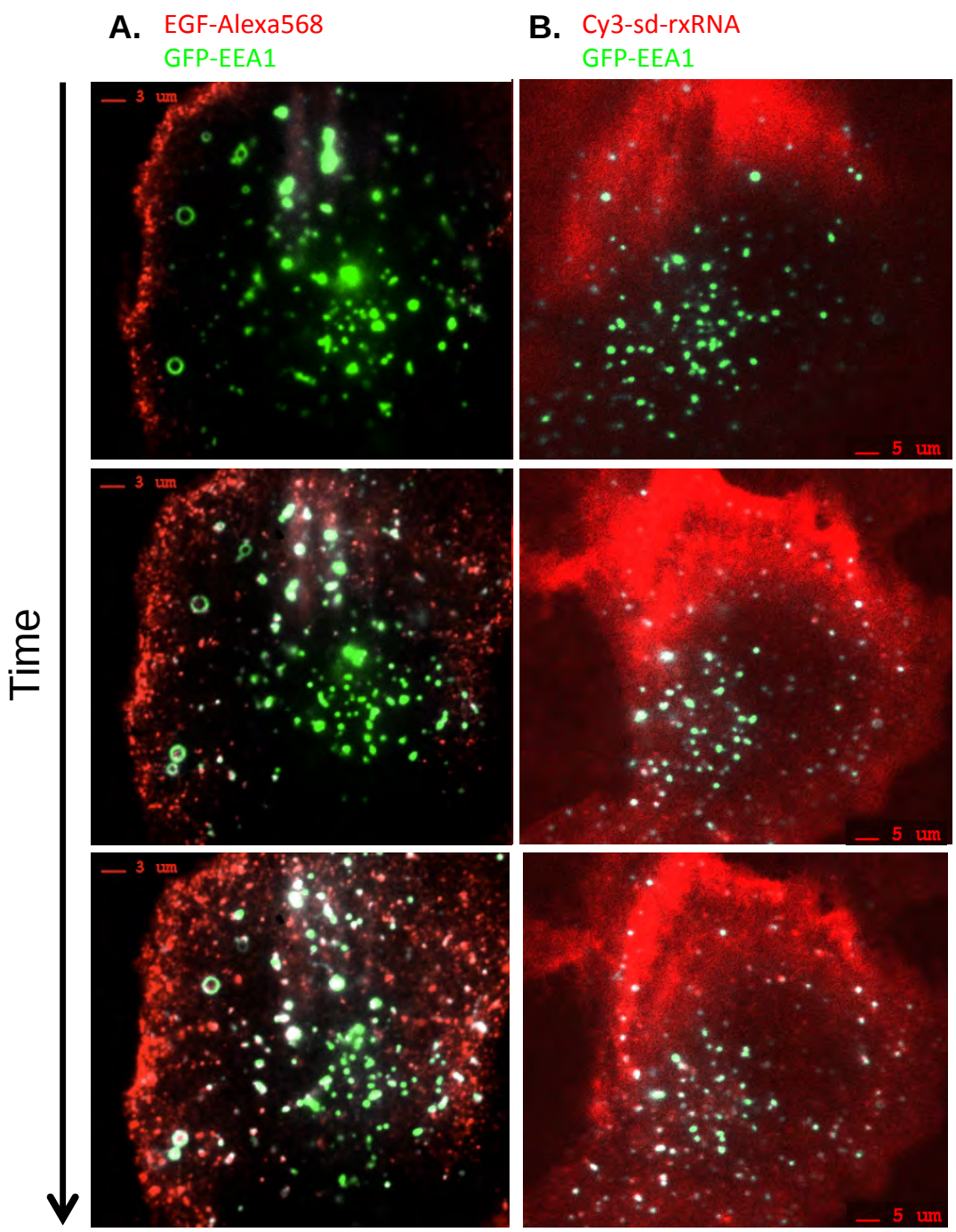

Figure 3.9. Visual comparison of EGF and EEA1 colocalization and sd-rxRNA and EEA1 colocalization. **A.** COS-7 cells expressing GFP-EEA1 were imaged by TIRF microscopy in the presence of 50ng/ml Alexa^{568}-EGF. White pixels indicate colocalized regions. **B.** COS-7 cells expressing GFP-EEA1 were imaged by TIRF microscopy in the presence of 0.25μM Cy3-sd-rxRNA. White pixels indicate colocalized regions.

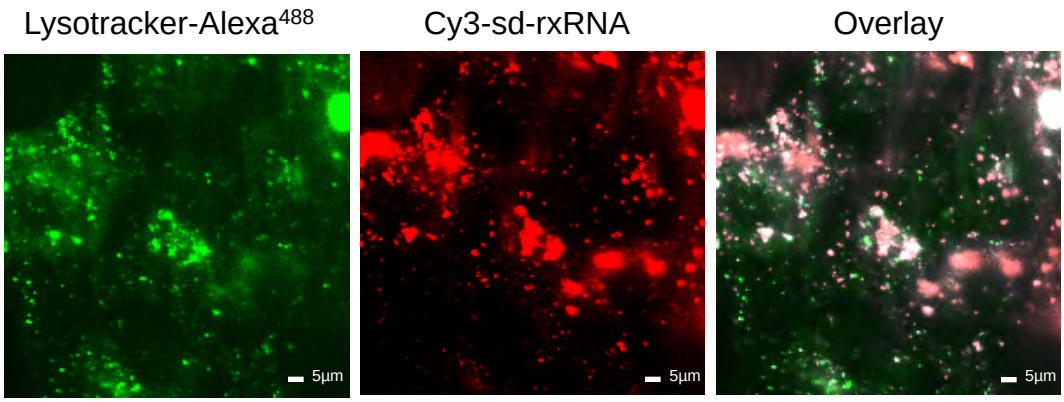

Figure 3.10. sd-rxRNA localizes to acidified vesicles. COS cells treated for 20 hours with sd-rxRNA were stained with lysotracker.

control and siRNA specific to EEA1. Once knockdown of EEA1 had reduced protein to virtually undetectable levels (Figure 3.11B) sd-rxRNA specific to MAP4K4 (M4K4) was added to these cells and the ability of M4K4-sd-rxRNA to silence M4K4 was assessed by quantitative real time PCR (qRT-PCR). As shown in Figure 3.11A under control conditions M4K4-sd-rxRNA is able to reduce M4K4 mRNA expression by 50% while in EEA1 knockdown cells attenuated this effect in a dose dependent manner. Knockdown of M4K4 by M4K4-sd-rxRNA was not inhibited in Rabenosyn-5 knockdown cells (Figure 3.11C) suggesting that EEA1 is specifically required for functional knockdown by sd-rxRNA. These results were confirmed with the use of a second sd-rxRNA targeting cyclophilin B (PPIB). As shown by immunoblotting in Figure 3.11D, siRNA depletion of EEA1 followed by treatment of these and control cells with PPIB-sd-rxRNA resulted in a marked decrease of PPIB protein levels in control transfected cells which was significantly inhibited in EEA1 knockdown cells.

To begin to determine the mechanism by which sd-rxRNA enters COS-7 cells we examined the ability of M4K4-sd-rxRNA to function in the absence of SidT1. Consistent with previous reports of low SidT1 expression in kidney [142], SidT1 is expressed at low levels COS-7 cells. Nonetheless, siRNA depletion of SidT1 followed by administration of M4K4-sd-rxRNA resulted in attenuated silencing at low concentrations of M4K4-sd-rxRNA (Figure 3.12).

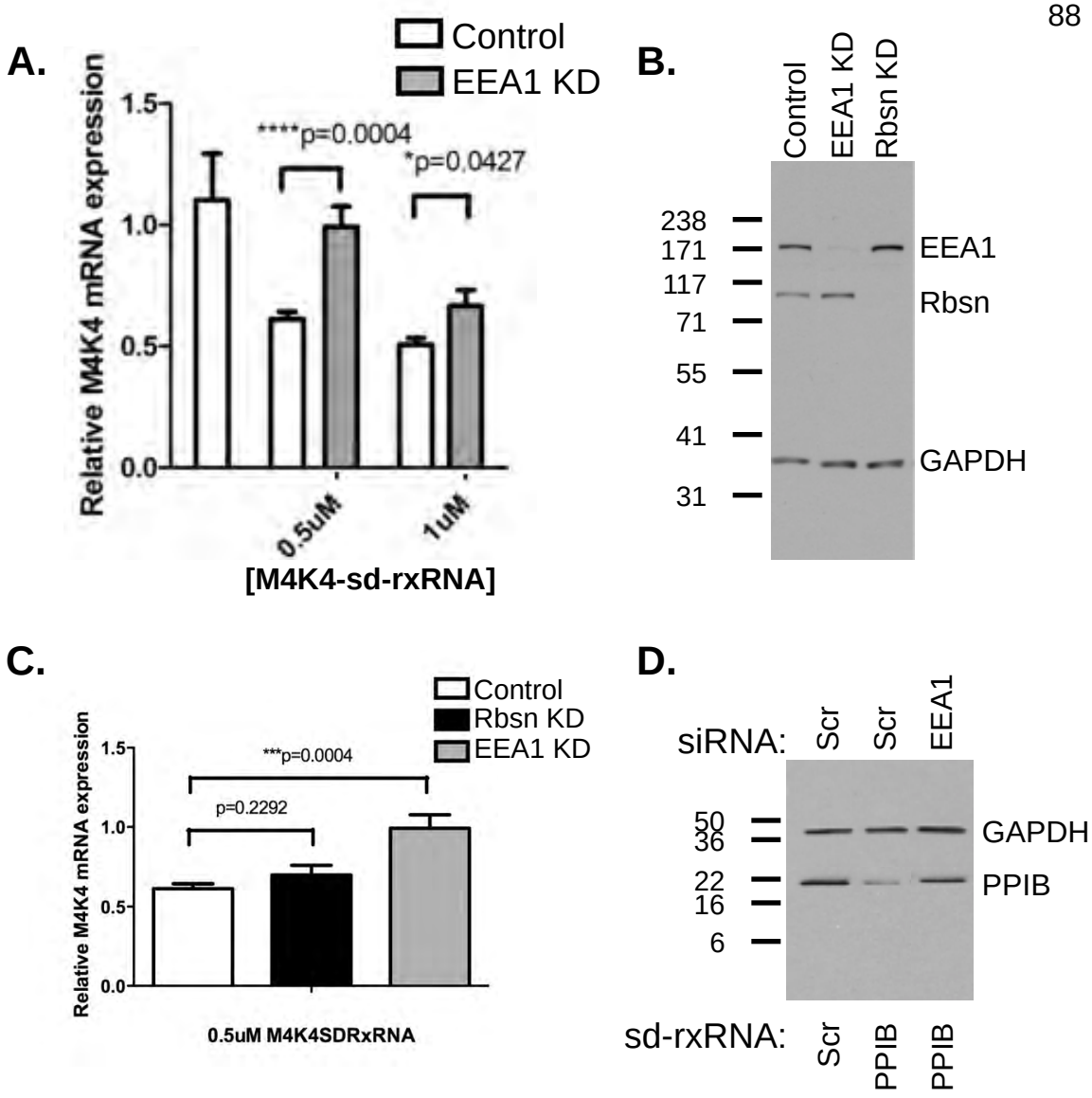

Figure 3.11. Loss of EEA1 impairs silencing by sd-rxRNA. COS-7 were treated with control, EEA1, or Rabenosyn-5 siRNA for 72 hours followed by 2 hour treatment with sd-rxRNA targeting MAP4K4 (M4K4). RNA was harvested 24 hours followed sd-rxRNA treatment and qRT-PCR was run to determine the relative expression of M4K4 mRNA. **A.** There is a dose dependent inhibition of M4K4-sd-rxRNA in EEA1 knockdown cells. **B.** Western blot showing the amount of EEA1 and Rabenosyn-5 protein remaining after their respective knockdowns. **C.** Knockdown of EEA1, but not Rabenosyn-5, inhibits silencing by M4K4-sd-rxRNA. **D.** COS-7 cells were treated with control (Scr), or EEA1 siRNA for 72 hours followed by 72 hour treatment with 2µM control sd-rxRNA or sd-rxRNA targeting cyclophilin B (PPIB). Lysates were harvested and immunoblots were probed for PPIB and GAPDH as a loading control.

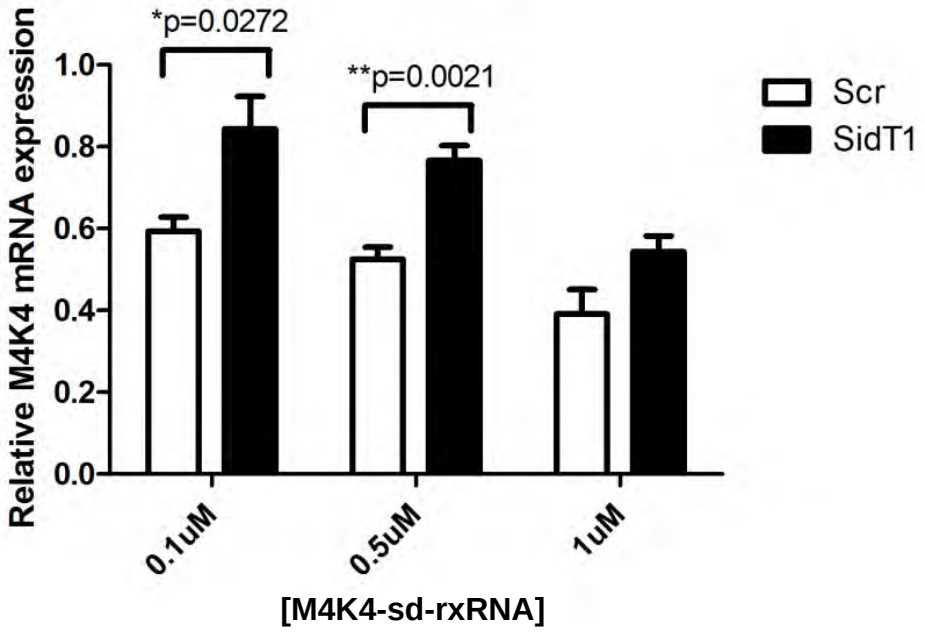

Figure 3.12. Loss of SidT1 impairs silencing by sd-rxRNA. COS-7 were treated with control (white) or SidT1 (black) siRNA for 72 hours followed by 2 hour treatment with sd-rxRNA targeting MAP4K4 (M4K4). RNA was harvested 24 hours followed sd-rxRNA treatment and qRT-PCR was run to determine the relative expression of M4K4 mRNA. There is a dose dependent inhibition of M4K4-sd-rxRNA in SidT1 knockdown cells.

DISCUSSION

Self-delivering siRNAs are of great therapeutic value because of their enhanced stability and efficient cellular uptake in the absence of a delivery vehicle. Understanding of the mechanisms by which these antisense oligonucleotides are taken up by target cells is of extreme importance. Recent work suggests scavenger receptors [138] or SID-1 transporter [139-142] are responsible for oligonucleotide uptake. Several components of the endocytic pathway are required for siRNA silencing suggesting endocytic vesicles are critical for siRNA entry into cells. To better understand the endosomal pathway by which oligonucleotides enter the cell we studied the uptake of a proprietary system of self-delivering siRNA. The results of the present study indicate endosomal localization of sd-rxRNA is distinct from fluid phase endocytosis suggesting a regulated mechanism of uptake.

TIRF microscopy demonstrates sd-rxRNA is taken up by COS-7 cells and transferred to Rabenosyn-5 and EEA1 positive endosomes, suggesting antisense oligonucleotides traffic through a specific endosomal pathway. Previously we've shown that Rabenosyn-5 is required for endocytic recycling of the TfR [154], however sd-rxRNA positive structures are distinct from Tf containing endosomes indicating that antisense oligonucleotides do not enter the endocytic recycling pathway. Sd-rxRNA colocalize with EGF containing endosomes, which require trafficking through EEA1 positive endosomes to be degraded in lysosomes and suggests antisense oligonucleotides follow a

lysosomal degradative pathway. Sd-rxRNA entry into both Rabenosyn-5 and EEA1 is consistent with the finding that endosomes containing both Rabenosyn-5 and EEA1 are found deeper within the cell [41]. Interestingly depletion of the PI(3)P endosomally localized protein Hrs [155] results in impaired EGFR degradation [156] and diminished miRNA silencing [101]. This is consistent with our findings that early sorting of sd-rxRNA to the lysosomal pathway is required for efficient silencing. Furthermore, EGF traffics through EEA1 positive endosomes and knockdown of EEA1 impairs EGFR degradation [49], similar reduction in EEA1 levels impairs targeted sd-rxRNA silencing suggesting sd-rxRNA and EGF follow the same degradative pathway.

SID-1 is a dsRNA channel required for systemic RNAi in *C. elegans* and to ask if a similar mechanism is present in mammals we investigated the function SidT1, the mammalian homolog of SID-1. Knockdown of SidT1 resulted in a reduction in silencing of the target of sd-rxRNA and suggests SidT1 may play a key role in sd-rxRNA uptake. Further studies are needed to address the role of SidT1, and possibly additional proteins, in sd-rxRNA internalization.

In addition to their implications in oligonucleotide uptake, scavenger receptors have been shown to be involved in the uptake of bacterial pathogens [157]. Additionally, RNA viruses such as Semliki Forest virus are known to use the endocytic pathway for viral pathogenesis [158]. Lastly, RNA silencing by siRNA has been show to protect both plants and invertebrates from viral infection [159]. Taken together these data suggest the antisense oligonucleotide uptake

pathway may have a role in the innate immune response and provide protection in the spread of viral infections.

Self-delivering siRNA represents a powerful potential therapeutic with seemingly limitless applications. Unfortunately little is known regarding how siRNA molecules enter the cell. A better understanding of the endocytic machinery governing sd-rxRNA entry could lead to more effective therapeutic siRNA delivery.

EXPERIMENTAL PROCEDURES

Cell culture and transfection – COS-7 cells were maintained in DMEM (Invitrogen) supplemented with 100U/ml penicillin streptomycin (Invitrogen), 0.1 mg/ml normocin (InvivoGen) and 10% fetal bovine serum (Atlanta Biologicals) at 37°C 5% CO_2. Cells were plated at a density of $1x10^5$ cells per well of a 6 well cell culture plate and grown for 24 hours. These cells were transfected with 1µg DNA using calcium phosphate and grown for 24 hours, plated on glass coverslips (Thomas Scientific 25 circle #1.5), grown for an additional 24 hours. Live imaging was done in KRH buffer (125M NaCl, 5mM KCl, 1.3mM $CaCl_2$, 1.2mM $MgSO_4$, 25mM HEPES, 2.5% BSA and 2mM sodium pyruvate) pH 7.4. Carrier free live imaging was done in KRH buffer without BSA (125M NaCl, 5mM KCl, 1.3mM $CaCl_2$, 1.2mM $MgSO_4$, 25mM HEPES and 2mM sodium pyruvate) pH 7.4.

RNAi – Rabenosyn-5 and EEA1 RNAi duplexes described previously [154], and

Sid1 (Sid no. 1 as described previously [142] along with non-targeting control duplexes were designed and synthesized by RXi Pharmaceuticals. One day before transfection cells were plated in antibiotic-free medium in a six-well cell-culture plate at a density of 1×10^5 cells per well. Cells were transfected using 5µL of Lipofectamine RNAiMAX (Invitrogen) according to the manufacturer's instructions with a final concentration of 10 nM siRNA. Cy3-conjugated scrambled and MAP4K4 sd-rxRNA and cyclophilin B sd-rxRNA were designed and synthesized by RXi Pharmaceuticals. Cells were treated with sd-rxRNA in DMEM.

Reagents – Polyclonal EEA1 and Rabenosyn-5 antibodies were described previously [154]. GAPDH antibody was obtained from Cell Signaling Technologies. Cyclophilin B antibody was obtained from Abcam. Unconjugated and DyLight-488–conjugated human Tf were obtained from Jackson Immunoresearch. EGF-Alexa-488, Lysotracker-488, and FM4-64 were obtained from Invitrogen.

Plasmids – GFP- Rabenosyn-5, GFP-EEA1, GFP-APPL1, and GFP-WDFY2 were previously described [65,126,127,154].

TIRF/Epi-fluorescence Structure-illumination Microscope (TESM) optical system, TESM imaging hardware and software, TESM 3-D imaging, and image analysis –

were described previously [154].

Quantitative RT-PCR – Total RNA was extracted using TRIzol reagent (Invitrogen). For quantitative mRNA analysis, 1µg of the total RNA was reverse-transcribed by using an iScript cDNA synthesis kit (Bio-Rad). 10% of each reverse transcriptase reaction was subjected to quantitative real-time PCR analysis using an iQ SYRB Green supermix kit and real-time PCR detection system following the manufacturer's instructions (MyiQ, Bio-Rad). β2-microglobulin was used as an internal housekeeping gene. Relative gene expression was calculated by the $2^{-\Delta\Delta CT}$ method [160].

CHAPTER IV

THE PLASMA MEMBRANE-ASSOCIATED GTPase RIN INTERACTS WITH THE DOPAMINE TRANSPORTER AND IS REQUIRED FOR PROTEIN KINASE C-REGULATED DOPAMINE TRANSPORTER TRAFFICKING

ABSTRACT

Dopaminergic signaling and plasticity are essential to numerous CNS functions and pathologies, including movement, cognition, and addiction. The amphetamine- and cocaine-sensitive dopamine (DA) transporter (DAT) tightly controls extracellular DA concentrations and half-life. DAT function and surface expression are not static but are dynamically modulated by membrane trafficking. We recently demonstrated that the DAT C terminus encodes a PKC-sensitive internalization signal that also suppresses basal DAT endocytosis. However, the cellular machinery governing regulated DAT trafficking is not well defined. In work presented here, we identified the Ras-like GTPase, Rin (for Ras-like in neurons) (Rit2), as a protein that interacts with the DAT C-terminal endocytic signal. Yeast two-hybrid, GST pull down and FRET studies establish that DAT and Rin directly interact, and colocalization studies reveal that DAT/Rin associations occur primarily in lipid raft microdomains. Coimmunoprecipitations demonstrate that PKC activation regulates Rin association with DAT. Perturbation of Rin function with GTPase mutants and shRNA-mediated Rin

knockdown reveals that Rin is critical for PKC-mediated DAT internalization and functional downregulation. These results establish that Rin is a DAT-interacting protein that is required for PKC-regulated DAT trafficking. Moreover, this work suggests that Rin participates in regulated endocytosis.

INTRODUCTION

Presynaptic neurotransmitter reuptake facilitated by plasma membrane transporters is the primary mechanism terminating synaptic transmission. Dopamine transporter (DAT) terminates DA signaling and thus is central to controlling extracellular DA levels in the brain [161]. DAT is the primary target for therapeutic agents such as methylphenidate (Ritalin) and bupropion (Wellbutrin), as well as the addictive psychostimulants amphetamine and cocaine, whose actions inhibit DAT function [162]. Recent knock-in transgenic mouse studies demonstrated that DAT availability is paramount to establishing the rewarding properties of cocaine [163], and aberrant DAT function was reported recently in a subgroup of attention-deficit hyperactivity disorder (ADHD) patients [164]. Moreover, $DAT^{+/-}$ and $DAT^{-/-}$ mice are hyperlocomotive and exhibit significant DA depletion in tissue stores [165,166]. Thus, mechanisms that regulate DAT plasma membrane availability are likely to have a significant impact on DA signaling and the availability of DAT to interact with therapeutic and addictive drugs.

A wealth of data demonstrates that DAT activity is acutely downregulated by protein kinase C (PKC) activation, resulting in DAT trafficking to, and sequestering in, endosomal vesicles [81,87]. Work from our laboratory established that DAT C-terminal residues 587–596 encode endocytic regulatory domain that modulates both basal and PKC-enhanced DAT internalization rates [90,91]. The DAT N terminus is also central to regulating DAT endocytic trafficking [167], and Nedd4–2-mediated ubiquitination in this domain is critical for PKC-mediated DAT sequestration [86,168]. A variety of proteins have been identified that interact with DAT, including PICK1 [169,170], Hic-5 [171], synaptogyrin-3 [172], and calcium/calmodulin-dependent kinase II (CaMKII) [94]. However, none of these identified DAT-interacting proteins are mechanistically linked to PKC-regulated DAT internalization. In the current study, we sought to identify proteins that (1) interacted with DAT endocytic regulatory residues 587–596 and (2) were required for PKC-regulated DAT trafficking. A yeast two-hybrid screen identified the Rin (for Ras-like in neurons) GTPase as a candidate DAT-interacting protein. Using biochemical, cellular imaging, and knockdown approaches, we determined that Rin interacts directly with DAT in a PKC-regulated manner and is required for PKC-mediated DAT internalization.

RESULTS

Rin is a DAT-interacting protein

We previously identified a 10 amino acid region encoded in hDAT C-terminal residues 587–596 that is required for PKC-regulated DAT internalization [91] and that negatively regulates basal DAT endocytic rates [90]. Our major aim in the current study was to identify proteins that interacted with the hDAT residues 587–596 (FREKALAYAIA) and that were mechanistically integral to PKC-regulated DAT trafficking. Using this sequence as bait, we used the hSOS rescue system to screen a human substantia nigra cDNA library. The advantage of this approach is that library cDNAs are myristylated and thereby anchored at the plasma membrane, whereas baits are cloned in-frame with the Ras guanine nucleotide exchange factor, hSOS. Thus, interactions between bait and library prey occur at or near the plasma membrane, mimicking circumstances during DAT endocytic trafficking. Screens take place in the temperature-sensitive mutant yeast strain cdc25H, which lacks Ras signaling and is unable to grow at the restrictive temperature. Protein–protein interactions localize hSOS to the plasma membrane, activate Ras signaling, and rescue the temperature-sensitive phenotype. In our initial studies, we attempted to use the entire DAT C terminus as bait. However, this bait alone was capable of rescuing growth in the absence of library coexpression and was thus deemed unsuitable as bait in the library screen. However, the FREKLAYAIA sequence (hDAT residues 587–596) alone did not rescue yeast growth (data not shown) and was therefore used as bait in

the screen. We isolated four clones that rescued yeast growth at the restrictive temperature. Sequence analysis revealed that clone H19 corresponded to the small neuronal GTPase Rin, also known as Rit2. Retransforming purified hRin plasmid with the DAT 587–596 bait also yielded a positive interaction and confirmed the protein–protein interaction (data not shown).

We first investigated whether Rin was expressed in dopaminergic cells, to determine whether there was a physiologically relevant context for cellular DAT/Rin interactions. Immunoblots revealed a single 25 kDa immunoreactive band in catecholaminergic cells lines and neuronal tissues, including the rat pheochromocytoma PC12, the human neuroblastoma SK-N-MC, as well as in rat striatum (Figure 4.1A). In addition to its neuronal expression, we also detected Rin in rat muscle and liver, primary cultured rat astrocytes, and mouse embryonic kidney cells, as well as in non-neuronal cell lines HeLa, COS-1, CHO, IMCD3, and HEK293 (Figure 4.1A). Given that the mRNA expression of Rin is reported to be restricted to neuronal tissue [173], we were concerned that the anti-Rin antibody might be also detecting Rit, the closest homolog of Rin. Because both proteins are 25 kDa and could not be distinguished on the basis of electrophoretic mobility, we used Rin and Rit GFP fusion proteins to test for this possibility. Both constructs were expressed in PC12 cells and exhibited the expected molecular weight shift, as confirmed by immunoblotting with anti-GFP antibodies (Figure 4.1D). However, the anti-Rin antibody only detected GFP–Rin and not GFP–Rit (data not shown), confirming its specificity. Thus, Rin protein

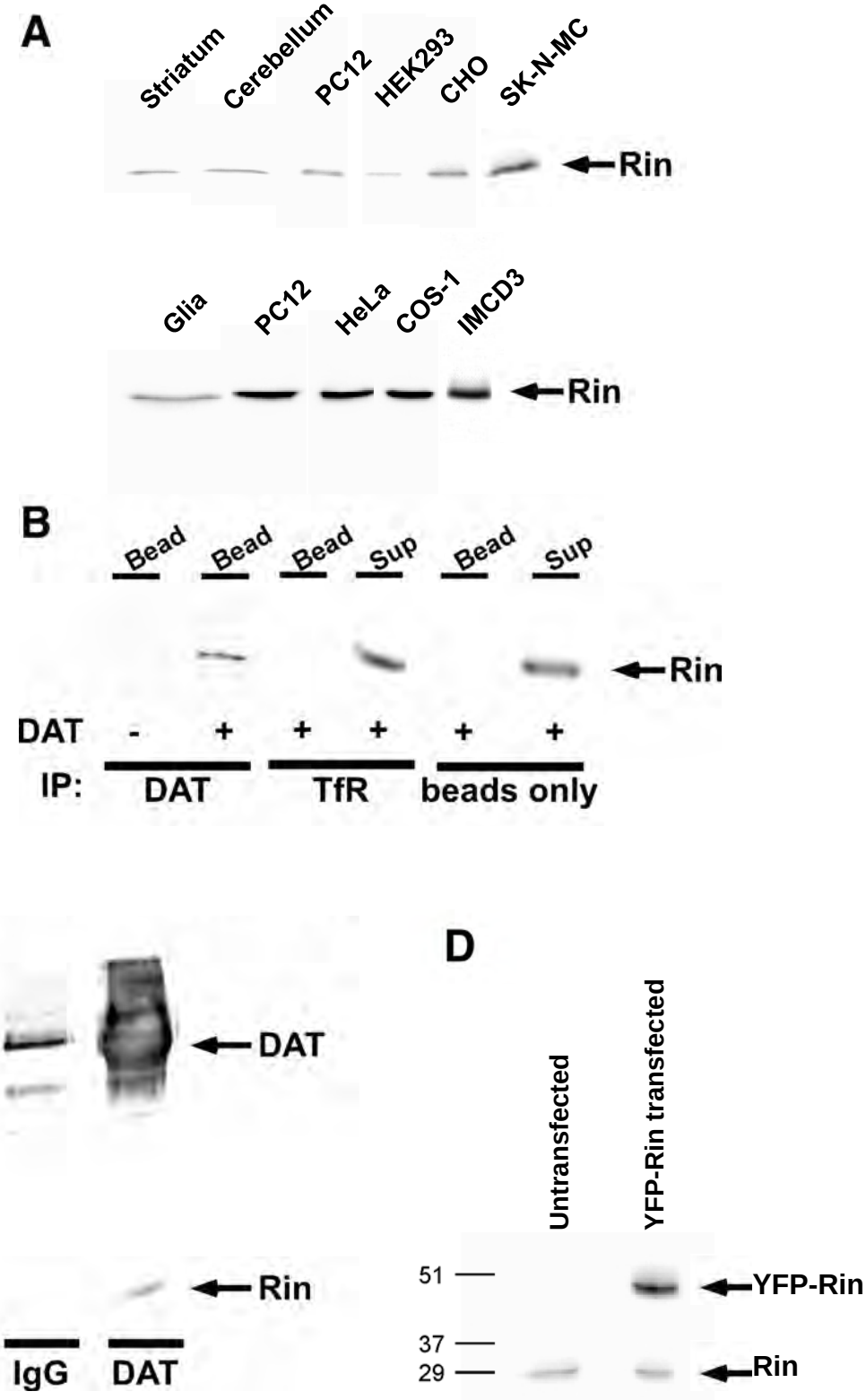
A
Striatum
Cerebellum
PC12
HEK293
CHO
SK-N-MC
Rin
Glia
PC12
HeLa
COS-1
IMCD3
Rin
B
Bead
Bead
Bead
Sup
Bead
Sup
Rin
DAT - + + + + +
IP: DAT TfR beads only
C
DAT
Rin
IP: IgG DAT
D
Untransfected
YFP-Rin transfected
51
37
29
YFP-Rin
Rin

Figure 4.1. Rin is expressed in PC12 cells and rat striatum and specifically coimmunoprecipitates with DAT. A. Rin expression in catecholaminergic tissue, noncatecholaminergic tissue, and cell lines. Top: Twenty micrograms of PC12, HEK293, CHO, and SK-N-MC lysate and 150 µg of rat striatal and cerebellum lysate. Bottom: 30µg of glial, PC12, HeLa, COS, and IMCD3 lysates were resolved by SDS-PAGE and immunoblotted with mouse anti-Rin antibodies. **B**. Coimmunoprecipitations. DAT was immunoprecipitated from equivalent amounts lysate from PC12 cells transfected with either vector (−) or DAT (+). Control immunoprecipitations were performed using anti-TfR antibodies or with Protein A/G beads alone. Bead eluents (Bead) and 110th supernatant volumes (Sup) were resolved by SDS-PAGE and immunoblotted with an anti-Rin antibody. Representative blots are shown (n = 3). **C**. Coimmunoprecipitations from rat striatal synaptosomes. Immunoprecipitations were performed with solubilized rat striatal synaptosomes using Protein A beads coated with rabbit anti-DAT antibodies or rabbit IgG alone. Eluents were resolved by SDS-PAGE, and immunoreactive bands were detected with the indicated antibodies. A representative blot is shown (n = 2). **D.** Immunoblot of PC12 cells and PC12 cells transfected with YFP-Rin.

appears to be expressed in neuronal, as well as non-neuronal, tissues and cell lines.

We next asked whether DAT and Rin interact in mammalian cells. Coimmunoprecipitations using an antibody directed against the DAT N terminus isolated Rin from DAT-PC12 cell lysates, confirming that Rin associates with DAT in mammalian neuroendocrine cells (Figure 4.1B). Rin coimmunoprecipitated with DAT specifically and was not isolated from nontransfected PC12 cells, with antibodies directed against the transferrin receptor, or when empty Protein A/G beads were used (Figure 4.1B). We also detected DAT/Rin interactions when DAT was immunoprecipitated from rat striatal synaptosomes (Figure 4.1C), confirming that the DAT/Rin interaction occurs in brain. It should be noted that we were unable to detect the DAT/Rin interaction when a C-terminus-directed anti-DAT antibody was used for immunoprecipitation, despite quantitative DAT pull down (data not shown). Moreover, we were not able to perform the reciprocal coimmunoprecipitation, because the available Rin antibody does not effectively immunoprecipitate Rin.

Although the Rin monoclonal antibody recognizes a single band on immunoblots, it does not recognize Rin *in situ*, nor does it immunoisolate Rin from cell lysates. Furthermore, our attempts to raise rabbit anti-peptide antibodies against Rin domains divergent from its homolog Rit did not yield immunoreactive sera. Therefore, we used CFP-tagged Rin to ask whether DAT and Rin colocalize in cells and, if so, in what cellular regions. In PC12 cells

cotransfected with CFP–Rin and DAT, staining was clearly detected as a ring around the cell perimeter (Figure 4.2A), consistent with its predicted plasma membrane localization. CFP–Rin was also detected primarily at the cell perimeter (Figure 4.2A), consistent with reports that it localizes to the plasma membrane [174]. We observed substantial DAT and Rin colocalization at the plasma membrane, and DAT and Rin colocalization was limited to discrete foci within the plasma membrane (Figure 4.2A, arrowheads). We also observed areas in which DAT did not appear to colocalize with Rin (Figure 4.2A, arrows). DAT is distributed between lipid raft and non-raft microdomains within the plasma membrane [175-177], and we asked whether the focal distribution of DAT/Rin colocalization correlated with the expression of DAT in membrane microdomains. To answer this question, we coexpressed DAT and CFP–Rin and labeled lipid rafts with Alexa Fluor 594-conjugated CTX, which specifically labels membrane rafts via binding to GM1 ganglioside [178]. Cells were then fixed, and DAT and CFP–Rin were stained as described in Experimental Procedures, using Alexa Fluor 488- and Alexa Fluor 405-conjugated secondary antibodies to visualize DAT and Rin in the green and blue channels, respectively (Figure 4.2B, C). Visually we observed striking colocalization of DAT and Rin in CTX-positive regions (Figure 4.2C, arrowheads). We then quantitatively compared the percentage of DAT/Rin colocalization in CTX-positive versus CTX-negative regions. At virtually all the thresholds tested, there was more DAT/Rin colocalization in rafts than in non-rafts (n = 16). Only at a very few extreme

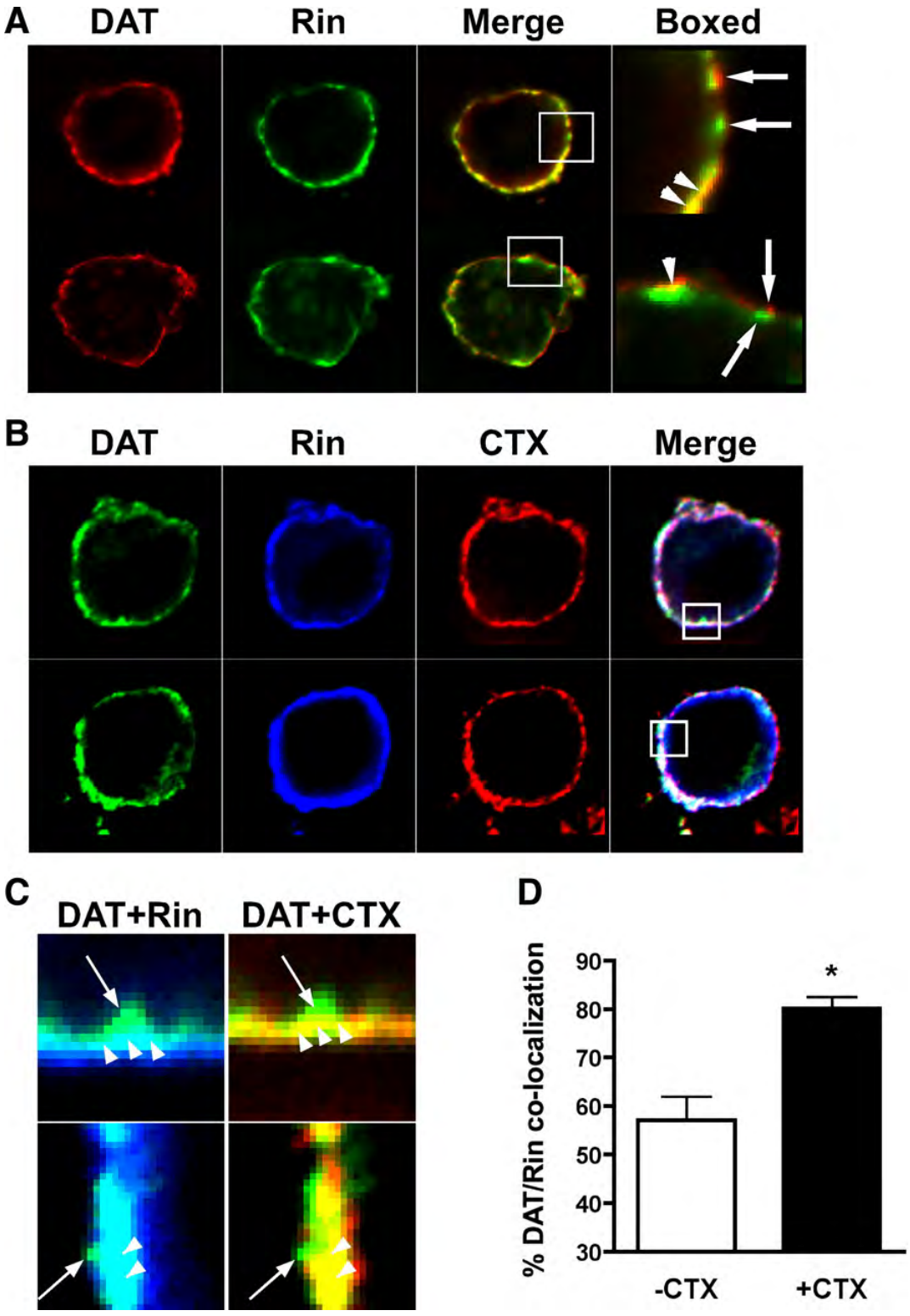
A
DAT
Rin
Merge
Boxed
B
DAT
Rin
CTX
Merge
C
DAT+Rin
DAT+CTX
D
% DAT/Rin co-localization
90
80
70
60
50
40
30
*
-CTX
+CTX

Figure 4.2. DAT and Rin colocalization at the plasma membrane is enriched in lipid raft microdomains. Immunofluorescence. PC12 cells were cotransfected with DAT and CFP–Rin and were fixed and stained as follows. **A**. Cells were stained with anti-DAT and anti-GFP antibodies and imaged as described in Materials and Methods. Boxes indicate an enlargement of the areas indicated with white boxes in the merged images. **B**. Cells were labeled with Alexa Fluor 594–CTX and were subsequently stained with anti-DAT and anti-GFP antibodies and imaged as described in Materials and Methods. **C**. Enlargement of the boxed areas from images in B. Arrows indicate DAT-immunoreactive pixels that colocalize with neither Rin (blue) nor CTX (red). Arrowheads indicate foci of DAT/Rin colocalization that also colocalize with CTX. **D**. Average data. DAT/Rin colocalization in CTX-positive (+CTX) and CTX-negative (−CTX) cell regions was measured at 10 independent thresholds per channel, as described in Materials and Methods. Average data at the median threshold are expressed as percentage ± SEM DAT/Rin colocalization. *$p < 0.0001$, significantly different from −CTX, paired t test; $n = 16$.

thresholds for a few cells (data not shown) was DAT/Rin colocalization higher (by a small amount) in CTX-negative regions than in CTX-positive regions. Analysis at the median threshold values for each cell revealed significantly more DAT/Rin colocalization in raft versus non-raft populations (80.1 ± 2.4% in CTX-positive vs 57.0 ± 4.9% in CTX-negative regions; $p < 0.0001$, paired *t*-test; $n = 16$).

To further evaluate whether DAT and Rin directly interact in living cells, we used FRET microscopy [178] using the three-filter method [179] as described by Feige *et al*. [180], which achieves quantitative visualization of protein oligomerization in intact cells and which generates N_{FRET} images. The results are shown in Figure 4.3 and Table 4.1. To provide a reference for membrane protein oligomerization, we coexpressed CFP- and YFP-tagged DAT, which have been shown to homo-oligomerize by both biochemical approaches [181-184] and FRET microscopy in various cell lines [181,183,184] and transfected neurons [172]. In addition, we used SERT tagged with CFP and YFP on its cytoplasmic N and C termini, respectively (C-SERT-Y), i.e., a transporter construct predicted to produce a strong homotypic FRET signal [172]. Coexpressing C-DAT and Y-DAT or C-SERT-Y resulted in enriched plasma membrane fluorescence and, as expected, robust N_{FRET} signals (18.89 ± 0. 1.16, $n = 23$ and 48.39 ± 2.54, $n = 28$, respectively; Figure 4.3B, Table 4.1). Similarly, expressing fluorescently tagged Rin proteins resulted in predominant plasma membrane fluorescence (Figure 4.3A). Coexpression of CFP–DAT and YFP–Rin resulted in an N_{FRET} value of 17.54 ± 1.30 ($n = 24$; Figure 4.3A, B), which was significantly higher than

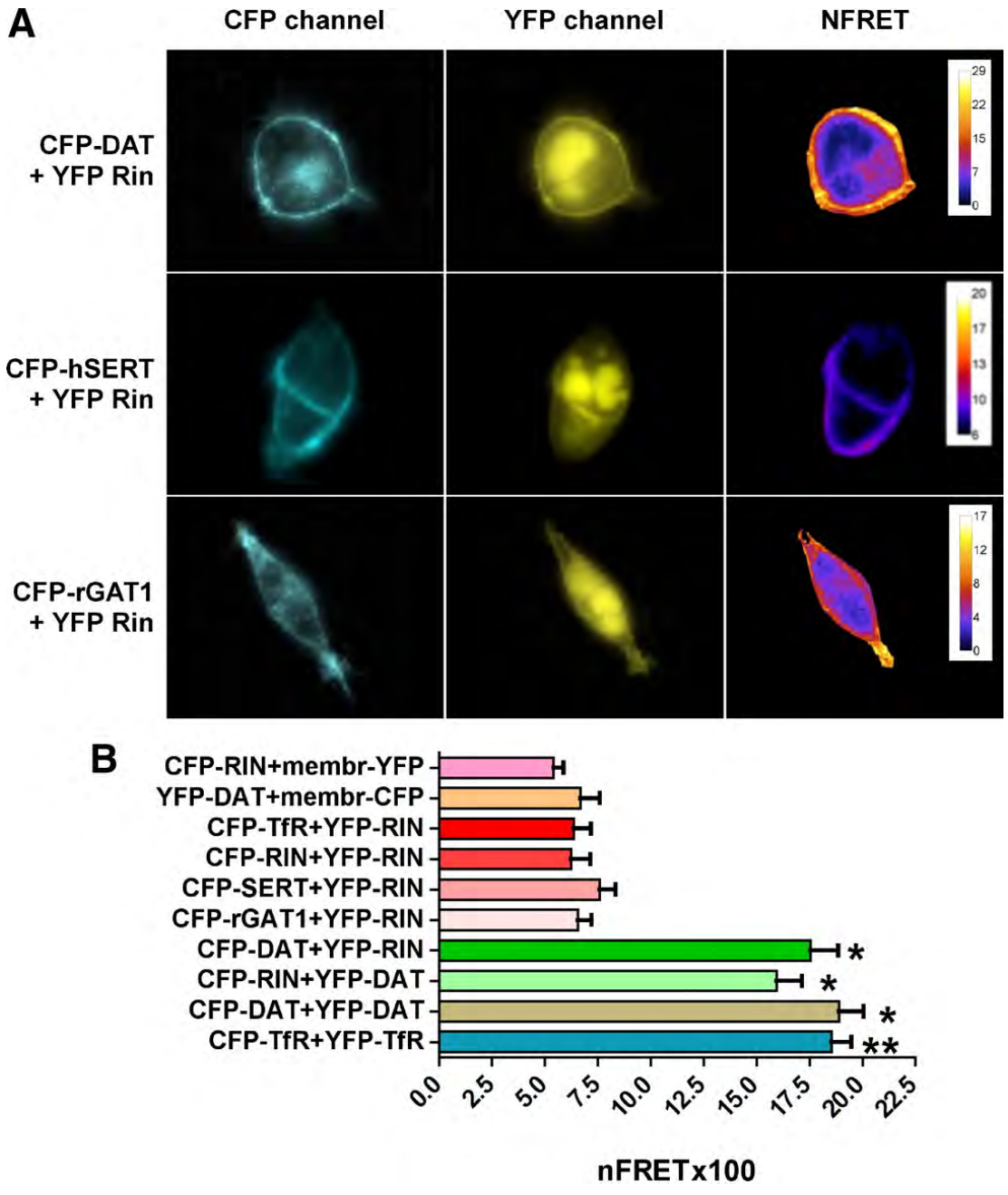
A
CFP channel
YFP channel
NFRET
CFP-DAT
+ YFP Rin
CFP-hSERT
+ YFP Rin
CFP-rGAT1
+ YFP Rin
29
22
15
7
0
20
17
13
10
6
17
12
8
4
0
B
CFP-RIN+membr-YFP
YFP-DAT+membr-CFP
CFP-TfR+YFP-RIN
CFP-RIN+YFP-RIN
CFP-SERT+YFP-RIN
CFP-rGAT1+YFP-RIN
CFP-DAT+YFP-RIN
CFP-RIN+YFP-DAT
CFP-DAT+YFP-DAT
CFP-TfR+YFP-TfR
*
*
*
**
0.0
2.5
5.0
7.5
10.0
12.5
15.0
17.5
20.0
22.5
nFRETx100

Figure 4.3. Rin and DAT oligomerization as demonstrated by FRET microscopy in intact cells. HEK293 cells were transiently transfected with cDNAs encoding CFP- or YFP-tagged proteins as indicated, and epifluorescence microscopy was performed 2 d after transfection. **A**. The first and second columns show images obtained with CFP and YFP filter sets, respectively; the third column displays a corrected and normalized FRET image (NFRET) established with PIXFRET. A look-up table of the color code used is presented in the last column. All images shown are representative of three to seven experiments. In all images, background fluorescence was subtracted. **B**. Averaged data. Normalized FRET efficiencies (NFRET values) are given for cells expressing the following constructs: C-Rin and membrane-bound YFP (membr-YFP; n = 15), Y-DAT and membr-CFP (n = 25), C-TfR and Y-Rin (n = 20), C-Rin and Y-Rin (n = 16), C-SERT and Y-Rin (n = 27), C-rGAT1 and Y-Rin (n = 30), C-DAT and Y-Rin (n = 24), C-Rin and Y-DAT (n = 20), C-DAT and Y-DAT (n = 23), and C-TfR and Y-TfR (n = 37). All values were analyzed by one-way ANOVA with Dunn's multiple comparison test. *$p < 0.001$, significantly different from (YFP–DAT and membr-CFP), (CFP–Rin and YFP–Rin), and (Rin and membr-YFP). **$p < 0.001$, significantly different from (CFP–TfR and YFP–Rin), (CFP–Rin and YFP–Rin), and (Rin and membr-YFP). See Table 1 for statistical analysis of complete dataset.

Table 4.1. Statistical analysis of N_{FRET} values

FRET Pair #1	FRET Pair #2	Significant?
CFP–DAT + YFP–Rin	CFP–SERT + YFP–Rin	Yes*
CFP–DAT + YFP–Rin	CFP–rGAT1 + YFP–Rin	Yes*
CFP–DAT + YFP–Rin	CFP–TfR + YFP–TfR	NS
CFP–DAT + YFP–Rin	CFP–TfR + YFP–Rin	Yes*
CFP–DAT + YFP–Rin	CFP–Rin + YFP–Rin	Yes*
CFP–DAT + YFP–Rin	YFP–DAT + membr-CFP	Yes*
CFP–DAT + YFP–Rin	CFP–Rin + membr-YFP	Yes*
CFP–DAT + YFP–Rin	CFP–Rin + YFP–DAT	NS
CFP–DAT + YFP–Rin	CFP–DAT + YFP–DAT	NS
CFP–SERT + YFP–Rin	CFP–rGAT1 + YFP–Rin	NS
CFP–SERT + YFP–Rin	CFP–TfR + YFP–TfR	Yes*
CFP–SERT + YFP–Rin	CFP–TfR + YFP–Rin	NS
CFP–SERT + YFP–Rin	CFP–Rin + YFP–Rin	NS
CFP–SERT + YFP–Rin	YFP–DAT + membr-CFP	NS
CFP–SERT + YFP–Rin	CFP–Rin + membr-YFP	NS
CFP–SERT + YFP–Rin	CFP–Rin + YFP–DAT	Yes**
CFP–SERT + YFP–Rin	CFP–DAT + YFP–DAT	Yes*
CFP-rGAT1 + YFP–Rin	CFP–TfR + YFP–TfR	Yes*
CFP-rGAT1 + YFP–Rin	CFP–TfR + YFP–Rin	NS
CFP-rGAT1 + YFP–Rin	CFP–Rin + YFP–Rin	NS

*$p < 0.001$, **$p < 0.05$, one-way ANOVA with Dunn's multiple comparison test.

fluorescent Rin proteins ($p < 0.001$, one-way ANOVA with Dunn's multiple comparison test) and not significantly different from either coexpressed CFP–DAT and YFP–DAT or CFP–Rin and YFP–DAT. This confirms that DAT and Rin interact in living cells and that the different fluorescent tags do not influence the signal. To control for the possibility of nonspecific FRET of fluorescent proteins in the plasma membrane, we tested whether Rin would generate significant FRET interaction with membrane anchored YFP; coexpression with CFP–Rin yielded an N_{FRET} value of 5.40 ± 0.49 ($n = 15$; Figure 4.3B), which was significantly less than any DAT/Rin combination ($p < 0.001$). Apparently, this membrane-attached YFP can serve as a weak acceptor for CFP fluorophores attached to proteins integral to membranes; indeed, some spurious FRET signal was visible during coexpression with CFP–DAT, but only in a cytosolic compartment (data not shown); therefore, the transitional interaction most likely occurred in the endoplasmic reticulum. Importantly, Rin proteins do not interact with themselves as revealed by an N_{FRET} value of 6.24 ± 0.90 ($n = 16$; Figure 4.3B).

We next asked whether the interaction of Rin with DAT was specific to DAT or whether it extended either to other SLC6 transporters or generally to proteins that are rapidly endocytosis, such as the transferrin receptor (TfR). To test potential Rin interaction with other SLC6 neurotransmitter transporters, we coexpressed Rin with either fluorescently tagged rat GABA (CFP–GAT1) or human serotonin transporter (CFP–SERT). Interestingly, CFP–GAT1 and CFP–

SERT did not interact with YFP–Rin (N_{FRET} values of 6.55 ± 0.64 and 7.58 ± 0.77, respectively; Figure 4.3A, B). Neither condition differed significantly from the CFP–Rin and membrane YFP negative control, and rGAT1 and Rin were significantly less than from DAT and Rin ($p < 0.001$) and from the positive control CFP–TfR and YFP–TfR (N_{FRET} value of 18.53 ± 0.96) ($p< 0.001$) but not from hSERT and Rin (N_{FRET} value of 7.58 ± 0.77; $n = 27$), respectively (Figure 4.3B). To test for Rin interactions with rapidly internalizing surface proteins, we coexpressed of YFP–Rin with CFP–TfR. This condition resulted in an N_{FRET} value of 6.35 ± 0.83, which was significantly less that DAT/Rin FRET pairs and not significantly greater than fluorescent Rin proteins or membrane-anchored fluorescent proteins with either DAT or Rin (Figure 4.3B). Lack of a significant TfR/Rin FRET signal was not attributable to inability of fluorescently tagged TfR to form FRET pairs, because CFP–TfR and YFP–TfR coexpression resulted in an N_{FRET} value of 18.5 ± 0.96, which was significantly greater than fluorescent TfR with Rin and is consistent with the known TfR homodimerization (Figure 4.3B) [185].

We next tested whether DAT/Rin interactions relied specifically on the DAT C terminus. To test this, we performed *in vitro* pull-down assays, using a GST fusion protein expressing DAT C-terminal residues 587–617 to probe PC12 cell homogenates lacking DAT expression. The GST–DAT 587–617 fusion protein was sufficient to isolate Rin from PC12 homogenates, whereas GST alone was not (Figure 4.4A). Moreover, GST–DAT 587–617 recovered Rin from

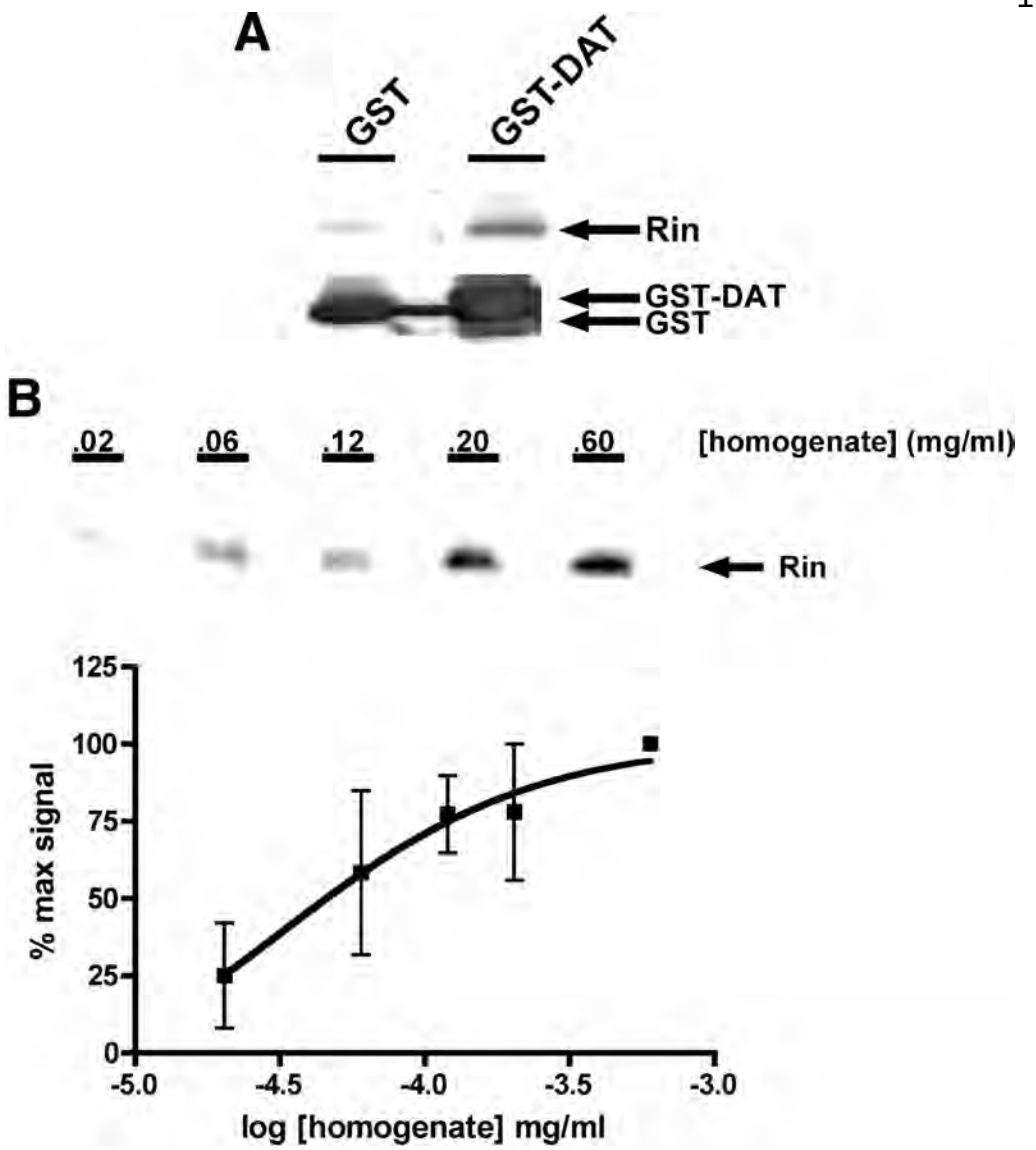

Figure 4.4. Rin interacts with DAT C terminus. GST pull-down assays. PC12 homogenate was incubated with either GST or GST–DAT 587–617, 1 h, 37°C. Complexes were isolated with glutathione agarose, and Rin was detected by immunoblot as described in Materials and Methods. **A**. Rin is isolated with the DAT C terminus but not GST alone. **B**. Concentration dependence. GST–DAT 587–617 was incubated with increasing concentrations of PC12 homogenate, 1 h, 37°C, followed by isolation of complexes with glutathione agarose. Top, Representative immunoblot probed for Rin. Bottom, Averaged data. Results are expressed as percentage maximal Rin signal versus log PC12 homogenate concentration (milligrams per milliliters) and were fit to a sigmoidal dose–response curve ($r^2 = 0.98$, $n = 3$).

PC12 homogenates in a concentration-dependent manner (Figure 4.4B). Together with our yeast two-hybrid co-IP and FRET data, these results demonstrate that DAT and Rin directly interact in mammalian cells and brain and that their interaction is mediated by the DAT C terminus, which encodes the FREKLAYAIA sequence used as bait in the original yeast two-hybrid screen.

PKC activation regulates DAT and Rin interactions

Our previous studies demonstrated that DAT residues 587–596 (FREKLAYAIA) encode elements that control DAT endocytic rates in a PKC-sensitive manner [90]. Specifically, 587–589 (REK) residues are required for PKC-induced increases in DAT internalization. Moreover, mutating residues 587–590 accelerates basal DAT endocytic rates, suggesting that a negative regulatory mechanism controls DAT endocytic rates. Therefore, we asked whether DAT associations with Rin were regulated by PKC activation and whether residues in the 587–590 region played a role in DAT/Rin interactions. PC12 cells stably expressing either wild-type DAT or the DAT 587–590(4A) mutant were treated with 1 μM PMA, 30 min, 37°C, and DAT/Rin interactions were assessed by coimmunoprecipitation and immunoblot. PKC activation significantly increased wild-type DAT/Rin interactions to 183.6 ± 16.5% of basal DAT/Rin interactions ($p < 0.005$, Student's t test; $n = 4$) (Figure 4.5A). PMA-induced increases in wild-type DAT/Rin interactions were blocked when cells were preincubated with the PKC inhibitor BIM (Figure 4.5A), demonstrating that

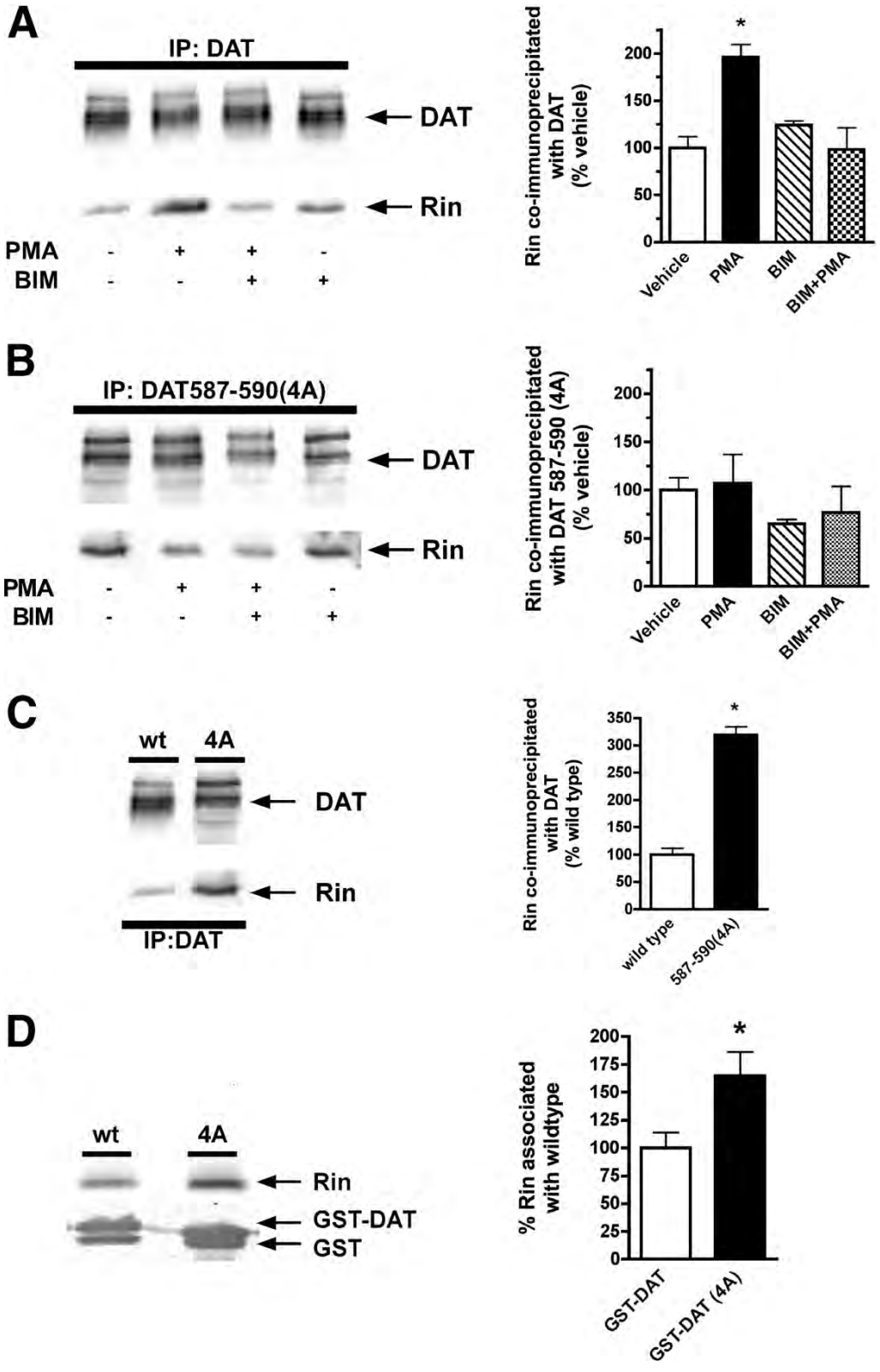
A
IP: DAT
DAT
Rin
PMA - + + -
BIM - - + +
Rin co-immunoprecipitated with DAT (% vehicle)
200
150
100
50
0
*
Vehicle
PMA
BIM
BIM+PMA
B
IP: DAT587-590(4A)
DAT
Rin
PMA - + + -
BIM - - + +
Rin co-immunoprecipitated with DAT 587-590 (4A) (% vehicle)
200
150
100
50
0
Vehicle
PMA
BIM
BIM+PMA
C
wt
4A
DAT
Rin
IP:DAT
Rin co-immunoprecipitated with DAT (% wild type)
350
300
250
200
150
100
50
0
*
wild type
587-590(4A)
D
wt
4A
Rin
GST-DAT
GST
% Rin associated with wildtype
200
175
150
125
100
75
50
25
0
*
GST-DAT
GST-DAT (4A)

Figure 4.5. DAT/Rin interactions are regulated by PKC activation and are sensitive to DAT C-terminal residues 587-590. A–C. Coimmunoprecipitations. PC12 cells stably expressing either wild-type DAT (**A**) or DAT 587–590(4A) (**B**) were pretreated with either 1 μM BIM or vehicle, 20 min, 37°C, followed by treatment with either vehicle or 1 μM PMA, 30 min, 37°C. Cells were lysed, and DAT was immunoprecipitated from equivalent amounts of cellular protein. Immunoprecipitants were resolved by SDS-PAGE and immunoblotted for both DAT and Rin. Left, Representative immunoblots. Right, Averaged data. Rin signals from nonsaturating bands were normalized to DAT signals and are expressed as percentage vehicle signal ± SEM. *$p < 0.002$, significantly different from vehicle control (one-way ANOVA with Tukey's multiple comparison test; $n = 4$). **C**. Basal Rin interaction with wild-type versus 587–590(4A) DAT. Left, Representative immunoblot. Right, Averaged data. Rin signals from nonsaturating bands were normalized to DAT signals and expressed as percentage wild-type signal ± SEM. *$p < 0.0005$, significantly different from wild-type DAT (Student's t test; $n = 3$). **D**. GST pull downs. GST fused to either wild-type or DAT 587–590(4A) C termini were induced and isolated on glutathione sepharose as described in Materials and Methods. Equivalent amounts of GST–DAT fusion proteins were incubated with PC12 homogenates, and bound proteins were resolved by SDS-PAGE and immunoblotted for both Rin and GST. Left, Representative immunoblot. Right, Averaged data. Rin densities were normalized to total GST pulled down for each sample and are expressed as percentage ± SEM Rin isolated compared with wild-type GST–DAT. *$p < 0.04$, significantly different from wild-type GST–DAT (Student's t test; $n = 5$).

the PMA-induced increase in DAT/Rin interactions is PKC dependent. In contrast, PMA treatment did not significantly increase Rin interactions with DAT 587–590(4A) (Figure 4.5B), and pretreatment with BIM did not alter DAT 587–590(4A)/Rin interactions. Moreover, under basal conditions, DAT 587–590(4A) interactions with Rin were 300% of wild-type DAT/Rin interactions (Figure 4.5C). These results suggest that DAT residues 587–590 are required for PKC-induced increases in DAT/Rin interactions. Additionally, these results suggest that DAT/Rin interactions increase in conditions were DAT internalization rates are accelerated either by PKC activation or mutating residues 587–590. To further test this possibility, we performed GST pull downs using GST–DAT C terminus that encoded the 587–590(4A) mutation [GST–DAT(4A)]. GST–DAT(4A) isolated significantly more Rin than wild-type GST–DAT (164.6 ± 21.8% of wild-type levels) (Figure 4.5D), consistent with a role for residues 587–590 in modulating DAT/Rin interactions.

Rin is required for PKC-mediated DAT trafficking

We next asked whether DAT endocytosis requires Rin activity, under either basal or PKC-stimulated conditions. To address this question, we used reversible biotinylation to measure relative DAT internalization rates in PC12 cells coexpressing DAT with wild-type Rin, or constitutively active (Q78L) or dominant-negative (S34N) Rin mutants. The results are shown in Figure 4.6. DAT internalized robustly under control conditions and PMA treatment

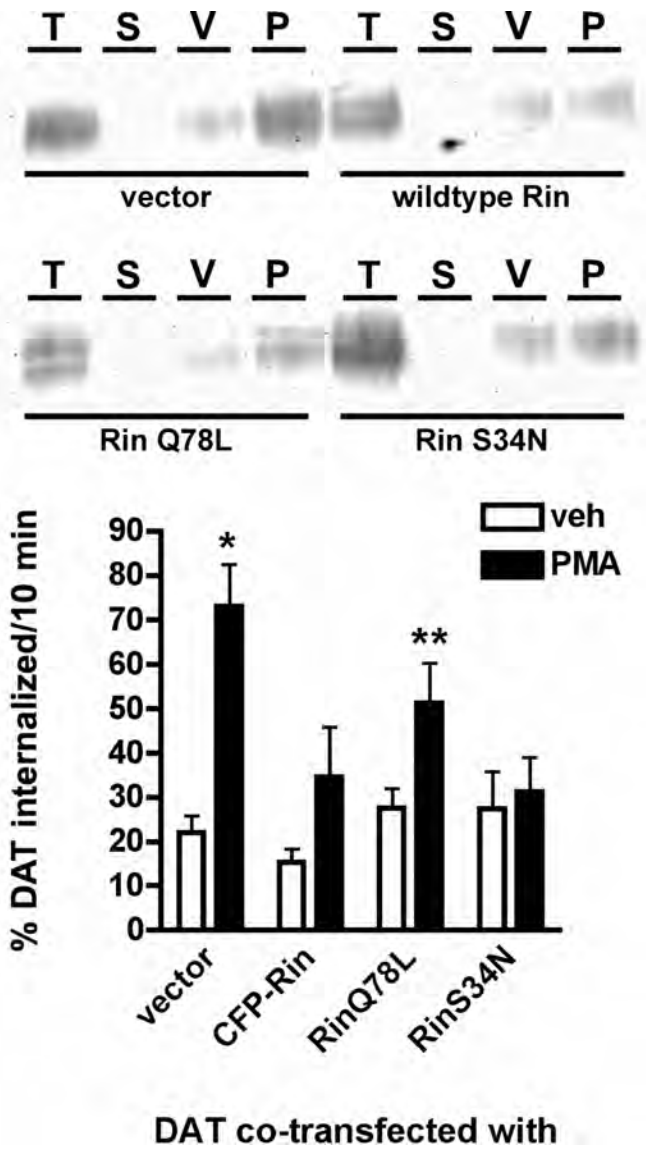

Figure 4.6. PKC-induced DAT internalization requires Rin activity. Internalization assays. PC12 cells were cotransfected with DAT and the indicated Rin or control cDNAs and were assayed 48–72 h after transfection. Relative DAT internalization rates over 10 min were measured by reversible biotinylation during treatment with or without 1 μM PMA, 37°C as described in Materials and Methods. Top, Representative immunoblots showing total surface DAT at time 0 (T), strip controls (S), and internalized DAT under vehicle-treated (V) and PMA-treated (P) conditions. Bottom, Average data. veh, Vehicle. Data are expressed as percentage ± SEM DAT internalized/10 min compared with total surface DAT at t = 0. *p < 0.001, **p < 0.05, significantly different from vehicle-treated control (Student's t test; n = 4).

significantly increased the endocytic rate of DAT, both when DAT was coexpressed with empty vector or constitutively active RinQ78L. In contrast, coexpressing DAT with either wild-type Rin or dominant-negative Rin S34N completely inhibited PMA-stimulated DAT endocytosis but had no effect on basal DAT internalization rates. These results demonstrate that Rin activity is required for PKC stimulation of DAT endocytosis.

We also visually examined DAT surface levels in response to PKC activation when DAT was coexpressed with either wild-type or mutant Rin constructs. When DAT was coexpressed with either vector (data not shown) or CFP–Rin, we observed robust DAT and Rin surface expression under vehicle-treated conditions (Figure 4.7). PMA treatment for 30 min, 37°C resulted in marked DAT redistribution to intracellular puncta, whereas Rin dissociated from DAT remained at the plasma membrane after PKC activation (Fugure 4.7). In cells that coexpressed DAT and Rin mutants, DAT and Rin were similarly expressed at the plasma membrane under vehicle conditions (Figure 4.7). However, although both wild-type Rin and Rin S34N inhibited PKC-stimulated DAT internalization when the global population was examined by biochemical means (i.e., reversible biotinylation; Figure 4.6), we still observed a subpopulation of cells that exhibit DAT intracellular sequestration in response to PKC activation. In this subpopulation, and in contrast to control conditions, both RinQ78L and S34N failed to dissociate from DAT and internalized with DAT into intracellular puncta after PKC activation (Figure 4.7). The majority of intracellular

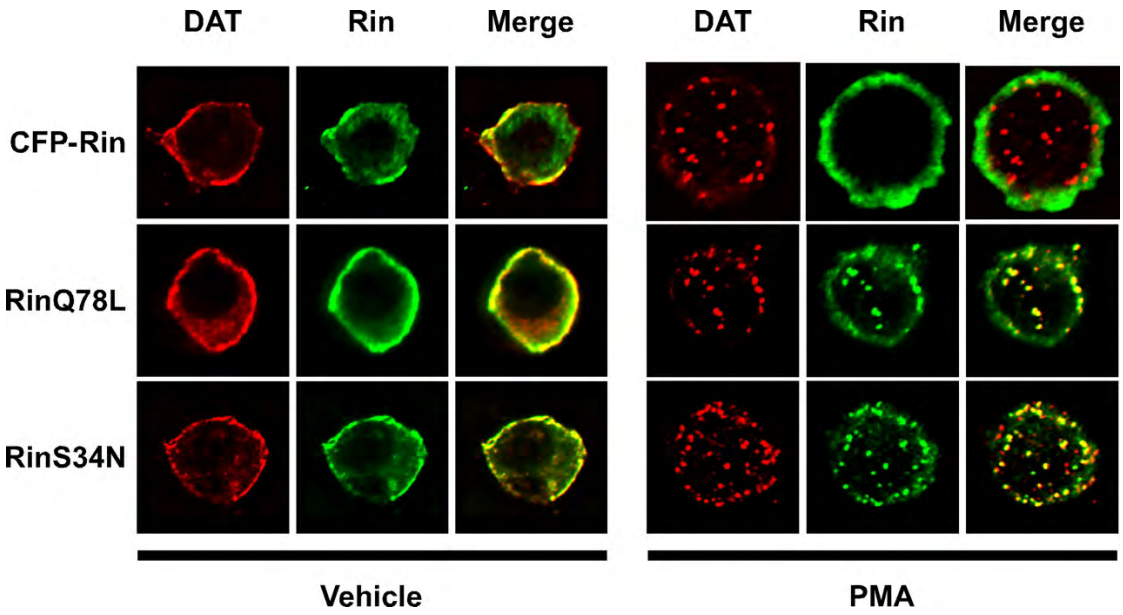

Figure 4.7. Guanyl nucleotide exchange is required for PKC-mediated Rin dissociation from DAT. Immunofluorescence. PC12 cells were cotransfected with DAT and the indicated Rin or control cDNAs and were assayed 48 h after transfection. Cells were treated with or without 1 μM PMA, 30 min, 37°C and were fixed, stained with anti-DAT or anti-GFP (to detect CFP–Rin) antibodies, and imaged as described in Materials and Methods. Planes through the cell center are shown and are representative of 12–16 cells imaged per condition in instances in which PMA-induced internalization was apparent (n = 4).

Rin puncta colocalized with DAT, although some DAT puncta were without Rin colocalization. These results suggest that the ability of Rin to dissociate from DAT after PKC activation is dependent on its ability to exchange guanyl nucleotide.

We further tested whether Rin was required for PKC-mediated DAT trafficking, using shRNAs targeted against human Rin mRNA to knockdown cellular Rin levels. Three shRNAs were tested for their ability to reduce cellular Rin levels in HEK293 cells. Of these, hRin228 significantly reduced Rin levels down to 68.6 ± 12.6% of that observed in vector-transfected cells, whereas a scrambled shRNA had no effect on Rin levels (Figure 4.8B, inset). Using these Rin-directed shRNAs, we first asked whether Rin was required for PKC-induced DAT sequestration in the human neuroblastoma cell line SK-N-MC. This line was chosen because it expresses the dopamine biosynthetic enzyme tyrosine hydroxylase and is compatible with commercially available human-targeted shRNAs. We coexpressed DAT encoding an extracellular HA epitope tag in the second extracellular loop with control or Rin-directed shRNA vectors and assessed PMA-induced DAT endocytosis by labeling surface DAT with anti-HA antibody. In cells cotransfected with DAT and GFP-expressing vector, treatment with 1 μM PMA treatment, 15 min, 37°C resulted in robust DAT intracellular puncta in 79.8 ± 2.9% of cells (Figure 4.8). Coexpressing DAT with scrambled shRNA had no significant effect on the number of cells exhibiting PMA-induced DAT internalization (73.0 ± 11.0% of cells). In contrast, significantly fewer cells

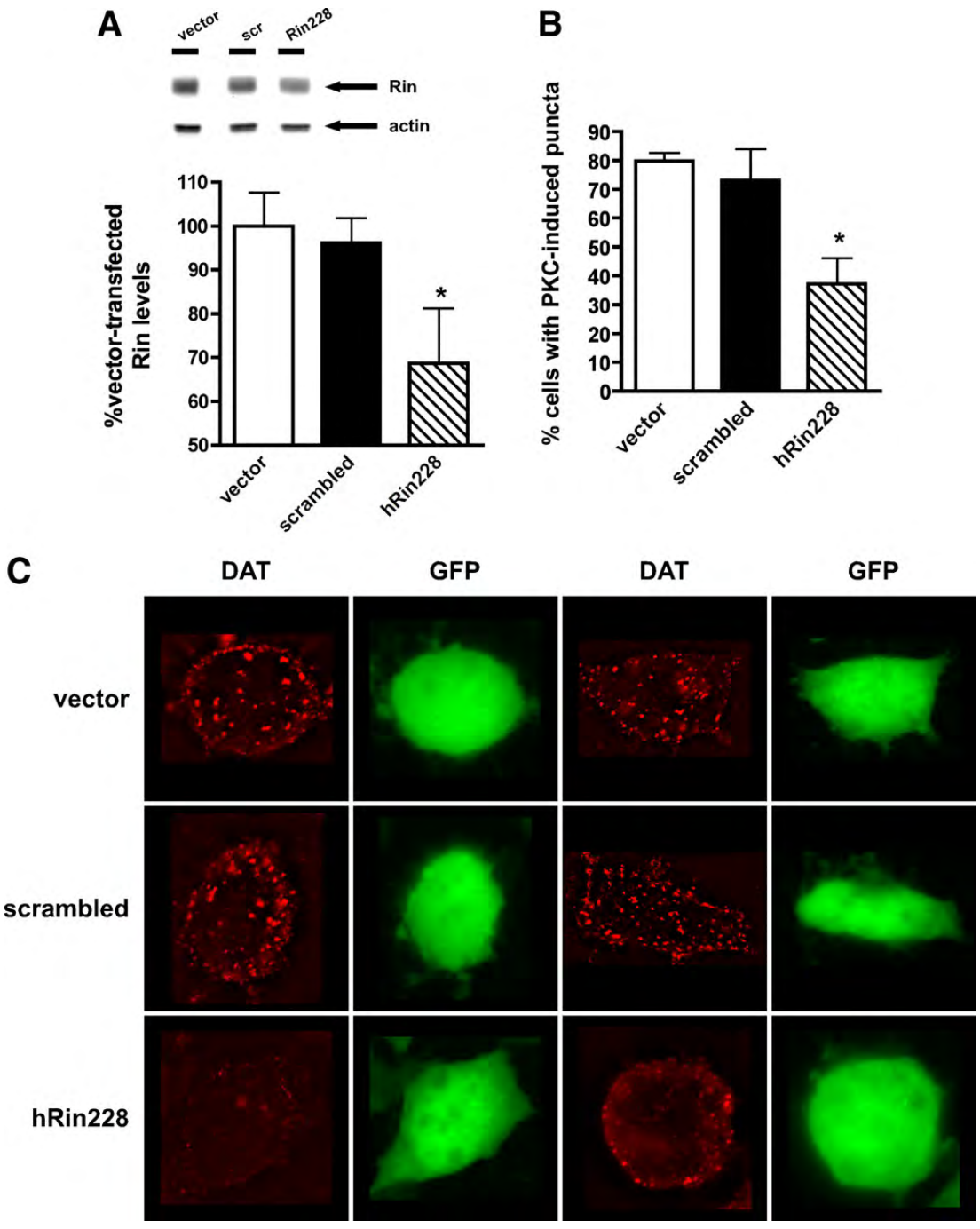
A
vector
scr
Rin228
Rin
actin
%vector-transfected Rin levels
110
100
90
80
70
60
50
*
vector
scrambled
hRin228
B
% cells with PKC-induced puncta
90
80
70
60
50
40
30
20
10
0
*
vector
scrambled
hRin228
C
DAT
GFP
DAT
GFP
vector
scrambled
hRin228

Figure 4.8. Rin is required for PKC-mediated DAT sequestration. hRin knockdown and antibody internalization assay. **A**. hRin knockdown. hRin-directed shRNAs were screened in HEK293 cells, 72 h after transfection. Top, Representative immunoblot showing Rin levels in vector-transfected, scrambled shRNA-transfected (scr), and hRin228-transfected cells, with actin probed as a loading control. Bottom, Averaged data. Data are expressed as percentage Rin levels compared with vector-transfected cells (normalized to actin loading control). *$p < 0.05$, significantly different from vector control (one-way ANOVA with Dunnett's post hoc analysis; $n = 5$). **B, C**. Antibody internalization assay. SK-N-MC cells cotransfected with EL2–HA–DAT and the indicated constructs were assayed 72 h after transfection. Cells were labeled with HA antibody, and DAT internalization was assessed for 15 min, 37°C in the presence of 1 μM PMA as described in Materials and Methods. Cells expressing shRNA constructs were identified by GFP coexpression. Optical z-stacks were collected and deconvolved as described in Materials and Methods. **B**. Averaged data. Data are expressed as percentage ± SEM cells exhibiting PMA-induced intracellular DAT puncta for each of the indicated transfection conditions. *$p < 0.05$, significantly different from vector-transfected control (one-way ANOVA with Dunnett's multiple comparison test; $n = 3$). **C**. Representative images. Planes through the cell center are shown for two cells per condition and are representative of 30–34 cells imaged per condition over three independent experiments.

exhibited PMA-induced DAT internalization when coexpressed with hRin228 (37.2 ± 8.9% cells; $p < 0.05$, one-way ANOVA with Dunnett's *post hoc* analysis). Rin knockdown effects on DAT internalization were not attributable to global perturbation of the endocytic machinery, because TfR endocytosis was identical in vector- versus hRin228-transfected cells, as assessed by Alexa Fluor 594–transferrin uptake (data not shown). These results demonstrate that Rin is absolutely essential for PKC-induced DAT sequestration.

Given that Rin is required for PKC-induced DAT sequestration, we used the hRin228 shRNA to ask whether Rin was required for PKC-mediated DAT functional downregulation. We measured robust [^{3}H]DA uptake in cells cotransfected with DAT and vector, and PKC activation significantly decreased DA uptake to 42.6 ± 11.1% of vehicle-treated cells ($p < 0.03$, Student's *t* test; $n = 4$; Figure 4.9). In contrast, PKC activation had no significant effect on DA uptake in cells cotransfected with DAT and hRin228 (106.3 ± 13.7% of vehicle-treated cells; $p = 0.72$, Student's *t* test; $n = 4$; Figure 4.9), consistent with the inability of DAT to sequester in a Rin-depleted environment.

DISCUSSION

In the current study, we sought to identify proteins that interacted with DAT residues 587–596 and were central to PKC-induced DAT sequestration. Using the hSOS rescue yeast two-hybrid approach, we determined that the neuronal GTPase Rin (Rit2) interacts with DAT residues 587–596

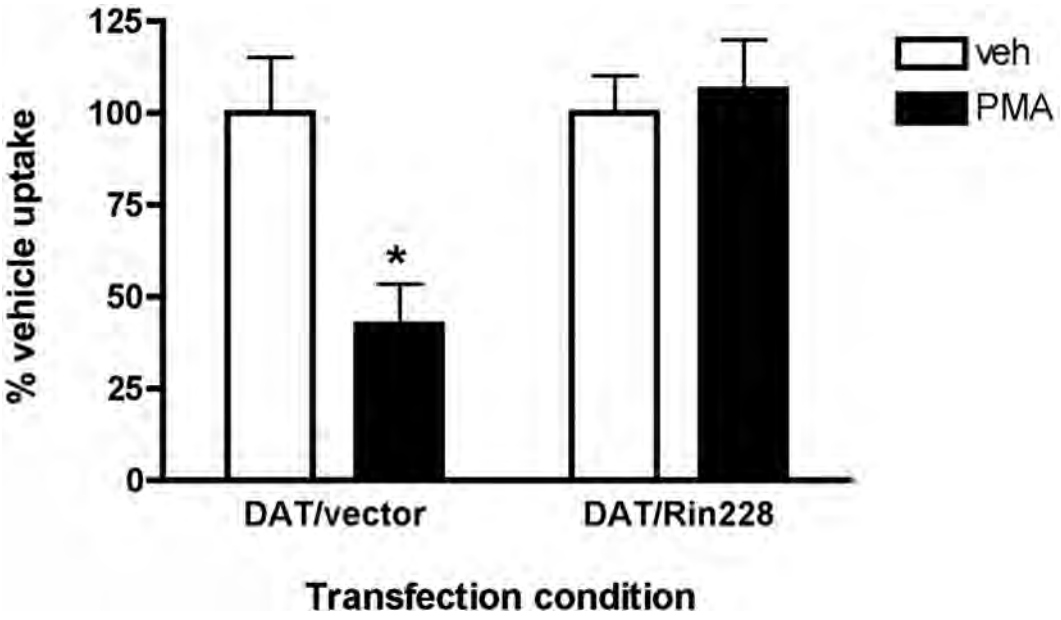

Figure 4.9. Rin is required for PKC-induced DAT functional downregulation. [^{3}H]DA uptake assays. SK-N-MC cells were cotransfected with DAT and the indicated constructs, and [3H]DA uptake was assessed 72 h after transfection. Cells were treated with or without 1µM PMA, 30 min, 37°C, followed by addition of [3H]DA as described in Materials and Methods. Averaged data are shown and are expressed as percentage ±SEM uptake of vehicle-treated cells. *$p < 0.03$, significantly different from vehicle-treated control (Student's t test; $n = 4$).

(FREKLAYAIA) and that Rin is absolutely required for PKC-induced DAT sequestration. Rin, also known as Rit2, is a member of the Rit subfamily of Ras-like small GTPases, which also includes the *Drosophila* homolog RIC [186]. These GTPases are highly conserved and are distinguished from other Ras-like GTPases in their lack of a C-terminal CaaX box for prenylation. Recent evidence suggests that a polybasic charged domain conserved at their C termini facilitates their plasma membrane association [174]. Whereas Rit is ubiquitously expressed, Rin expression is reported to be limited to neurons [173], and a recent report suggests that Rin expression is particularly enriched in dopaminergic neurons [187]. A recent study also revealed that Rin exhibits significant copy number variation in schizophrenic patient populations [188] and that a 5.3 Mb deletion encompassing the Rin gene on chromosome 18q12.3 is present in two patients with profound speech delay [189]. Together, these results suggest that Rin may play a central role in the pathophysiology of neuropsychiatric disorders.

What is known about the role of Rin in intracellular signaling, and how might that shed light onto downstream pathways that converge on DAT? Rin activates atypical PKC via interactions with the Par6/cdc42 complex [92,93] and a recent screen for endocytic determinants in *Caenorhabditis elegans* revealed that the Par6/cdc42 complex is absolutely required for transferrin receptor endocytosis, as well as for MHCI endocytic recycling [190]. Additionally, the Par6/cdc42/aPKC complex is required for E-cadherin endocytosis in

Drosophila [191]. Our results linking Rin to regulated DAT internalization raise the possibility that Rin may be an upstream signaling step in Par6/cdc42-dependent endocytosis. Rin also reportedly binds to and activates calmodulin [173]. Given that CaMKII interacts with the DAT C terminus and is essential for amphetamine-mediated DA efflux through DAT [94], it is possible that Rin may serve as a means to activate DAT-bound CaMKII via calmodulin activation. Rin is also required for nerve growth factor (NGF)-stimulated neurite extension [192-194] and p38 MAP kinase activation in response to NGF signaling [195]. Several reports link the MAP kinase signaling pathway to DAT trafficking [84,196-198], potentially implicating Rin in this process as well.

We detected Rin protein expression in striatal tissue and several dopaminergic cell lines, including SK-N-MC and PC12 (Figure 4.1A). In addition, we detected Rin in non-neuronal tissues and cell lines (Figure 4.1D), whereas previous studies reported that Rin mRNA expression was limited to neuronal tissues as determined by Northern blot and RT-PCR approaches [173]. This inconsistency is not attributable to lack of specificity of the Rin antibody, because it did not cross-react with GFP–Rit (data not shown). Moreover, we detected both Rit and Rin mRNA signals by RT-PCR in primary mouse embryonic kidney, PC12, and HeLa cells, as well as in whole brain and substantia nigra (data not shown). Thus, the apparent discrepancy between our results and previous reports may reflect a lack in sensitivity in the available approaches used at the

time the previous studies were performed. Alternatively, Rin may be ectopically expressed in transformed cell lines.

We observed DAT/Rin associations via coimmunoprecipitation in rat striatal tissue (Figure 4.1) and PC12 cells (Figures 4.1, 4.5). Additionally, colocalization studies revealed that the DAT/Rin interaction occurs at the plasma membrane in PC12 and HEK293 cell lines (Figures 4.2, 4.3, 4.6). We also wanted to determine whether DAT and Rin colocalize in native dopaminergic neurons. The commercially available Rin monoclonal antibody does not recognize Rin *in situ*, and our attempts at raising Rin-specific antisera were not successful, thwarting our ability to examine the DAT/Rin interaction in native preparations. As an alternative, we attempted to express CFP–Rin in primary ventral midbrain (VM) neurons using lentiviral infection. Despite successful generation of high-titer lentivirus, as determine by transduction of HEK293 cells, we were unable to reproducibly and efficiently transduce VM neurons in culture. Future studies will explore alternative gene delivery methods to further examine the DAT/Rin interaction *in situ*.

DAT/Rin interactions were significantly enriched in membrane raft regions within the membrane (Figure 4.2B-D). A recent report indicates that DAT localizes to both lipid raft and non-raft domains within the plasma membrane [177] and that DAT may be differentially regulated by PKC, depending on its microdomain localization. Moreover, Cremona *et al.* [176] recently reported that the membrane raft protein flotilin-1 is absolutely required for DAT localization to

lipid microdomains and for PKC-stimulated DAT sequestration. Thus, DAT/Rin interactions may occur in a specific lipid microdomain that facilitates enhanced endocytosis in response to PKC activation.

We recently reported that the charged residues at hDAT positions E589 and R590 contribute to a braking mechanism that dampens DAT endocytic rates under basal conditions but is released during PKC activation [90]. In agreement with our findings, Sorkina *et al.* [167] also recently confirmed the existence of a negative endocytic regulatory mechanism. Interestingly, results from that study demonstrated that the negative endocytic regulatory mechanism requires the DAT N terminus. The DAT N terminus is also the target of PKC-stimulated ubiquitination, and ubiquitination is required for PKC-mediated DAT internalization [168]. We observed increased DAT/Rin interactions in circumstances in which the DAT endocytic brake is released, either during PKC activation (Figure 4.5A) or when DAT residues 587–590 are mutated (Figure 4.5C, D). These results suggest that Rin plays a role in accelerating DAT endocytic rates. It also raises the possibility that there is a synergistic interaction between the DAT N and C termini that regulates the DAT endocytic rate.

A common approach to testing the role of small GTPases is the use of dominant-negative and constitutively active mutant GTPases, which are locked in the GTP-bound and GDP-bound states, respectively, and are unable to either hydrolyze GTP (constitutively active) or exchange GDP for GTP (dominant negative). Rin Q78L and S34N mutants have been described previously to

perturb Rin function in response to growth factor stimulation [195,199]. The Rin S34N mutant inhibited PKC-mediated DAT sequestration (Figure 4.6), consistent with a requisite role for Rin in PKC regulated DAT endocytosis. Interestingly, overexpression of wild-type Rin also inhibited PKC-stimulated DAT endocytosis. Overexpressed GTPases can have an inhibitory effect, because they can mislocalize and potentially sequester important factors required for vesicle trafficking [200]. Cellular imaging revealed that both of the Rin mutants fail to dissociate from DAT during internalization (Figure 4.7). Together with our coimmunoprecipitation results, these data suggest that Rin binds to the DAT C terminus to promote increased DAT internalization rates and then dissociates from DAT during guanyl nucleotide exchange. Rab GTPases are reported to function in a similar manner, with guanyl nucleotide exchange dictating Rab movement between membrane-bound compartments [201].

Rin depletion significantly inhibited PKC-mediated DAT sequestration (Figure 4.8). However, we should note that we did see PKC-induced DAT internalization in a population of cells with either high DAT expression or relatively low shRNA expression (correlated to GFP signal intensity). This is consistent with our previous report in which we observed that PKC-mediated DAT trafficking is highly sensitive to DAT expression levels [83], suggesting a readily saturable cellular process. Indeed, we also observed that excessively high DAT expression levels in HEK293 cells resulted in a loss of PKC-induced DAT sequestration (unpublished results). Surprisingly, Rin knockdown also

abolished PKC-mediated DAT functional downregulation (Figure 4.9). Foster *et al*. [177] recently reported both trafficking-dependent and -independent modes of PKC-mediated DAT downregulation, in contrast with our findings. The differences in our results may be attributable to different cell lines used (LLC-PK1 vs SK-N-MC) or may indicate that Rin is also required for trafficking-independent forms of PKC-mediated DAT downregulation. One possibility is that distinct PKC isoforms may participate in trafficking-dependent and -independent DAT regulatory mechanisms. A recent report suggests that PKCβ plays a central role in DAT trafficking [202]. In addition, previous studies demonstrated that multiple PKC isoforms are capable of functional DAT downregulation [203]. Because phorbol ester treatment activates multiple PKC isoforms, simultaneously, we cannot conclude whether or not specific PKC isoforms underlie the trafficking-dependent and -independent forms of DAT downregulation. However, future studies exploring the role of specific PKC isoforms in Rin-mediated DAT trafficking should be illuminating in this regard.

Recent studies have revealed a central role for biogenic amine transporter function in neuropsychiatric disorders, including ADHD [164] and autism [204]. Given the eminent role that transporters play, both as addictive and therapeutic drug targets, as well as in the pathophysiology of neuropsychiatric diseases, modulation of transporter availability by membrane trafficking is likely to have a significant impact on both normal and aberrant neurotransmission. The identification of Rin as a critical modulator of DAT trafficking and as a potentially

important link between DAT, CaMKII, and MAP kinase signaling will undoubtedly shed additional light on the mechanisms governing dopamine levels and plasticity in the brain. Moreover, these studies raise the possibility that Rin may play a larger role in synaptic endocytic trafficking.

EXPERIMENTAL PROCEDURES

Antibodies and reagents – Monoclonal rat anti-DAT antibodies were from Millipore Bioscience Research Reagents and mouse anti-Rin antibodies (clone 27G2) were from ExAlpha Biologics or Millipore. Rabbit anti-DAT polyclonal antibody was a generous gift from Dr. Roxanne Vaughan (University of North Dakota, Grand Forks, ND). cDNAs encoding HA–RinQ78L and HA–RinS34N (Spencer *et al*., 2002a) were kindly provided by Dr. Doug Andres (University of Kentucky, Lexington, KY). Mouse anti-green fluorescent protein (GFP) antibody and rat anti-HA antibody (clone 3F10) were from Roche, and mouse anti-actin antibody was from Santa Cruz Biotechnology. Mouse anti-HA (HA.11) antibody was acquired from Covance. Horseradish peroxidase (HRP)-conjugated secondary antibodies were from either Millipore Bioscience Research Reagents (anti-mouse) or Santa Cruz Biotechnology (anti-rat), and goat anti-mouse Fc fragment coupled to horseradish peroxidase was from Jackson ImmunoResearch. Fluorescently conjugated secondary antibodies and transferrin were from Invitrogen. [^{3}H]DA (dihydroxyphenylethylamine 3,4-[ring-2,5,6,-^{3}H]) was from PerkinElmer Life and Analytical Sciences, and sulfo-NHS-

SS-biotin was from Pierce. Phorbol 12-myristate 13-acetate (PMA) and GBR12909 (1-[2-[bis(4-fluorophenyl)-methoxy]ethyl]-4-[3-phenylpropyl]piperazine) were from Tocris Cookson. All other chemicals and reagents were from Sigma-Aldrich and Thermo Fisher Scientific and were of the highest grade available.

Yeast two-hybrid screen – A bait encoding human DAT amino acids 587–596 was constructed by amplifying hDAT cDNA region 1778–1807 with primers containing NotI and BglII sites and was cloned in-frame into the pSOS vector (Stratagene) at the NotI/BglII sites. The pSOS–DAT(586–597) bait was used to screen a CytoTrap XR substantia nigra cDNA library cloned into the pMyr vector (Stratagene). Positive interactions rescue Ras activity and permit yeast growth at the restrictive temperature. Positive clones were picked and underwent secondary and tertiary screening to rule out false positives attributable to temperature reversion. Plasmid DNA was isolated from tertiary positive clones, transformed into DH5αE bacteria (Invitrogen), amplified in liquid culture, and purified, and sequences were determined (Genewiz).

Cell culture and transfections – PC12 cells were maintained at 37°C, 10% CO_2 in DMEM (high glucose), 5% horse serum (Hyclone), and 5% bovine calf serum (Invitrogen) supplemented with 2 mM glutamine, 10^2 U/ml penicillin/streptomycin. Stably transfected PC12 cells expressing wild-type and 587–590(4A) DAT were

maintained as described previously [83,90,205] under selective pressure with 0.2 mg/ml G418 (Invitrogen). HEK293 cells were grown in DMEM, 10% fetal bovine serum, 2 mM glutamine, and 10^2 U/ml penicillin/streptomycin, 37°C, 5% CO_2. The human neuroblastoma cell line SK-N-MC was obtained from American Type Culture Collection and was maintained in MEM supplemented with 10% fetal bovine serum, 2 mM glutamine, and 10^2 U/ml penicillin/streptomycin, 37°C, 5% CO_2. HEK293 cells were transiently transfected with Lipofectamine 2000, according to the instructions of the manufacturer, using 2 µg of total DNA/7 × 10^5 cells, incubating with DNA/Lipofectamine complexes with cells 4 h for maximal cell viability. PC12 cells were transfected either by electroporation or using Lipofectamine 2000. For electroporation, 18.2 µg of DNA/1.1 × 10^7 PC12 cells in 0.75 ml of electroporation buffer (in mM: 137 NaCl, 5.0 KCl, 0.7 Na_2HPO_4, 6.0 glucose, and 20 HEPES, pH 7.05) was combined in 4 mm cuvettes and were electroporated using an exponential decay protocol at 300 V, 500 µF. Cells were resuspended in PC12 media supplemented with 3 mM EGTA and recovered 30 min, 37°C with occasional inversion. Cells were collected by centrifugation, resuspended in PC12 media, and plated as indicated. For Lipofectamine 2000 transfections, PC12 cells were seeded 1 d before transfection at 1 × 10^6 cells per well (six-well plates coated with 0.5 mg/ml poly-D-lysine; biochemical assays) or 2.25 × 10^5 per well (glass coverslips coated with 1.0 mg/ml poly-D-lysine for microscopy) in antibiotic-free PC12 media. Cells were transfected with either 4 µg (six-well plates) or 0.8 µg (glass coverslips)

total DNA at a 2.5:1 Lipofectamine/DNA ratio, according to the instructions of the manufacturer. Transfection solutions were replaced with fresh antibiotic-free media 16–24 h after transfection, and cells were assayed as described for each experiment. For SK-N-MC cells, 2.25×10^5 cells per well were plated 1 d before transfection in antibiotic-free media on either glass coverslips coated with 0.25 mg/ml poly-D-lysine (microscopy) or in uncoated 24-well tissue cultureware plates (uptake assays). Cells were transfected with 0.3 µg of total DNA per well at a 2:1 Lipofectamine/DNA ratio, according to the instructions of the manufacturer. Transfection solutions were replaced with fresh, antibiotic-free media 4 h after transfection, and cells were assayed as described for each experiment.

Coimmunoprecipitations – One $\times 10^6$ PC12 or PC12 cells stably expressing either wild-type or 587–590(4A) DAT were seeded in poly-D-lysine-coated six-well plates 1 d before experiments. Cells were treated as indicated, lysed in coimmunoprecipitation (co-IP) buffer (50 mM Tris, pH 7.4, 100 mM NaCl, 1% Triton X-100, 10% glycerol, and 1 mM EDTA) containing protease inhibitors (1.0 mM PMSF and 1.0 µg/ml each leupeptin, aprotinin, and pepstatin) and phosphatase inhibitors (10 mM sodium fluoride and 1 mM sodium orthovanadate), 30 min, 4°C with gentle shaking. Lysates were cleared by centrifugation (4°C), and protein concentrations were determined using the BCA Protein Assay (Pierce) with BSA standards. Equivalent amounts of cellular

protein underwent immunoprecipitation (overnight, 4°C) using Protein A/G beads (Pierce) precoated with the indicated antibodies. Supernatants were concentrated with Milliporespin filtration columns (10 kDa molecular weight cutoff), and beads were washed three times with co-IP buffer. Proteins were eluted by boiling in SDS-PAGE sample buffer containing 2 M urea (final concentration), and proteins were separated on 10% SDS-PAGE gels. After transfer to nitrocellulose, immunoblots were blocked with 5% nonfat dry milk, 0.1% Tween 20, and PBS, and proteins were detected with the indicated primary antibodies. To avoid detecting mouse IgG light chain in the immunoprecipitation complex, immunoreactive Rin bands were detected with goat anti-mouse F_c fragment coupled to HRP. Standard secondary antibodies conjugated to HRP were used to detect all other immunoreactive proteins. HRP-positive bands were visualized by reacting with Dura West Substrate (Pierce) and imaging with a VersaDoc imaging system (Bio-Rad). Nonsaturating bands were quantified using Quantity One software (Bio-Rad) and were normalized to the amount of DAT immunoprecipitated in the same reaction.

Glutathione S-transferase pull downs – hDAT cDNA nucleotides 1778–1879, corresponding to DAT amino acids 587–617, were amplified by PCR, and the product was cloned into the pGEX-5x-1 vector (GE Healthcare) downstream of and in-frame with glutathione *S*-transferase (GST). The DAT 587–590(4A) mutation was generated using QuikChange Mutagenesis (Stratagene), and all

construct sequences were confirmed by dideoxy chain termination sequencing (Genewiz). Plasmids were transformed into *Escherichia coli*BL21 and were cultured and induced with isopropyl-β-D-thiogalactopyranoside at 28°C to minimize fusion protein degradation, although some degradation was apparent in many of the assays. Fusion proteins were purified with glutathione agarose according to the instructions of the manufacturer, and protein purification was monitored at each step by SDS-PAGE with Coomassie staining. For pull downs, PC12 postnuclear supernatants were prepared with a ball-bearing cell homogenizer as described previously [205]. The indicated amount of cell homogenate was incubated with equivalent amounts of glutathione agarose bound to GST, GST–DAT 587–617, or GST–DAT 587–590(4A), 37°C, 1 h. Beads were washed three times with 50 mM Tris, pH 7.4, 150 mM NaCl, 1 mM EDTA, 1% Triton X-100, and 10% glycerol and were boiled in SDS-PAGE sample buffer, 5 min to elute bound proteins. Samples were resolved on SDS-PAGE gels and were immunoblotted for Rin and GST (to confirm pull down). Nonsaturating Rin bands were imaged as described above for coimmunoprecipitations, normalizing to GST band densities (GST + GST–DAT in cases when degradation occurred).

Fluorescence resonance energy transfer (FRET) – FRET [206] was measured with a Carl Zeiss Axiovert 200 epifluorescence microscope. The “three-filter method” was performed as described previously [181]. Images were taken using

63× oil-immersion objectives and Ludl filter wheels allowing a rapid excitation and emission filter exchange. We used HEK293 cells that were maintained and transiently transfected with plasmid cDNA (1.7 µg) by means of the calcium phosphate coprecipitation method as described previously [207]. The Ludl filter wheels were configured as follows: cyan fluorescent protein (CFP) (I_{Donor}; excitation, 436 nm; emission, 480 nm; and dichroic mirror, 455 nm), yellow fluorescent protein (YFP) ($I_{Acceptor}$; excitation, 500 nm; emission, 535 nm; and dichroic mirror, 515 nm), and FRET (I_{FRET}; excitation, 436 nm; emission, 535 nm; and dichroic mirror, 455 nm). Images were taken with a CCD camera (Coolsnap *fx*; Roper Scientific). Background fluorescence was subtracted from all images. We analyzed the images pixel by pixel using NIH ImageJ (version 1.43b; Wayne Rasband, National Institutes of Health, Bethesda, MD) and the NIH ImageJ plug-in PixFRET (pixel-by-pixel analysis of FRET with NIH ImageJ, version 1.5.0; [180]) with which spectral bleed-through parameters for the donor bleed through (BT) and the acceptor BT were determined and normalized FRET image (N_{FRET}) was calculated in the following way:

$$N_{FRET} = \frac{I_{FRET} - BT_{Donor} * I_{Donor} - BT_{Acceptor} * I_{Acceptor}}{\sqrt{I_{Donor} * I_{Acceptor}}} * 100,$$

The mean N_{FRET} was measured at the plasma membrane (predefined as the region of interest) using the computed N_{FRET} image. The regions of interest were selected in the CFP (donor) or YFP (acceptor) image (to avoid bleaching-associated bias) and transmitted to the N_{FRET} image by the NIH ImageJ Multi

Measure Tool. As negative control, we used the CFP-labeled form of DAT or Rin with a membrane-bound form of YFP [208] that was kindly provided by Viacheslav Nikolaev (University of Würzburg, Würzburg, Germany). As positive controls for membrane proteins, we used the serotonin transporter (SERT) tagged with CFP and YFP on its cytoplasmic N and C termini, respectively (to yield C-SERT-Y; [209]). We tagged DAT and Rin with CFP and YFP to reveal C-DAT and Y-DAT [181] as well as C-Rin and Y-Rin to compare the FRET values in Rin and DAT (and rule out any bias introduced by the different tags, although they differ only in a few amino acids). We also transfected HEK293 cells with combinations of C-DAT and Y-DAT as well as C-Rin and Y-Rin. The statistical significance of differences between the experimental conditions was determined using one-way ANOVA followed by Tukey's multiple comparison test.

Immunocytochemistry and microscopy – Cells were transfected with the indicated cDNAs at a 1:1 ratio and were assayed 48 h after transfection. Cells were treated as indicated, rinsed in PBS, and fixed in 4% paraformaldehyde prepared in PBS, 10 min, 25°C. Cells were blocked and permeabilized in blocking solution (PBS, 1% IgG/protease-free BSA, 5% goat serum, and 0.2% Triton X-100), 30 min, room temperature, followed by incubation with the indicated primary antibodies, 45 min, 25°C. Cells were washed with PBS and incubated with Alexa Fluor 594-, Alexa Fluor 405-, and Alexa Fluor 488-conjugated secondary antibodies (as indicated), 45 min, 25°C. Cells were

washed with PBS, dried, and mounted on glass slides with ProLong Gold mounting medium (Invitrogen). Immunoreactive cells were visualized as described previously [91] with a Carl Zeiss Axiovert 200M microscope using a 63×, 1.4 numerical aperture oil-immersion objective, and 0.4 µm optical sections were captured through the *z*-axis with a Retiga-1300R cooled CCD camera (Qimaging) using Slidebook 5.0 software (Intelligent Imaging Innovations). *z*-stacks were deconvolved with a constrained iterative algorithm using measured point-spread functions for each fluorescent channel. All images shown are single 0.4 µm planes through the center of each cell. For CTX colocalization studies, before fixing and staining cells, cells were incubated with 2.0 µg/ml Alexa Fluor 594-conjugated cholera toxin subunit B (CTX), 1 h, 4°C and were washed extensively in PBS^{2+} and 0.2% IgG/protease-free BSA. To quantify the percentage of DAT that colocalized with Rin (by volume, i.e., counting voxels) in CTX-positive and CTX-negative regions, we assessed each *z*-stack over a broad range of threshold triplets (i.e., a threshold for each of the three channels). Given the inherent signal intensity variability among cells and to avoid biasing our analysis, a range of thresholds (picked manually while viewing three-dimensional images) was deliberately set to be somewhat wider than the likely range. The lowest threshold allowed for some diffuse background fluorescence to remain; the highest threshold clearly was eroding the margins of labeled structures. Colocalization percentages were calculated at 10 equally spaced thresholds for each species, resulting in 1000 colocalization pairs for each cell. For each cell,

we examined the sensitivity (to the threshold) of the raft and non-raft colocalization percentages by creating a surface plot for the two percentages. A Wilcoxon's matched-pairs signed-rank test indicated significant difference across all thresholds. Therefore, single measurements at the median threshold were chosen for statistical analysis and data presentation.

Internalization assay – Relative initial internalization rates were measured using reversible biotinylation as described previously [83,90,91]. Cells were cotransfected with DAT and the indicated constructs at a 1:2 DAT/other cDNA ratio and were assayed 48–72 h after transfection. Briefly, transfected cells were biotinylated twice, 15 min, 4°C with 2.5 mg/ml NHS-SS-biotin and were quenched twice, 15 min, 4°C with 100 mM glycine. Cells were rapidly warmed to 37°C and incubated with or without 1 μM PMA, 10 min, 37°C, followed by rapidly cooling to 4°C to stop internalization. Residual surface biotin on internalization samples and stripping controls was stripped by reducing twice for 15 min, 4°C with 50 mM tris(2-carboxyethyl)phosphine. Cells were lysed, and biotinylated proteins were isolated with streptavidin agarose and analyzed by SDS-PAGE and immunoblotting for DAT. Immunoblots were probed in parallel for GFP and HA to confirm cotransfection with CFP–Rin (wild-type) and HA-tagged Rin mutants. Internalization rates were calculated as the percentage DAT internalized over 10 min compared with total surface protein labeled at time 0. Assays were only included if stripping efficiencies were >90%.

Short hairpin studies – Short hairpin RNAs (shRNAs) targeting 29 nt spans of the human Rin mRNA cloned into the pGFP-V-RS vector, which coexpresses turbo GFP, were purchased from Origene. hRin shRNA sequences were as follows: hRin228, GGTCCAGAGAGTACAAGGTGGTAATGCTG. hRin knockdown efficiencies were assessed in HEK293T cells, taking advantage of their relatively high transfection efficiency. Two × 10^5 cells were seeded into six-well culture plates 1 d before transfection. Cells were transfected using Lipofectamine 2000 (Invitrogen), using 4.0 µg of plasmid DNA per well and a Lipofectamine/DNA ratio of 2.5:1. Media was changed 4 h after transfection, and at 72 h after transfection, GFP-positive cells were enriched by flow cytometry (University of Massachusetts Medical School Flow Cytometry Core Facility). Cells were collected by centrifugation and lysed in RIPA buffer, and Rin levels were measured by quantitative immunoblotting equivalent amounts of cell lysate, normalizing to actin as a loading control. For knockdown experiments, SK-N-MC cells were transfected with Lipofectamine 2000 as described above, with equal amounts of DAT and the indicated plasmids, and were plated on either poly-D-lysine-coated glass coverslips (immunofluorescence) or 24-well tissue cultureware plates (uptake assays). All studies were conducted 72 h after transfection, and shRNA expression was confirmed by detecting GFP coexpression, by microscopy or immunoblot.

Antibody internalization assays – SK-N-MC cells were cotransfected with hDAT encoding an HA epitope tag in the second extracellular loop (ELA–HA–DAT) [86] and the indicated control or shRNA cDNAs at a 1:1 ratio. At 72 h after transfection, surface DAT was labeled with 2 µg/ml mouse anti-HA antibody, 30 min, room temperature. To monitor PKC-induced internalization, cells were extensively washed and rapidly warmed to 37°C in PBS^{2+} supplemented with 0.2% IgG and protease-free BSA, 0.18% glucose, and 1 µM PMA and were incubated in the same solution, 15 min, 37°C. Cells were rapidly washed in cold PBS to inhibit additional endocytic trafficking and were fixed in 4% paraformaldehyde in PBS, 10 min, room temperature. Residual surface HA antibody was blocked by incubating in 20 µg/ml goat anti-mouse secondary antibody in 5% normal goat serum and 1% IgG/protease-free BSA, 45 min, room temperature. Cells were washed three times in PBS and were permeabilized in 0.2% saponin in PBS containing 1% IgG and protease-free BSA, and 5% normal goat serum, 30 min, room temperature. Internalized HA antibody was detected by probing cells with goat anti-mouse secondary antibody conjugated to Alexa Fluor 594 (1:5000), 45 min, room temperature. Cells were washed three times in PBS, and coverslips were mounted in ProLong Gold. Images of GFP-positive cells were captured as described above for microscopy, using identical exposure times for all cells. For quantification, GFP-positive cells were scored blindly for PMA-induced DAT internalization, which was defined as the presence of multiple large (≥100 nm) intracellular puncta distinct from the plasma membrane and

visible in all three cell perspectives (*x–y*, *x–z*, and *y–z* axes). The percentage GFP-positive cells exhibiting PMA-induced DAT internalization for each transfection condition was averaged across multiple experiments, and significant differences in PMA-induced internalization were determined by one-way ANOVA with Dunnett's *post hoc* analysis compared with vector-transfected cells.

[^{3}H]DA uptake assays – Transfected cells were seeded onto 24-well plates, and [^{3}H]DA uptake was measured 48 h after transfection as reported previously [83,90]. Briefly, cells were rinsed and preincubated in KRH buffer (120 mM NaCl, 4.7 mM KCl, 2.2 mM $CaCl_2$, 1.2 mM $MgSO_4$, 1.2 mM KH_2PO_4, 0.18% glucose, and 10 mM HEPES, pH 7.4) at for 37°C for 30 min with the indicated drugs. Uptake was initiated by adding 1.0 µM [^{3}H]DA (PerkinElmer Life and Analytical Sciences) containing 10^{-5} M pargyline and 10^{-5} M ascorbic acid. Assays proceeded for 10 min (37°C) and were terminated by rapidly washing cells with ice-cold KRH buffer. Cells were solubilized in scintillation fluid, and accumulated radioactivity was determined by liquid scintillation counting in a Wallac Microbeta scintillation plate counter. Nonspecific uptake was defined in the presence of 10 µM GBR12909 and averaged <5% of total counts measured. Data analysis was performed using Microsoft Excel and GraphPad Prism Software.

CHAPTER V

DISCUSSION AND FUTURE STUDIES

The plasma membrane of eukaryotic cells contains all of the molecular machineries required to sense and respond to extracellular environmental cues. Endocytic sorting patterns can have profound effects on the organism as a whole and mammalian pathology has been reported in cases where normal protein sorting is disrupted. Two examples of molecules with different fates following internalization are the glucose transporter 4 (GLUT4), and EGFR. GLUT4, expressed in adipocytes and muscle cells, recycles to the plasma membrane following internalization. The relative amount of GLUT4 on the plasma membrane increases in response to insulin which mobilizes the transporter to the plasma membrane and into a rapid recycling pathway, allowing it to maintain a high relative concentration at the plasma membrane [210,211]. Telltale signs of insulin resistance and Type II diabetes can be associated with abnormalities in GLUT4 trafficking [210,212,213]. The EGFR expressed in epithelial cells, upon EGF binding, undergoes rapid internalization and degradation. Many types of cancers exhibit changes in EGFR levels that are brought about by disruption of the receptor's normal degradative mechanism [11,12]. The cellular and molecular mechanisms by which proteins with distinct intracellular fates are sorted are not fully understood. Insight into the molecular and cellular basis of

endocytosis requires experimental methods to detect the localization of multiple molecules within the 3-dimensional volume of the cell with high temporal and spatial resolution.

Previous studies utilizing ligands for TfR and EGFR determined that the sorting of ligands begins at the plasma membrane [49]. Additionally, it was found that EGF rapidly and specifically associates with EEA1, and that expression of EEA1 is required for the lysosomal degradation of EGFR [49]. The aim of Chapter 2 was to determine whether different internalization mechanisms are associated with distinct endosome populations. To address this question, I investigated whether Tf would be delivered from clathrin patches to specific endosome subpopulations. Endocytic recycling is a dynamic process requiring real-time acquisition of data. More importantly, in order to systematically visualize the internalization of Tf through clathrin and into a population of early endosomes we required an optical system equipped with three laser channels.

Prior to the start of biological experiments, our collaborators in the Biomedical Imaging and Engineering group designed a high resolution imaging platform that integrates TIRF and ESL microscopy called TESM. Importantly, TESM is equipped for the simultaneous visualization of three fluorophores allowing the systematic analysis of Tf cargo transferred from one cellular compartment to another in the early endocytic pathway. An additional feature of TESM is the spatial resolution brought by combining TIRF and ESL imaging, allowing us to generate high resolution 3-dimensional maps of the position of

endosomes relative to the cell surface. We developed not only a microscopy platform, but also analytical methodology to quantify the high resolution time lapse images generated. Analytical methods employed allow both population-based as well as single event-based analysis.

Utilizing TESM in conjunction with standard biochemical and molecular biological tools, I was able to define the role of Rabenosyn-5 in TfR endocytic recycling. Simultaneous imaging of clathrin, serving as the frame of reference, Tf, and various endosomal markers followed by quantitative image analysis and kinetic models determined that Rabenosyn-5 endosomes preferentially receive Tf immediately following entry through clathrin coated pits. Combined TIRF and ESL imaging revealed that Rabenosyn-5 endosomes reside proximal to clathrin patches at the plasma membrane while EEA1 endosomes are more distal from the plasma membrane. This provides a spatial and temporal framework for delivery of Tf into Rabenosyn-5 endosomes.

Biochemical analysis of Rabenosyn-5 knockdown gave insight into the functional role or Rabenosyn-5 in TfR endocytic recycling. Depletion of Rabneosyn-5 by siRNA led to an impairment in rapid TfR recycling in conjunction with an increase in TfR degradation, culminating in a marked reduction in TfR expression. These results are consistent with the concept of early endosome specialization, where endosomes containing Rabenosyn-5 capture cargo destined for recycling, while endosomes containing EEA1 capture internalized cargo destined to lysosomes.

Data presented here indicate Rabenosyn-5 is a crucial component of the endocytic recycling system involved in determining the recycling versus degradative fate of cargo internalized through clathrin coated pits. Like TfR, which requires Rabenosyn-5 for its proper expression and recycling, GLUT4 is internalized through clathrin coated pits and can recycle through the slow and fast endocytic recycling pathways. Rabenosyn-5 is known to engage in multivalent interactions with Rab GTPases, EHD proteins, Vps45 and PI(3)P. Eathiraj *et al.* [120] found that Rabenosyn-5 also interacts with Rab14, a known target for the insulin regulated GTPase activating protein AS160. Taken together with published data that Rabenosyn-5 binds EHD1 [70] and EHD1 has been shown to regulate GLUT4 recycling [214], the goal of future studies is to define and characterize the role of Rabenosyn-5 in constitutive and insulin-stimulated endocytic recycling of GLUT4.

Improved axial resolution within the TIRF zone reveals that subpopulations of endosomes exist that contain only Rabenosyn-5, only EEA1, and also a mixed population of endosomes containing both proteins. Further analysis is needed to understand what the functional roles are for these subpopulations and how they are generated. Given that Rabenosyn-5 binds to Rab5, Rab4, and PI(3)P, the amount of EEA1 binding to a Rabenosyn-5 endosomes may be dependent upon the concentration of PI(3)P and Rab5 on the endosomal membrane left unoccupied by Rabenosyn-5. In this regard, internalized activated growth factor receptor tyrosine kinases, which increase the

activity of PI3-kinase, and activate Rab5, would be expected to promote binding of EEA1 to its vesicle. Consistent with this are the published results of Nielsen *el al.* [32] in A431 cells transfected with Rab5 that showed extensive co-localization of EEA1 with Rabenosyn-5 on the same endosomal surface. While our data revels distinct and overlapping populations of early endosomes, the morphology of these populations is still unknown. Electron microscopy studies will provide insight into the structural identity of these endosomal regions. Additionally, it is unknown what happens to endosomal morphology following siRNA-mediated depletion of effector proteins such as Rabenosyn-5 and EEA1.

It was reported by Marsh *et al*. [215] that clustering of TfR reduced uptake. The multivalent Tf (Tf_{10}) used in these studies was reported to traffic much slower, be selectively retained in endocytic recycling compartments, and have a higher proportion trafficked for degradation [215]. It is important to note that the Tf_{10} used in these studies was large, thus confounding the difference between surface protein clustering and endocytosis and alterations in cargo size and endocytosis. The trafficking of oligomerized receptors through pathways that diverge from the less valent receptors may also be occurring at the plasma membrane. However, alterations in endocytosis may be a direct result of valency. For example, the clathrin coated pit is restricted in size. If the valency exceeds the capacity of the clathrin coated pit, as we find with Tf linked to 1µm Dynabeads®, internalization can be inhibited or potentially brought about through an alternate mechanism. Work by St. Pierre *et al*. [216] using fluorescent

anti-CD71, an antibody specific for the exofacial domain of TfR, also found increased colocalization of CD71 with late endosomal markers. While these studies showed a greater proportion of CD71 trafficked for degradation, a caveat of these studies is that experiments did not verify whether or not internalized CD71 remained bound to the TfR. It is possible that either 1) antibody binding of TfR, in the absence of multireceptor crosslinking, alters the receptor trafficking pathway or 2) following internalization of the antibody-receptor complex the antibody is released from the receptor and degraded while the receptor itself recycles normally.

The results shown in Chapter 2 combined with those of Leonard *et al*. [49] suggest that sorting of internalized cargo proceeds through the delivery of cargo from the plasma membrane into specialized endosome populations characterized by their topological organization relative to the plasma membrane. This differs from the classical understanding in which sorting occurs following delivery of cargo into a common type of early endosome. Testing this new model further will require the analysis of other types of cargo, such as LDL and platelet derived growth factor (PDGF), relative to specific endosome populations. Further studies examining GFP-LDLR and LDL-Alexa^{568} will aid our understanding of endosomal proteins involved in sorting LDL from recycling LDLR.

Surprisingly, in conjunction with the effect Rabenosyn-5 knockdown had on TfR, the dynamics of clathrin patches at the plasma membrane also appear to be altered. The number, size, and intensity of clathrin regions are increased

when Rabenosyn-5 is depleted. It is possible that Rabenosyn-5 may affect the efficiency of budding or scission of clathrin-coated vesicles. This data suggests a mechanistic link between Rabenosyn-5 and clathrin mediated endocytosis. It is interesting to note that Bucci *et al.* [19] reported that dominant negative Rab5 mutants impair Tf uptake and Rabenosyn-5 is a Rab5 effector with two Rab5 binding domains. Data presented here in conjunction with preliminary immunoprecipitation data suggest an association, direct or indirect, between Rabenosyn-5 and clathrin (Figure 5.1). This interaction could be mediated through EHD1 which has been shown to associate with Rabenosyn-5 [70], clathrin and its adaptor protein AP2 [217], and membrane bound tubules [218]. More extensive studies will determine if this interaction is specific, what protein(s) are involved, and what domains of Rabenosyn-5 are required.

The endocytic pathway may be a common mechanism for the transport of dsRNA. *Drosophila* S2 cells have been shown to utilize receptors to internalize dsRNA while in *C. elegans* the transmembrane protein SID-1 is required to import dsRNA from the environment. In mammals, miRNAs can be transferred form one cell to another via secreted exosomes.

The efficient intracellular uptake of RNAi compounds to tissues of interest remains a major hurdle in the development of RNAi as a therapeutic. The goal of the study outlined in Chapter 3 was to determine how siRNA silencing is connected to endocytic trafficking. In collaboration with RXi Pharmaceuticals with the use of patented sd-rxRNA, I discovered a pathway for siRNA transport

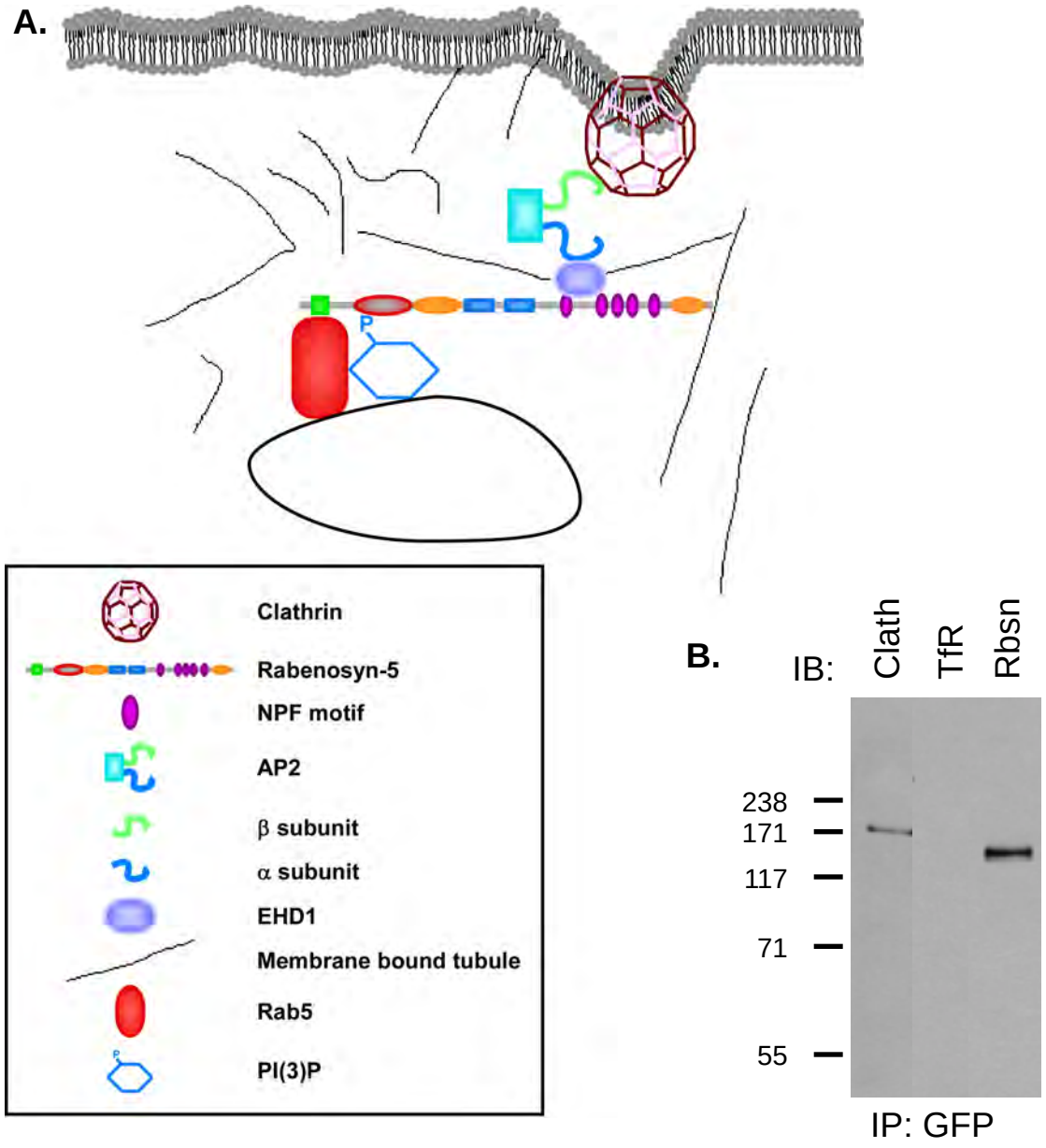

Figure 5.1. Link between Rabenosyn-5 and clathrin mediated endocytosis. A. Model for association between Rabenosyn-5 and clathrin. **B.** GFP immunoprecipitations from COS-7 stably expressing GFP-Rabenosyn-5 immunoblotted for Clathrin, TfR, and Rabenosyn-5.

whereby endosomes containing both Rabenosyn-5 and EEA1 receive internalized sd-rxRNA. While sd-rxRNA enters both endosomes, knockdown of EEA1 shows diminished silencing by the endocytosed sd-rxRNA. Future studies are needed to better understand how antisense oligonucleotides are targeted to EEA1 endosomes.

Antisense oligonucleotide activity is regulated by cargo sorting, but the sorting mechanism, which presumably would occur at the plasma membrane, is currently unknown. A detailed understanding of the mechanism of siRNA uptake will allow for the development of strategies to significantly enhance the utilization of RNAi therapeutic compounds.

Neurotransmitter transporters such as DAT traffic dynamically in a constitutive and regulated manner in response to stimuli and substrates. Recent work has focused on elucidating the mechanisms involved in transporter trafficking to and from the membrane. We previously defined the DAT internalization signal as a 10 amino acid stretch located in the protein C-terminus. The aim of Chapter 4 was to define molecular partners that interact with the DAT internalization signal. The small GTPase Rin was found to specifically interact with the DAT internalization signal. Interactions between DAT and Rin were confirmed by coimmunoprecipitations and immunofluorescence analysis revealed that this interaction occurs at the plasma membrane and is enriched in lipid rafts.

We previously reported that there exists an endocytic braking mechanism that attenuates DAT endocytic rates under basal conditions and this brake is released during PKC activation. In Chapter 4 we observed that interactions between DAT and Rin increase in response to PKC activation, or when the braking mechanism is released through alanine mutations of the involved residues. What this breaking mechanism is, and proteins or chemical modifications that it requires are still unknown and require further experimentation. Rin activity is required for PKC-induced DAT internalization as both dominant negative Rin expression, as well as shRNA mediated Rin depletion, significantly inhibit this internalization process.

I observed Rin, originally reported to be a neuronal specific GTPase, expression in neuronal and non-neuronal tissues and cell lines. The requirement for Rin in DAT trafficking and its expression in all tissues analyzed may help to explain why DAT trafficking has been successfully studied in non-neuronal cell lines, such as HEK293.

BIBLIOGRAPHY

1. Conner SD, Schmid SL (2003) Regulated portals of entry into the cell. Nature 422: 37-44.
2. Le Roy C, Wrana JL (2005) Clathrin- and non-clathrin-mediated endocytic regulation of cell signalling. Nat Rev Mol Cell Biol 6: 112-126.
3. Brown MS, Goldstein JL (1979) Receptor-mediated endocytosis: insights from the lipoprotein receptor system. Proc Natl Acad Sci U S A 76: 3330-3337.
4. Hobbs HH, Russell DW, Brown MS, Goldstein JL (1990) The LDL receptor locus in familial hypercholesterolemia: mutational analysis of a membrane protein. Annu Rev Genet 24: 133-170.
5. Brown MS, Goldstein JL (1986) A receptor-mediated pathway for cholesterol homeostasis. Science 232: 34-47.
6. Rudenko G, Deisenhofer J (2003) The low-density lipoprotein receptor: ligands, debates and lore. Curr Opin Struct Biol 13: 683-689.
7. Davis CG, Lehrman MA, Russell DW, Anderson RG, Brown MS, et al. (1986) The J.D. mutation in familial hypercholesterolemia: amino acid substitution in cytoplasmic domain impedes internalization of LDL receptors. Cell 45: 15-24.
8. Via LE, Deretic D, Ulmer RJ, Hibler NS, Huber LA, et al. (1997) Arrest of mycobacterial phagosome maturation is caused by a block in vesicle fusion between stages controlled by rab5 and rab7. J Biol Chem 272: 13326-13331.
9. Garvey WT, Maianu L, Zhu JH, Brechtel-Hook G, Wallace P, et al. (1998) Evidence for defects in the trafficking and translocation of GLUT4 glucose transporters in skeletal muscle as a cause of human insulin resistance. J Clin Invest 101: 2377-2386.
10. Dugan JM, deWit C, McConlogue L, Maltese WA (1995) The Ras-related GTP-binding protein, Rab1B, regulates early steps in exocytic transport and processing of beta-amyloid precursor protein. J Biol Chem 270: 10982-10989.
11. Mendelsohn J, Baselga J (2000) The EGF receptor family as targets for cancer therapy. Oncogene 19: 6550-6565.
12. Yarden Y, Sliwkowski MX (2001) Untangling the ErbB signalling network. Nat Rev Mol Cell Biol 2: 127-137.
13. Behnia R, Munro S (2005) Organelle identity and the signposts for membrane traffic. Nature 438: 597-604.
14. De Matteis MA, Di Campli A, Godi A (2005) The role of the phosphoinositides at the Golgi complex. Biochim Biophys Acta 1744: 396-405.
15. Di Paolo G, De Camilli P (2006) Phosphoinositides in cell regulation and membrane dynamics. Nature 443: 651-657.
16. Odorizzi G, Babst M, Emr SD (2000) Phosphoinositide signaling and the regulation of membrane trafficking in yeast. Trends Biochem Sci 25: 229-235.

17. Zerial M, McBride H (2001) Rab proteins as membrane organizers. Nat Rev Mol Cell Biol 2: 107-117.
18. Barbieri MA, Roberts RL, Mukhopadhyay A, Stahl PD (1996) Rab5 regulates the dynamics of early endosome fusion. Biocell 20: 331-338.
19. Bucci C, Parton RG, Mather IH, Stunnenberg H, Simons K, et al. (1992) The small GTPase rab5 functions as a regulatory factor in the early endocytic pathway. Cell 70: 715-728.
20. Lippe R, Miaczynska M, Rybin V, Runge A, Zerial M (2001) Functional synergy between Rab5 effector Rabaptin-5 and exchange factor Rabex-5 when physically associated in a complex. Mol Biol Cell 12: 2219-2228.
21. Nielsen E, Severin F, Backer JM, Hyman AA, Zerial M (1999) Rab5 regulates motility of early endosomes on microtubules. Nat Cell Biol 1: 376-382.
22. Stenmark H, Parton RG, Steele-Mortimer O, Lutcke A, Gruenberg J, et al. (1994) Inhibition of rab5 GTPase activity stimulates membrane fusion in endocytosis. EMBO J 13: 1287-1296.
23. Daro E, van der Sluijs P, Galli T, Mellman I (1996) Rab4 and cellubrevin define different early endosome populations on the pathway of transferrin receptor recycling. Proc Natl Acad Sci U S A 93: 9559-9564.
24. Sheff DR, Daro EA, Hull M, Mellman I (1999) The receptor recycling pathway contains two distinct populations of early endosomes with different sorting functions. J Cell Biol 145: 123-139.
25. van der Sluijs P, Hull M, Webster P, Male P, Goud B, et al. (1992) The small GTP-binding protein rab4 controls an early sorting event on the endocytic pathway. Cell 70: 729-740.
26. Sonnichsen B, De Renzis S, Nielsen E, Rietdorf J, Zerial M (2000) Distinct membrane domains on endosomes in the recycling pathway visualized by multicolor imaging of Rab4, Rab5, and Rab11. J Cell Biol 149: 901-914.
27. Furman CA, Chen R, Guptaroy B, Zhang M, Holz RW, et al. (2009) Dopamine and amphetamine rapidly increase dopamine transporter trafficking to the surface: live-cell imaging using total internal reflection fluorescence microscopy. J Neurosci 29: 3328-3336.
28. Wishart MJ, Dixon JE (2002) PTEN and myotubularin phosphatases: from 3-phosphoinositide dephosphorylation to disease. Trends Cell Biol 12: 579-585.
29. Stenmark H, Aasland R, Driscoll PC (2002) The phosphatidylinositol 3-phosphate-binding FYVE finger. FEBS Lett 513: 77-84.
30. Stenmark H, Aasland R, Toh BH, D'Arrigo A (1996) Endosomal localization of the autoantigen EEA1 is mediated by a zinc-binding FYVE finger. J Biol Chem 271: 24048-24054.
31. Shin HW, Hayashi M, Christoforidis S, Lacas-Gervais S, Hoepfner S, et al. (2005) An enzymatic cascade of Rab5 effectors regulates phosphoinositide turnover in the endocytic pathway. J Cell Biol 170: 607-618.

32. Nielsen E, Christoforidis S, Uttenweiler-Joseph S, Miaczynska M, Dewitte F, et al. (2000) Rabenosyn-5, a novel Rab5 effector, is complexed with hVPS45 and recruited to endosomes through a FYVE finger domain. J Cell Biol 151: 601-612.
33. Christoforidis S, Miaczynska M, Ashman K, Wilm M, Zhao L, et al. (1999) Phosphatidylinositol-3-OH kinases are Rab5 effectors. Nat Cell Biol 1: 249-252.
34. Simonsen A, Lippe R, Christoforidis S, Gaullier JM, Brech A, et al. (1998) EEA1 links PI(3)K function to Rab5 regulation of endosome fusion. Nature 394: 494-498.
35. Backer JM (2000) Phosphoinositide 3-kinases and the regulation of vesicular trafficking. Mol Cell Biol Res Commun 3: 193-204.
36. Backer JM (2008) The regulation and function of Class III PI3Ks: novel roles for Vps34. Biochem J 410: 1-17.
37. Schnatwinkel C, Christoforidis S, Lindsay MR, Uttenweiler-Joseph S, Wilm M, et al. (2004) The Rab5 effector Rabankyrin-5 regulates and coordinates different endocytic mechanisms. PLoS Biol 2: E261.
38. Corvera S, D'Arrigo A, Stenmark H (1999) Phosphoinositides in membrane traffic. Curr Opin Cell Biol 11: 460-465.
39. Gaullier JM, Simonsen A, D'Arrigo A, Bremnes B, Stenmark H, et al. (1998) FYVE fingers bind PtdIns(3)P. Nature 394: 432-433.
40. Stenmark H, Aasland R (1999) FYVE-finger proteins--effectors of an inositol lipid. J Cell Sci 112 (Pt 23): 4175-4183.
41. de Renzis S, Sonnichsen B, Zerial M (2002) Divalent Rab effectors regulate the sub-compartmental organization and sorting of early endosomes. Nat Cell Biol 4: 124-133.
42. McBride HM, Rybin V, Murphy C, Giner A, Teasdale R, et al. (1999) Oligomeric complexes link Rab5 effectors with NSF and drive membrane fusion via interactions between EEA1 and syntaxin 13. Cell 98: 377-386.
43. Hayes S, Chawla A, Corvera S (2002) TGF beta receptor internalization into EEA1-enriched early endosomes: role in signaling to Smad2. J Cell Biol 158: 1239-1249.
44. Bonifacino JS, Traub LM (2003) Signals for sorting of transmembrane proteins to endosomes and lysosomes. Annu Rev Biochem 72: 395-447.
45. Gruenberg J (2003) Lipids in endocytic membrane transport and sorting. Curr Opin Cell Biol 15: 382-388.
46. Jovic M, Sharma M, Rahajeng J, Caplan S The early endosome: a busy sorting station for proteins at the crossroads. Histol Histopathol 25: 99-112.
47. Maxfield FR, McGraw TE (2004) Endocytic recycling. Nat Rev Mol Cell Biol 5: 121-132.
48. Mellman I (1996) Endocytosis and molecular sorting. Annu Rev Cell Dev Biol 12: 575-625.

49. Leonard D, Hayakawa A, Lawe D, Lambright D, Bellve KD, et al. (2008) Sorting of EGF and transferrin at the plasma membrane and by cargo-specific signaling to EEA1-enriched endosomes. J Cell Sci 121: 3445-3458.
50. Hoeller D, Volarevic S, Dikic I (2005) Compartmentalization of growth factor receptor signalling. Curr Opin Cell Biol 17: 107-111.
51. Schlessinger J, Ullrich A (1992) Growth factor signaling by receptor tyrosine kinases. Neuron 9: 383-391.
52. Thompson DM, Gill GN (1985) The EGF receptor: structure, regulation and potential role in malignancy. Cancer Surv 4: 767-788.
53. Ullrich A, Schlessinger J (1990) Signal transduction by receptors with tyrosine kinase activity. Cell 61: 203-212.
54. Pawson T (2004) Specificity in signal transduction: from phosphotyrosine-SH2 domain interactions to complex cellular systems. Cell 116: 191-203.
55. Haglund K, Di Fiore PP, Dikic I (2003) Distinct monoubiquitin signals in receptor endocytosis. Trends Biochem Sci 28: 598-603.
56. Katzmann DJ, Odorizzi G, Emr SD (2002) Receptor downregulation and multivesicular-body sorting. Nat Rev Mol Cell Biol 3: 893-905.
57. van Renswoude J, Bridges KR, Harford JB, Klausner RD (1982) Receptor-mediated endocytosis of transferrin and the uptake of fe in K562 cells: identification of a nonlysosomal acidic compartment. Proc Natl Acad Sci U S A 79: 6186-6190.
58. Hopkins CR, Gibson A, Shipman M, Strickland DK, Trowbridge IS (1994) In migrating fibroblasts, recycling receptors are concentrated in narrow tubules in the pericentriolar area, and then routed to the plasma membrane of the leading lamella. J Cell Biol 125: 1265-1274.
59. Klausner RD, Ashwell G, van Renswoude J, Harford JB, Bridges KR (1983) Binding of apotransferrin to K562 cells: explanation of the transferrin cycle. Proc Natl Acad Sci U S A 80: 2263-2266.
60. Li G, D'Souza-Schorey C, Barbieri MA, Roberts RL, Klippel A, et al. (1995) Evidence for phosphatidylinositol 3-kinase as a regulator of endocytosis via activation of Rab5. Proc Natl Acad Sci U S A 92: 10207-10211.
61. Shpetner H, Joly M, Hartley D, Corvera S (1996) Potential sites of PI-3 kinase function in the endocytic pathway revealed by the PI-3 kinase inhibitor, wortmannin. J Cell Biol 132: 595-605.
62. Steinman RM, Silver JM, Cohn ZA (1974) Pinocytosis in fibroblasts. Quantitative studies in vitro. J Cell Biol 63: 949-969.
63. Katz JH (1961) Iron and protein kinetics studied by means of doubly labeled human crystalline transferrin. J Clin Invest 40: 2143-2152.
64. Anderson RG, Brown MS, Goldstein JL (1977) Role of the coated endocytic vesicle in the uptake of receptor-bound low density lipoprotein in human fibroblasts. Cell 10: 351-364.
65. Hayakawa A, Leonard D, Murphy S, Hayes S, Soto M, et al. (2006) The WD40 and FYVE domain containing protein 2 defines a class of early

endosomes necessary for endocytosis. Proc Natl Acad Sci U S A 103: 11928-11933.
66. Lakadamyali M, Rust MJ, Zhuang X (2006) Ligands for clathrin-mediated endocytosis are differentially sorted into distinct populations of early endosomes. Cell 124: 997-1009.
67. Miaczynska M, Christoforidis S, Giner A, Shevchenko A, Uttenweiler-Joseph S, et al. (2004) APPL proteins link Rab5 to nuclear signal transduction via an endosomal compartment. Cell 116: 445-456.
68. Abe M, Setoguchi Y, Tanaka T, Awano W, Takahashi K, et al. (2009) Membrane protein location-dependent regulation by PI3K (III) and rabenosyn-5 in Drosophila wing cells. PLoS One 4: e7306.
69. Wilson JM, de Hoop M, Zorzi N, Toh BH, Dotti CG, et al. (2000) EEA1, a tethering protein of the early sorting endosome, shows a polarized distribution in hippocampal neurons, epithelial cells, and fibroblasts. Mol Biol Cell 11: 2657-2671.
70. Naslavsky N, Boehm M, Backlund PS, Jr., Caplan S (2004) Rabenosyn-5 and EHD1 interact and sequentially regulate protein recycling to the plasma membrane. Mol Biol Cell 15: 2410-2422.
71. Axelrod D (2001) Total internal reflection fluorescence microscopy in cell biology. Traffic 2: 764-774.
72. Gustafsson MG (2000) Surpassing the lateral resolution limit by a factor of two using structured illumination microscopy. J Microsc 198: 82-87.
73. Huvenne H, Smagghe G Mechanisms of dsRNA uptake in insects and potential of RNAi for pest control: a review. J Insect Physiol 56: 227-235.
74. Jose AM, Hunter CP (2007) Transport of sequence-specific RNA interference information between cells. Annu Rev Genet 41: 305-330.
75. Whangbo JS, Hunter CP (2008) Environmental RNA interference. Trends Genet 24: 297-305.
76. Rajagopal R, Sivakumar S, Agrawal N, Malhotra P, Bhatnagar RK (2002) Silencing of midgut aminopeptidase N of Spodoptera litura by double-stranded RNA establishes its role as Bacillus thuringiensis toxin receptor. J Biol Chem 277: 46849-46851.
77. Winston WM, Sutherlin M, Wright AJ, Feinberg EH, Hunter CP (2007) Caenorhabditis elegans SID-2 is required for environmental RNA interference. Proc Natl Acad Sci U S A 104: 10565-10570.
78. Bennasser Y, Le SY, Benkirane M, Jeang KT (2005) Evidence that HIV-1 encodes an siRNA and a suppressor of RNA silencing. Immunity 22: 607-619.
79. Elbashir SM, Harborth J, Lendeckel W, Yalcin A, Weber K, et al. (2001) Duplexes of 21-nucleotide RNAs mediate RNA interference in cultured mammalian cells. Nature 411: 494-498.
80. Reynolds A, Anderson EM, Vermeulen A, Fedorov Y, Robinson K, et al. (2006) Induction of the interferon response by siRNA is cell type- and duplex length-dependent. RNA 12: 988-993.

81. Torres GE, Gainetdinov RR, Caron MG (2003) Plasma membrane monoamine transporters: structure, regulation and function. Nat Rev Neurosci 4: 13-25.
82. Chen NH, Reith ME, Quick MW (2004) Synaptic uptake and beyond: the sodium- and chloride-dependent neurotransmitter transporter family SLC6. Pflugers Arch 447: 519-531.
83. Loder MK, Melikian HE (2003) The dopamine transporter constitutively internalizes and recycles in a protein kinase C-regulated manner in stably transfected PC12 cell lines. J Biol Chem 278: 22168-22174.
84. Mortensen OV, Larsen MB, Prasad BM, Amara SG (2008) Genetic complementation screen identifies a mitogen-activated protein kinase phosphatase, MKP3, as a regulator of dopamine transporter trafficking. Mol Biol Cell 19: 2818-2829.
85. Sorkina T, Hoover BR, Zahniser NR, Sorkin A (2005) Constitutive and protein kinase C-induced internalization of the dopamine transporter is mediated by a clathrin-dependent mechanism. Traffic 6: 157-170.
86. Sorkina T, Miranda M, Dionne KR, Hoover BR, Zahniser NR, et al. (2006) RNA interference screen reveals an essential role of Nedd4-2 in dopamine transporter ubiquitination and endocytosis. J Neurosci 26: 8195-8205.
87. Melikian HE (2004) Neurotransmitter transporter trafficking: endocytosis, recycling, and regulation. Pharmacol Ther 104: 17-27.
88. Robinson MB (2002) Regulated trafficking of neurotransmitter transporters: common notes but different melodies. J Neurochem 80: 1-11.
89. Zahniser NR, Doolen S (2001) Chronic and acute regulation of Na+/Cl- -dependent neurotransmitter transporters: drugs, substrates, presynaptic receptors, and signaling systems. Pharmacol Ther 92: 21-55.
90. Boudanova E, Navaroli DM, Stevens Z, Melikian HE (2008) Dopamine transporter endocytic determinants: carboxy terminal residues critical for basal and PKC-stimulated internalization. Mol Cell Neurosci 39: 211-217.
91. Holton KL, Loder MK, Melikian HE (2005) Nonclassical, distinct endocytic signals dictate constitutive and PKC-regulated neurotransmitter transporter internalization. Nat Neurosci 8: 881-888.
92. Hoshino M, Nakamura S (2003) Small GTPase Rin induces neurite outgrowth through Rac/Cdc42 and calmodulin in PC12 cells. J Cell Biol 163: 1067-1076.
93. Hoshino M, Yoshimori T, Nakamura S (2005) Small GTPase proteins Rin and Rit Bind to PAR6 GTP-dependently and regulate cell transformation. J Biol Chem 280: 22868-22874.
94. Fog JU, Khoshbouei H, Holy M, Owens WA, Vaegter CB, et al. (2006) Calmodulin kinase II interacts with the dopamine transporter C terminus to regulate amphetamine-induced reverse transport. Neuron 51: 417-429.
95. Doherty GJ, McMahon HT (2009) Mechanisms of endocytosis. Annu Rev Biochem 78: 857-902.

96. Gruenberg J, Maxfield FR (1995) Membrane transport in the endocytic pathway. Curr Opin Cell Biol 7: 552-563.
97. Mellman I (1995) Molecular sorting of membrane proteins in polarized and nonpolarized cells. Cold Spring Harb Symp Quant Biol 60: 745-752.
98. Li L, Guan KL (2009) Amino acid signaling to TOR activation: Vam6 functioning as a Gtr1 GEF. Mol Cell 35: 543-545.
99. Sancak Y, Bar-Peled L, Zoncu R, Markhard AL, Nada S, et al. (2010) Ragulator-Rag complex targets mTORC1 to the lysosomal surface and is necessary for its activation by amino acids. Cell 141: 290-303.
100. Gibbings DJ, Ciaudo C, Erhardt M, Voinnet O (2009) Multivesicular bodies associate with components of miRNA effector complexes and modulate miRNA activity. Nat Cell Biol 11: 1143-1149.
101. Lee YS, Pressman S, Andress AP, Kim K, White JL, et al. (2009) Silencing by small RNAs is linked to endosomal trafficking. Nat Cell Biol 11: 1150-1156.
102. Siomi H, Siomi MC (2009) RISC hitches onto endosome trafficking. Nat Cell Biol 11: 1049-1051.
103. Collinet C, Stoter M, Bradshaw CR, Samusik N, Rink JC, et al. (2010) Systems survey of endocytosis by multiparametric image analysis. Nature 464: 243-249.
104. Zoncu R, Perera RM, Balkin DM, Pirruccello M, Toomre D, et al. (2009) A phosphoinositide switch controls the maturation and signaling properties of APPL endosomes. Cell 136: 1110-1121.
105. Sheff D, Pelletier L, O'Connell CB, Warren G, Mellman I (2002) Transferrin receptor recycling in the absence of perinuclear recycling endosomes. J Cell Biol 156: 797-804.
106. Traub LM (2011) Regarding the amazing choreography of clathrin coats. PLoS Biol 9: e1001037.
107. Karadaglic D, Wilson T (2008) Image formation in structured illumination wide-field fluorescence microscopy. Micron 39: 808-818.
108. Neil MA, Juskaitis R, Wilson T (1997) Method of obtaining optical sectioning by using structured light in a conventional microscope. Opt Lett 22: 1905-1907.
109. Christoforidis S, McBride HM, Burgoyne RD, Zerial M (1999) The Rab5 effector EEA1 is a core component of endosome docking. Nature 397: 621-625.
110. Dumas JJ, Merithew E, Sudharshan E, Rajamani D, Hayes S, et al. (2001) Multivalent endosome targeting by homodimeric EEA1. Mol Cell 8: 947-958.
111. Lindmo K, Stenmark H (2006) Regulation of membrane traffic by phosphoinositide 3-kinases. J Cell Sci 119: 605-614.
112. Bellve KD, Leonard D, Standley C, Lifshitz LM, Tuft RA, et al. (2006) Plasma membrane domains specialized for clathrin-mediated endocytosis in primary cells. J Biol Chem 281: 16139-16146.

113. Merrifield CJ, Perrais D, Zenisek D (2005) Coupling between clathrin-coated-pit invagination, cortactin recruitment, and membrane scission observed in live cells. Cell 121: 593-606.
114. Traub LM (2009) Clathrin couture: fashioning distinctive membrane coats at the cell surface. PLoS Biol 7: e1000192.
115. Zaliauskiene L, Kang S, Brouillette CG, Lebowitz J, Arani RB, et al. (2000) Down-regulation of cell surface receptors is modulated by polar residues within the transmembrane domain. Mol Biol Cell 11: 2643-2655.
116. Yoon HY, Lee JS, Randazzo PA (2008) ARAP1 regulates endocytosis of EGFR. Traffic 9: 2236-2252.
117. Conner SD, Schmid SL (2003) Differential requirements for AP-2 in clathrin-mediated endocytosis. J Cell Biol 162: 773-779.
118. Gengyo-Ando K, Kuroyanagi H, Kobayashi T, Murate M, Fujimoto K, et al. (2007) The SM protein VPS-45 is required for RAB-5-dependent endocytic transport in Caenorhabditis elegans. EMBO Rep 8: 152-157.
119. Morrison HA, Dionne H, Rusten TE, Brech A, Fisher WW, et al. (2008) Regulation of early endosomal entry by the Drosophila tumor suppressors Rabenosyn and Vps45. Mol Biol Cell 19: 4167-4176.
120. Eathiraj S, Pan X, Ritacco C, Lambright DG (2005) Structural basis of family-wide Rab GTPase recognition by rabenosyn-5. Nature 436: 415-419.
121. Wegner CS, Malerod L, Pedersen NM, Progida C, Bakke O, et al. (2010) Ultrastructural characterization of giant endosomes induced by GTPase-deficient Rab5. Histochem Cell Biol 133: 41-55.
122. Hamasaki M, Araki N, Hatae T (2004) Association of early endosomal autoantigen 1 with macropinocytosis in EGF-stimulated A431 cells. Anat Rec A Discov Mol Cell Evol Biol 277: 298-306.
123. Bryant DM, Kerr MC, Hammond LA, Joseph SR, Mostov KE, et al. (2007) EGF induces macropinocytosis and SNX1-modulated recycling of E-cadherin. J Cell Sci 120: 1818-1828.
124. Barbieri MA, Roberts RL, Gumusboga A, Highfield H, Alvarez-Dominguez C, et al. (2000) Epidermal growth factor and membrane trafficking. EGF receptor activation of endocytosis requires Rab5a. J Cell Biol 151: 539-550.
125. Shaner NC, Lin MZ, McKeown MR, Steinbach PA, Hazelwood KL, et al. (2008) Improving the photostability of bright monomeric orange and red fluorescent proteins. Nat Methods 5: 545-551.
126. Lawe DC, Chawla A, Merithew E, Dumas J, Carrington W, et al. (2002) Sequential roles for phosphatidylinositol 3-phosphate and Rab5 in tethering and fusion of early endosomes via their interaction with EEA1. J Biol Chem 277: 8611-8617.
127. Saito T, Jones CC, Huang S, Czech MP, Pilch PF (2007) The interaction of Akt with APPL1 is required for insulin-stimulated Glut4 translocation. J Biol Chem 282: 32280-32287.

128. Lifshitz LM, Collins JA, Moore ED, Gauch J (1994) Computer vision and graphics in fluorescence microscopy. Proceedings of the IEEE Workshop on Biomedical Image Analysis: 166-175.
129. Giannetti AM, Bjorkman PJ (2004) HFE and transferrin directly compete for transferrin receptor in solution and at the cell surface. J Biol Chem 279: 25866-25875.
130. Fire A, Xu S, Montgomery MK, Kostas SA, Driver SE, et al. (1998) Potent and specific genetic interference by double-stranded RNA in Caenorhabditis elegans. Nature 391: 806-811.
131. Zamore PD, Tuschl T, Sharp PA, Bartel DP (2000) RNAi: double-stranded RNA directs the ATP-dependent cleavage of mRNA at 21 to 23 nucleotide intervals. Cell 101: 25-33.
132. Bernstein E, Caudy AA, Hammond SM, Hannon GJ (2001) Role for a bidentate ribonuclease in the initiation step of RNA interference. Nature 409: 363-366.
133. Gregory RI, Chendrimada TP, Cooch N, Shiekhattar R (2005) Human RISC couples microRNA biogenesis and posttranscriptional gene silencing. Cell 123: 631-640.
134. Sen GL, Blau HM (2005) Argonaute 2/RISC resides in sites of mammalian mRNA decay known as cytoplasmic bodies. Nat Cell Biol 7: 633-636.
135. Eulalio A, Behm-Ansmant I, Izaurralde E (2007) P bodies: at the crossroads of post-transcriptional pathways. Nat Rev Mol Cell Biol 8: 9-22.
136. Waterhouse PM, Graham MW, Wang MB (1998) Virus resistance and gene silencing in plants can be induced by simultaneous expression of sense and antisense RNA. Proc Natl Acad Sci U S A 95: 13959-13964.
137. Himber C, Dunoyer P, Moissiard G, Ritzenthaler C, Voinnet O (2003) Transitivity-dependent and -independent cell-to-cell movement of RNA silencing. EMBO J 22: 4523-4533.
138. Ulvila J, Parikka M, Kleino A, Sormunen R, Ezekowitz RA, et al. (2006) Double-stranded RNA is internalized by scavenger receptor-mediated endocytosis in Drosophila S2 cells. J Biol Chem 281: 14370-14375.
139. Winston WM, Molodowitch C, Hunter CP (2002) Systemic RNAi in C. elegans requires the putative transmembrane protein SID-1. Science 295: 2456-2459.
140. Feinberg EH, Hunter CP (2003) Transport of dsRNA into cells by the transmembrane protein SID-1. Science 301: 1545-1547.
141. Duxbury MS, Ashley SW, Whang EE (2005) RNA interference: a mammalian SID-1 homologue enhances siRNA uptake and gene silencing efficacy in human cells. Biochem Biophys Res Commun 331: 459-463.
142. Wolfrum C, Shi S, Jayaprakash KN, Jayaraman M, Wang G, et al. (2007) Mechanisms and optimization of in vivo delivery of lipophilic siRNAs. Nat Biotechnol 25: 1149-1157.

143. Saleh MC, van Rij RP, Hekele A, Gillis A, Foley E, et al. (2006) The endocytic pathway mediates cell entry of dsRNA to induce RNAi silencing. Nat Cell Biol 8: 793-802.
144. Hutvagner G, McLachlan J, Pasquinelli AE, Balint E, Tuschl T, et al. (2001) A cellular function for the RNA-interference enzyme Dicer in the maturation of the let-7 small temporal RNA. Science 293: 834-838.
145. Ketting RF, Fischer SE, Bernstein E, Sijen T, Hannon GJ, et al. (2001) Dicer functions in RNA interference and in synthesis of small RNA involved in developmental timing in C. elegans. Genes Dev 15: 2654-2659.
146. Liu J, Carmell MA, Rivas FV, Marsden CG, Thomson JM, et al. (2004) Argonaute2 is the catalytic engine of mammalian RNAi. Science 305: 1437-1441.
147. Vanlandingham PA, Ceresa BP (2009) Rab7 regulates late endocytic trafficking downstream of multivesicular body biogenesis and cargo sequestration. J Biol Chem 284: 12110-12124.
148. van Deurs B, Holm PK, Sandvig K (1996) Inhibition of the vacuolar H(+)-ATPase with bafilomycin reduces delivery of internalized molecules from mature multivesicular endosomes to lysosomes in HEp-2 cells. Eur J Cell Biol 69: 343-350.
149. Stoorvogel W, Kleijmeer MJ, Geuze HJ, Raposo G (2002) The biogenesis and functions of exosomes. Traffic 3: 321-330.
150. Valadi H, Ekstrom K, Bossios A, Sjostrand M, Lee JJ, et al. (2007) Exosome-mediated transfer of mRNAs and microRNAs is a novel mechanism of genetic exchange between cells. Nat Cell Biol 9: 654-659.
151. Pegtel DM, Cosmopoulos K, Thorley-Lawson DA, van Eijndhoven MA, Hopmans ES, et al. (2010) Functional delivery of viral miRNAs via exosomes. Proc Natl Acad Sci U S A 107: 6328-6333.
152. Betz WJ, Mao F, Smith CB (1996) Imaging exocytosis and endocytosis. Curr Opin Neurobiol 6: 365-371.
153. Fischer-Parton S, Parton RM, Hickey PC, Dijksterhuis J, Atkinson HA, et al. (2000) Confocal microscopy of FM4-64 as a tool for analysing endocytosis and vesicle trafficking in living fungal hyphae. J Microsc 198: 246-259.
154. Navaroli DM, Bellve KD, Standley C, Lifshitz LM, Cardia J, et al. (2012) Rabenosyn-5 defines the fate of the transferrin receptor following clathrin-mediated endocytosis. Proc Natl Acad Sci U S A 109: E471-480.
155. Raiborg C, Bremnes B, Mehlum A, Gillooly DJ, D'Arrigo A, et al. (2001) FYVE and coiled-coil domains determine the specific localisation of Hrs to early endosomes. J Cell Sci 114: 2255-2263.
156. Bache KG, Raiborg C, Mehlum A, Stenmark H (2003) STAM and Hrs are subunits of a multivalent ubiquitin-binding complex on early endosomes. J Biol Chem 278: 12513-12521.
157. Peiser L, Mukhopadhyay S, Gordon S (2002) Scavenger receptors in innate immunity. Curr Opin Immunol 14: 123-128.

158. Kujala P, Ikaheimonen A, Ehsani N, Vihinen H, Auvinen P, et al. (2001) Biogenesis of the Semliki Forest virus RNA replication complex. J Virol 75: 3873-3884.
159. Ding SW, Voinnet O (2007) Antiviral immunity directed by small RNAs. Cell 130: 413-426.
160. Livak KJ, Schmittgen TD (2001) Analysis of relative gene expression data using real-time quantitative PCR and the 2(-Delta Delta C(T)) Method. Methods 25: 402-408.
161. Torres GE, Amara SG (2007) Glutamate and monoamine transporters: new visions of form and function. Curr Opin Neurobiol 17: 304-312.
162. Iversen L (2006) Neurotransmitter transporters and their impact on the development of psychopharmacology. Br J Pharmacol 147 Suppl 1: S82-88.
163. Chen R, Tilley MR, Wei H, Zhou F, Zhou FM, et al. (2006) Abolished cocaine reward in mice with a cocaine-insensitive dopamine transporter. Proc Natl Acad Sci U S A 103: 9333-9338.
164. Mazei-Robison MS, Bowton E, Holy M, Schmudermaier M, Freissmuth M, et al. (2008) Anomalous dopamine release associated with a human dopamine transporter coding variant. J Neurosci 28: 7040-7046.
165. Gainetdinov RR, Jones SR, Fumagalli F, Wightman RM, Caron MG (1998) Re-evaluation of the role of the dopamine transporter in dopamine system homeostasis. Brain Res Brain Res Rev 26: 148-153.
166. Jones SR, Gainetdinov RR, Jaber M, Giros B, Wightman RM, et al. (1998) Profound neuronal plasticity in response to inactivation of the dopamine transporter. Proc Natl Acad Sci U S A 95: 4029-4034.
167. Sorkina T, Richards TL, Rao A, Zahniser NR, Sorkin A (2009) Negative regulation of dopamine transporter endocytosis by membrane-proximal N-terminal residues. J Neurosci 29: 1361-1374.
168. Miranda M, Dionne KR, Sorkina T, Sorkin A (2007) Three ubiquitin conjugation sites in the amino terminus of the dopamine transporter mediate protein kinase C-dependent endocytosis of the transporter. Mol Biol Cell 18: 313-323.
169. Bjerggaard C, Fog JU, Hastrup H, Madsen K, Loland CJ, et al. (2004) Surface targeting of the dopamine transporter involves discrete epitopes in the distal C terminus but does not require canonical PDZ domain interactions. J Neurosci 24: 7024-7036.
170. Torres GE, Yao WD, Mohn AR, Quan H, Kim KM, et al. (2001) Functional interaction between monoamine plasma membrane transporters and the synaptic PDZ domain-containing protein PICK1. Neuron 30: 121-134.
171. Carneiro AM, Ingram SL, Beaulieu JM, Sweeney A, Amara SG, et al. (2002) The multiple LIM domain-containing adaptor protein Hic-5 synaptically colocalizes and interacts with the dopamine transporter. J Neurosci 22: 7045-7054.

172. Egana LA, Cuevas RA, Baust TB, Parra LA, Leak RK, et al. (2009) Physical and functional interaction between the dopamine transporter and the synaptic vesicle protein synaptogyrin-3. J Neurosci 29: 4592-4604.
173. Lee CH, Della NG, Chew CE, Zack DJ (1996) Rin, a neuron-specific and calmodulin-binding small G-protein, and Rit define a novel subfamily of ras proteins. J Neurosci 16: 6784-6794.
174. Heo WD, Inoue T, Park WS, Kim ML, Park BO, et al. (2006) PI(3,4,5)P3 and PI(4,5)P2 lipids target proteins with polybasic clusters to the plasma membrane. Science 314: 1458-1461.
175. Adkins EM, Samuvel DJ, Fog JU, Eriksen J, Jayanthi LD, et al. (2007) Membrane mobility and microdomain association of the dopamine transporter studied with fluorescence correlation spectroscopy and fluorescence recovery after photobleaching. Biochemistry 46: 10484-10497.
176. Cremona ML, Matthies HJ, Pau K, Bowton E, Speed N, et al. (2011) Flotillin-1 is essential for PKC-triggered endocytosis and membrane microdomain localization of DAT. Nat Neurosci 14: 469-477.
177. Foster JD, Adkins SD, Lever JR, Vaughan RA (2008) Phorbol ester induced trafficking-independent regulation and enhanced phosphorylation of the dopamine transporter associated with membrane rafts and cholesterol. J Neurochem 105: 1683-1699.
178. Sandvig K, van Deurs B (2000) Entry of ricin and Shiga toxin into cells: molecular mechanisms and medical perspectives. EMBO J 19: 5943-5950.
179. Xia Z, Liu Y (2001) Reliable and global measurement of fluorescence resonance energy transfer using fluorescence microscopes. Biophys J 81: 2395-2402.
180. Feige JN, Sage D, Wahli W, Desvergne B, Gelman L (2005) PixFRET, an ImageJ plug-in for FRET calculation that can accommodate variations in spectral bleed-throughs. Microsc Res Tech 68: 51-58.
181. Bartholomaus I, Milan-Lobo L, Nicke A, Dutertre S, Hastrup H, et al. (2008) Glycine transporter dimers: evidence for occurrence in the plasma membrane. J Biol Chem 283: 10978-10991.
182. Hastrup H, Karlin A, Javitch JA (2001) Symmetrical dimer of the human dopamine transporter revealed by cross-linking Cys-306 at the extracellular end of the sixth transmembrane segment. Proc Natl Acad Sci U S A 98: 10055-10060.
183. Miranda M, Sorkina T, Grammatopoulos TN, Zawada WM, Sorkin A (2004) Multiple molecular determinants in the carboxyl terminus regulate dopamine transporter export from endoplasmic reticulum. J Biol Chem 279: 30760-30770.
184. Sorkina T, Doolen S, Galperin E, Zahniser NR, Sorkin A (2003) Oligomerization of dopamine transporters visualized in living cells by

fluorescence resonance energy transfer microscopy. J Biol Chem 278: 28274-28283.
185. Alvarez E, Girones N, Davis RJ (1989) Intermolecular disulfide bonds are not required for the expression of the dimeric state and functional activity of the transferrin receptor. EMBO J 8: 2231-2240.
186. Wes PD, Yu M, Montell C (1996) RIC, a calmodulin-binding Ras-like GTPase. EMBO J 15: 5839-5848.
187. Zhou Q, Li J, Wang H, Yin Y, Zhou J (2011) Identification of nigral dopaminergic neuron-enriched genes in adult rats. Neurobiol Aging 32: 313-326.
188. Glessner JT, Reilly MP, Kim CE, Takahashi N, Albano A, et al. (2010) Strong synaptic transmission impact by copy number variations in schizophrenia. Proc Natl Acad Sci U S A 107: 10584-10589.
189. Bouquillon S, Andrieux J, Landais E, Duban-Bedu B, Boidein F, et al. (2011) A 5.3Mb deletion in chromosome 18q12.3 as the smallest region of overlap in two patients with expressive speech delay. Eur J Med Genet 54: 194-197.
190. Balklava Z, Pant S, Fares H, Grant BD (2007) Genome-wide analysis identifies a general requirement for polarity proteins in endocytic traffic. Nat Cell Biol 9: 1066-1073.
191. Leibfried A, Fricke R, Morgan MJ, Bogdan S, Bellaiche Y (2008) Drosophila Cip4 and WASp define a branch of the Cdc42-Par6-aPKC pathway regulating E-cadherin endocytosis. Curr Biol 18: 1639-1648.
192. Lein PJ, Guo X, Shi GX, Moholt-Siebert M, Bruun D, et al. (2007) The novel GTPase Rit differentially regulates axonal and dendritic growth. J Neurosci 27: 4725-4736.
193. Spencer ML, Shao H, Andres DA (2002) Induction of neurite extension and survival in pheochromocytoma cells by the Rit GTPase. J Biol Chem 277: 20160-20168.
194. Spencer ML, Shao H, Tucker HM, Andres DA (2002) Nerve growth factor-dependent activation of the small GTPase Rin. J Biol Chem 277: 17605-17615.
195. Shi GX, Han J, Andres DA (2005) Rin GTPase couples nerve growth factor signaling to p38 and b-Raf/ERK pathways to promote neuronal differentiation. J Biol Chem 280: 37599-37609.
196. Bolan EA, Kivell B, Jaligam V, Oz M, Jayanthi LD, et al. (2007) D2 receptors regulate dopamine transporter function via an extracellular signal-regulated kinases 1 and 2-dependent and phosphoinositide 3 kinase-independent mechanism. Mol Pharmacol 71: 1222-1232.
197. Moron JA, Zakharova I, Ferrer JV, Merrill GA, Hope B, et al. (2003) Mitogen-activated protein kinase regulates dopamine transporter surface expression and dopamine transport capacity. J Neurosci 23: 8480-8488.

198. Zapata A, Kivell B, Han Y, Javitch JA, Bolan EA, et al. (2007) Regulation of dopamine transporter function and cell surface expression by D3 dopamine receptors. J Biol Chem 282: 35842-35854.
199. Andres DA, Rudolph JL, Sengoku T, Shi GX (2006) Analysis of Rit signaling and biological activity. Methods Enzymol 407: 499-512.
200. Shipitsin M, Feig LA (2004) RalA but not RalB enhances polarized delivery of membrane proteins to the basolateral surface of epithelial cells. Mol Cell Biol 24: 5746-5756.
201. Goody RS, Rak A, Alexandrov K (2005) The structural and mechanistic basis for recycling of Rab proteins between membrane compartments. Cell Mol Life Sci 62: 1657-1670.
202. Chen R, Furman CA, Zhang M, Kim MN, Gereau RWt, et al. (2009) Protein kinase Cbeta is a critical regulator of dopamine transporter trafficking and regulates the behavioral response to amphetamine in mice. J Pharmacol Exp Ther 328: 912-920.
203. Doolen S, Zahniser NR (2002) Conventional protein kinase C isoforms regulate human dopamine transporter activity in Xenopus oocytes. FEBS Lett 516: 187-190.
204. Prasad HC, Steiner JA, Sutcliffe JS, Blakely RD (2009) Enhanced activity of human serotonin transporter variants associated with autism. Philos Trans R Soc Lond B Biol Sci 364: 163-173.
205. Melikian HE, Buckley KM (1999) Membrane trafficking regulates the activity of the human dopamine transporter. J Neurosci 19: 7699-7710.
206. Schmid JA, Sitte HH (2003) Fluorescence resonance energy transfer in the study of cancer pathways. Curr Opin Oncol 15: 55-64.
207. Sucic S, Dallinger S, Zdrazil B, Weissensteiner R, Jorgensen TN, et al. (2010) The N terminus of monoamine transporters is a lever required for the action of amphetamines. J Biol Chem 285: 10924-10938.
208. Hein P, Frank M, Hoffmann C, Lohse MJ, Bunemann M (2005) Dynamics of receptor/G protein coupling in living cells. EMBO J 24: 4106-4114.
209. Just H, Sitte HH, Schmid JA, Freissmuth M, Kudlacek O (2004) Identification of an additional interaction domain in transmembrane domains 11 and 12 that supports oligomer formation in the human serotonin transporter. J Biol Chem 279: 6650-6657.
210. Birnbaum MJ (1992) The insulin-sensitive glucose transporter. Int Rev Cytol 137: 239-297.
211. Zaid H, Antonescu CN, Randhawa VK, Klip A (2008) Insulin action on glucose transporters through molecular switches, tracks and tethers. Biochem J 413: 201-215.
212. Charron MJ, Brosius FC, 3rd, Alper SL, Lodish HF (1989) A glucose transport protein expressed predominately in insulin-responsive tissues. Proc Natl Acad Sci U S A 86: 2535-2539.

213. Watson RT, Kanzaki M, Pessin JE (2004) Regulated membrane trafficking of the insulin-responsive glucose transporter 4 in adipocytes. Endocr Rev 25: 177-204.
214. Guilherme A, Soriano NA, Furcinitti PS, Czech MP (2004) Role of EHD1 and EHBP1 in perinuclear sorting and insulin-regulated GLUT4 recycling in 3T3-L1 adipocytes. J Biol Chem 279: 40062-40075.
215. Marsh EW, Leopold PL, Jones NL, Maxfield FR (1995) Oligomerized transferrin receptors are selectively retained by a lumenal sorting signal in a long-lived endocytic recycling compartment. J Cell Biol 129: 1509-1522.
216. St Pierre CA, Leonard D, Corvera S, Kurt-Jones EA, Finberg RW (2011) Antibodies to cell surface proteins redirect intracellular trafficking pathways. Exp Mol Pathol 91: 723-732.
217. Rotem-Yehudar R, Galperin E, Horowitz M (2001) Association of insulin-like growth factor 1 receptor with EHD1 and SNAP29. J Biol Chem 276: 33054-33060.
218. Caplan S, Naslavsky N, Hartnell LM, Lodge R, Polishchuk RS, et al. (2002) A tubular EHD1-containing compartment involved in the recycling of major histocompatibility complex class I molecules to the plasma membrane. EMBO J 21: 2557-2567.
219. Beckman ML, Quick MW (1998) Neurotransmitter transporters: regulators of function and functional regulation. J Membr Biol 164: 1-10.
220. Amara SG, Sonders MS (1998) Neurotransmitter transporters as molecular targets for addictive drugs. Drug Alcohol Depend 51: 87-96.
221. Blakely RD (2001) Physiological genomics of antidepressant targets: keeping the periphery in mind. J Neurosci 21: 8319-8323.
222. Robertson SD, Matthies HJ, Galli A (2009) A closer look at amphetamine-induced reverse transport and trafficking of the dopamine and norepinephrine transporters. Mol Neurobiol 39: 73-80.
223. Jayanthi LD, Ramamoorthy S (2005) Regulation of monoamine transporters: influence of psychostimulants and therapeutic antidepressants. AAPS J 7: E728-738.
224. Zahniser NR, Sorkin A (2004) Rapid regulation of the dopamine transporter: role in stimulant addiction? Neuropharmacology 47 Suppl 1: 80-91.
225. Puthenveedu MA, von Zastrow M (2006) Cargo regulates clathrin-coated pit dynamics. Cell 127: 113-124.
226. Eriksen J, Rasmussen SG, Rasmussen TN, Vaegter CB, Cha JH, et al. (2009) Visualization of dopamine transporter trafficking in live neurons by use of fluorescent cocaine analogs. J Neurosci 29: 6794-6808.
227. Daws LC, Callaghan PD, Moron JA, Kahlig KM, Shippenberg TS, et al. (2002) Cocaine increases dopamine uptake and cell surface expression of dopamine transporters. Biochem Biophys Res Commun 290: 1545-1550.
228. Little KY, Elmer LW, Zhong H, Scheys JO, Zhang L (2002) Cocaine induction of dopamine transporter trafficking to the plasma membrane. Mol Pharmacol 61: 436-445.

229. Adams SR, Tsien RY (2008) Preparation of the membrane-permeant biarsenicals FlAsH-EDT2 and ReAsH-EDT2 for fluorescent labeling of tetracysteine-tagged proteins. Nat Protoc 3: 1527-1534.
230. Bhunia AK, Miller SC (2007) Labeling tetracysteine-tagged proteins with a SplAsH of color: a modular approach to bis-arsenical fluorophores. Chembiochem 8: 1642-1645.
231. Adams SR, Campbell RE, Gross LA, Martin BR, Walkup GK, et al. (2002) New biarsenical ligands and tetracysteine motifs for protein labeling in vitro and in vivo: synthesis and biological applications. J Am Chem Soc 124: 6063-6076.
232. Orun O, Rasmussen S, Gether U (2009) Introducing tetraCys motifs at two different sites results in a functional dopamine transporter. Acta Biol Hung 60: 15-25.
233. Vaughan RA, Huff RA, Uhl GR, Kuhar MJ (1997) Protein kinase C-mediated phosphorylation and functional regulation of dopamine transporters in striatal synaptosomes. J Biol Chem 272: 15541-15546.
234. Machleidt T, Robers M, Hanson GT (2007) Protein labeling with FlAsH and ReAsH. Methods Mol Biol 356: 209-220.
235. Taguchi Y, Shi ZD, Ruddy B, Dorward DW, Greene L, et al. (2009) Specific biarsenical labeling of cell surface proteins allows fluorescent- and biotin-tagging of amyloid precursor protein and prion proteins. Mol Biol Cell 20: 233-244.
236. Hearps AC, Pryor MJ, Kuusisto HV, Rawlinson SM, Piller SC, et al. (2007) The biarsenical dye Lumio exhibits a reduced ability to specifically detect tetracysteine-containing proteins within live cells. J Fluoresc 17: 593-597.
237. Hastrup H, Sen N, Javitch JA (2003) The human dopamine transporter forms a tetramer in the plasma membrane: cross-linking of a cysteine in the fourth transmembrane segment is sensitive to cocaine analogs. J Biol Chem 278: 45045-45048.

APPENDIX

INSERTION OF TETRACYSTEINE MOTIFS INTO DOPAMINE TRANSPORTER EXTRACELLULAR DOMAINS

ABSTRACT

The neuronal dopamine transporter (DAT) is a major determinant of extracellular dopamine (DA) levels and is the primary target for a variety of addictive and therapeutic psychoactive drugs. DAT is acutely regulated by protein kinase C (PKC) activation and amphetamine exposure, both of which modulate DAT surface expression by endocytic trafficking. In order to use live imaging approaches to study DAT endocytosis, methods are needed to exclusively label the DAT surface pool. The use of membrane impermeant, sulfonated biarsenic dyes holds potential as one such approach, and requires introduction of an extracellular tetracysteine motif (tetraCys; CCPGCC) to facilitate dye binding. In the current study, we took advantage of intrinsic proline-glycine (Pro-Gly) dipeptides encoded in predicted DAT extracellular domains to introduce tetraCys motifs into DAT extracellular loops 2, 3, and 4. [^{3}H]DA uptake studies, surface biotinylation and fluorescence microscopy in PC12 cells indicate that tetraCys insertion into the DAT second extracellular loop results in a functional transporter that maintains PKC-mediated downregulation. Introduction of tetraCys into extracellular loops 3 and 4 yielded DATs with severely

compromised function that failed to mature and traffic to the cell surface. This is the first demonstration of successful introduction of a tetracysteine motif into a DAT extracellular domain, and may hold promise for use of biarsenic dyes in live DAT imaging studies.

INTRODUCTION

DA reuptake mediated by DAT is the primary means for clearing synaptic DA and terminating dopaminergic neurotransmission [82,219]. DAT is member of the Na^+/Cl^- -dependent SLC6 symporter gene family and is potently inhibited by addictive psychostimulants, such as amphetamine and cocaine, as well as by therapeutic agents such as the NDRI class of antidepressants and methylphenidate (Ritalin) [220-222]. Transgenic mouse studies indicate that DAT is critical in maintaining normal dopaminergic neurotransmission and synaptic tone, and that even a 50% reduction in DAT protein (DAT +/− mice) is sufficient to significantly alter DA signaling and synaptic stores [165,166]. Thus, cellular mechanisms that modulate DAT cell surface expression are likely to have a significant impact on DA availability and signaling in the brain.

DAT is acutely downregulated by PKC activation [87,88] and amphetamine exposure [89,223,224], which markedly decrease DAT surface levels via endosomal trafficking. While it is well established DAT surface levels are modulated by endocytic trafficking, the cellular mechanisms that mediate DAT trafficking are not well defined. Live cellular imaging is a highly effective

means to reveal cellular trafficking mechanisms that are not detectable by fixed cell imaging or biochemical approaches [49,225]. Recent studies using GFP-tagged DAT [27] and fluorescently-labeled cocaine analogs [226] have proved successful in achieving live DAT trafficking images; however, each approach has inherent limitations. GFP-tagged DAT may not behave identically to the wildtype DAT, and has the disadvantage of labeling the entire cellular DAT population, limiting the ability to examine DAT surface dynamics specifically. Use of cocaine analogs allows for exclusive labeling of the DAT surface pool, but may not reflect native DAT trafficking as cocaine binding has itself been reported to alter DAT surface expression [227,228].

The use of biarsenic dyes, such as FlAsH, ReAsH [229] and SplAsH [230], is another potential means to fluorescently label proteins for live imaging. In particular, sulfonated versions of these dyes are membrane impermeant and may be suitable to exclusively label surface proteins [231]. Biarsenic dyes are not fluorescent in solution and bind with high affinity to tetracysteine (tetraCys) motifs, preferably flanking a proline-glycine (Pro-Gly) dipeptide (CCPGCC) [231]. Upon binding, they become highly fluorescent. In the current study, we engineered tetraCys motifs flanking existing extracellular Pro-Gly dipeptide residues encoded in human DAT (hDAT) at amino acid positions 194, 288 and 387, to use as potential biarsenic dye labeling sites. Analysis of these DAT mutants reveals that inserting a tetraCys site into DAT extracellular loop 2 (EL2) is well tolerated by DAT, and yields a functional transporter that retains sensitivity

to PKC activation, whereas insertion of tetraCys into either extracellular loop 3 or 4 (EL3, EL4) perturbs DAT biosynthesis and trafficking to the cell surface.

RESULTS

Protein labeling with biarsenic dyes requires the presence of a tetraCys motif, optimally flanking a Pro-Gly dipeptide. As depicted in Figure A.1, DAT encodes three predicted extracellular Pro-Gly sequences at residues 194, 288 and 387. We took advantage of these intrinsic Pro-Gly residues and mutated the 2 upstream and downstream residues to cysteines to generate three DAT constructs with CCPGCC sequences in either extracellular loops 2, 3 or 4 (termed DAT EL2-CCPGCC, EL3-CCPGCC and EL4-CCPGCC, respectively). We first tested whether the mutant DATs retained DA transport function as compared to wildtype DAT. As seen in Figure A.2A, all three tetraCys mutants exhibited significantly reduced DA uptake as compared to wildtype DAT ($p<.01$). However, DAT-EL2-CCPGCC retained 63.5% of wildtype activity, which was significantly greater than both DAT-EL3-CCPGCC and DAT-EL4-CCPGCC ($p<.001$). We next tested whether any of the DAT tetraCys mutants were capable of undergoing PKC-mediated downregulation. Following treatment with 100 nM PMA, 30′, 37°C, wildtype DAT function decreased by 30.7±2.3% (Figure A.2B). Similarly, PKC activation decreased DAT-EL2-CCPGCC activity by 29% (Not significantly different from wild type, $p = 0.77$, Student's t test, $n = 3$). In contrast, PKC activation had no effect on either DAT-EL3-CCPGCC or DAT-EL4-

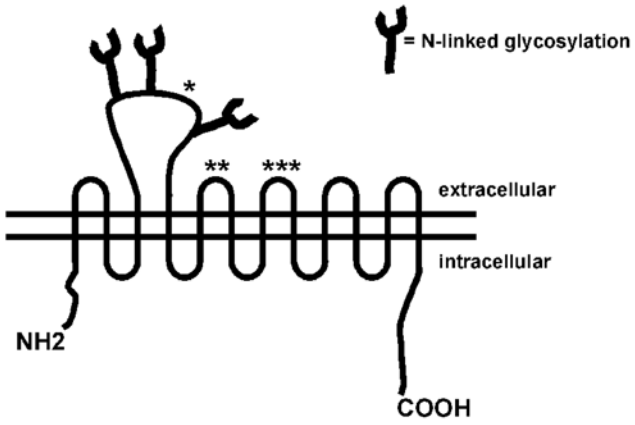

*EL2	189	CSDAHPGDSSGD	200
**EL3	283	RGVTLPGAIDGI	294
***EL4	382	VAKDGPGLIFII	393

Figure A.1. Schematic of DAT with target sites for tetracysteine mutagenesis. *Top*: DAT model. Asterisk indicate extracellular Pro-Gly residues targeted for tetracysteine mutagenesis. *Bottom*: DAT sequences spanning across the Pro-Gly tetracysteine target sites. Pro-Gly dipeptides are highlighted in the shaded boxes.

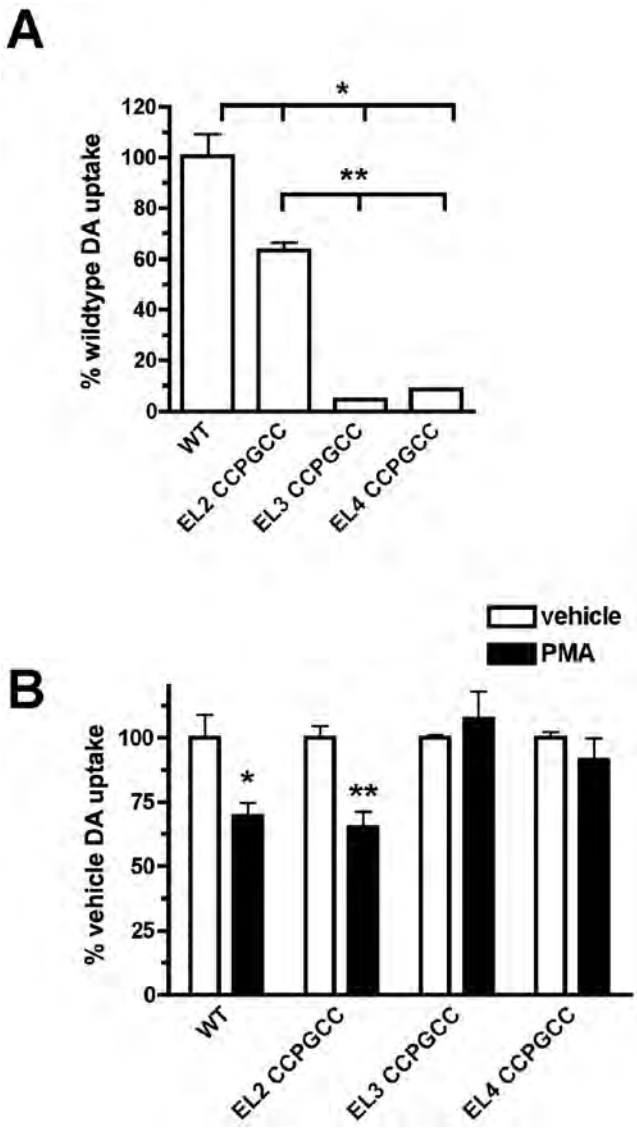

Figure A.2. DA uptake and PKC-mediated down-regulation are preserved when a tetracysteine motif is introduced into EL2, but not EL3 or EL4. *DA uptake assay*. Cells were transfected as described in *Experimental Procedures* and [^{3}H]DA uptake was assessed 48 hours post transfection. **A.** Introduction of tetracysteine motifs decreases DA uptake. Data are expressed as % wild-type activity +/_ S.E.M. *Significantly different from wild-type ($p<0.1$, One-way ANOVA with Tukey's multiple comparison test, n=3), **Significantly different from EL2-CCPGCC DAT ($p<0.001$, One-way ANOVA with Tukey's multiple comparison test, n=3). **B.** EL2-CC{GCC DAT is acutely downregulated by PKC activation, whereas EL3- and EL4-CCPGCC are not. Cells were treated with either vehicle or 100nM PMA, 30 min, 37°C and [^{3}H]DA uptake was measured. Data are expressed as % vehicle-treated DA uptake +/-S.E.M. for each construct. *Significantly different from vehicle treated ($p<0.05$, Student's t test, n=3), **Significantly different from vehicle treated ($p<0.02$, Student's t test, n=3).

CCPGCC (Figure A.2B). These data suggest that introduction of a tetraCys motif into the DAT EL2 results in a functional DAT that undergoes PKC-mediated downregulation, whereas conversion of residues in EL3 and EL4 is not well tolerated by DAT.

We next used cell surface biotinylation to test whether the tetracysteine DATs exhibited maturation and cell surface expression comparable to wildtype DAT. As seen in Figure A.3A, surface and intracellular proteins are readily detectable for both wildtype and EL2-CCPGCC DATs, and no significant difference between the %total mature DAT on the cell surface was detected (Figure A.3B, 48.1±6.7% (wildtype) vs. 49.0±5.4% (EL2-CCPGCC), p = .92, Student's *t* test, n = 4). In contrast, neither EL3 nor EL4 were detected at the cell surface, nor was any mature protein detected, suggesting that these mutants fail to progress through the biosynthetic pathway (Figure A.3C). We also measured the ratios of mature (90 kDa) to immature (56 kDa) DAT as an index of how readily EL2-CCPGCC DAT progresses through the biosynthetic pathway. Wildtype DAT exhibited mature:immature protein ratio of 1.66±0.22, whereas EL2-CCPGCC DAT had a trend for less mature:immature protein (0.99±.17), but which was not significantly different from wildtype (p = .07, Student's t test, n = 4), suggesting that EL2-CCPGCC DAT is processed through the biosynthetic pathway comparably to wildtype DAT.

We next used fluorescence microscopy to examine the cellular distribution of the tetracysteine-tagged DATs as compared to wildtype DAT in transiently

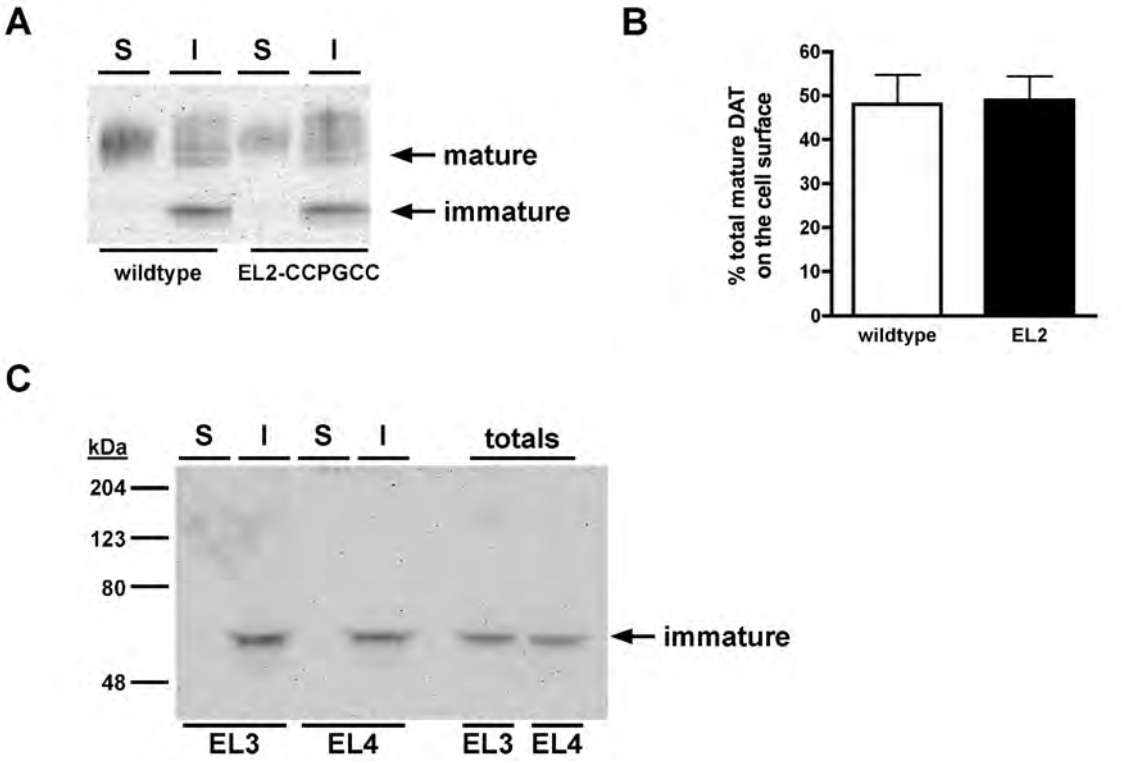

Figure A.3. The presence of a tetracysteine in DAT EL2 does not alter DAT maturation or surface expression. *Surface biotinylation assay*. Cells were transfected with the indicated DAT constructs and cell surface proteins were biotinylated and isolated from intracellular proteins as described in *Experimental Procedures*. **A.** Representative immunoblot displaying surface (S) and intracellular (I) wild-type and EL2-CCPGCC DAT. Mature (90 kDa) and immature (56 kDa) species are indicated. **B.** Averaged data. Data are expressed as % total mature DAT on cell surface +/-S.E.M. (n=4). **C.** Representative immunoblot displaying surface (S) and intracellular (I) EL3-CCPGCC and EL4-CC{GCC DAT. Total lysates are displayed in the far right hand lanes. Note that no mature protein is detected. Immature species (56 kDa) are indicated.

transfected PC12 cells. Wildtype DAT staining presented as an intense ring at the cell perimeter, and PKC activation resulted in robust DAT redistribution to intracellular puncta (Figure A.4A). Similarly, EL2-CCPGCC DAT staining was primarily at the cell perimeter (Figure A.4A), although some intracellular staining was apparent. Moreover, PKC activation resulted in pronounced surface losses of EL2-CCPGCC DAT, similar to that observed for wildtype and consistent with our uptake results demonstrating functional downregulation of EL2-CCPGCC DAT. We also expressed EL3, EL4 mutants and visualized their cellular distribution. Neither EL3 nor EL4 were present at the cell perimeter, and a diffuse perinuclear signal was detected (Figure A.4B). These results are consistent with our uptake and surface biotinylation results suggesting that EL3 and EL4 fail to mature and traffic to the cell surface and that these mutations are not well tolerated by DAT.

DISCUSSION

In the current study, we aimed to introduce tetraCys residues in DAT extracellular domains that intrinsically encode Pro-Gly dipeptide sequences at DAT amino acid positions 194, 288 and 387. The CCPGCC sequence is the optimal sequence to facilitate biarsenic dye binding, and once bound confers the proper dye conformation for fluorescence emission [229,231]. Converting the four residues flanking the Pro-Gly at amino acid positions 194–195 yielded a DAT that retained DAT surface expression comparable to wildtype. Moreover,

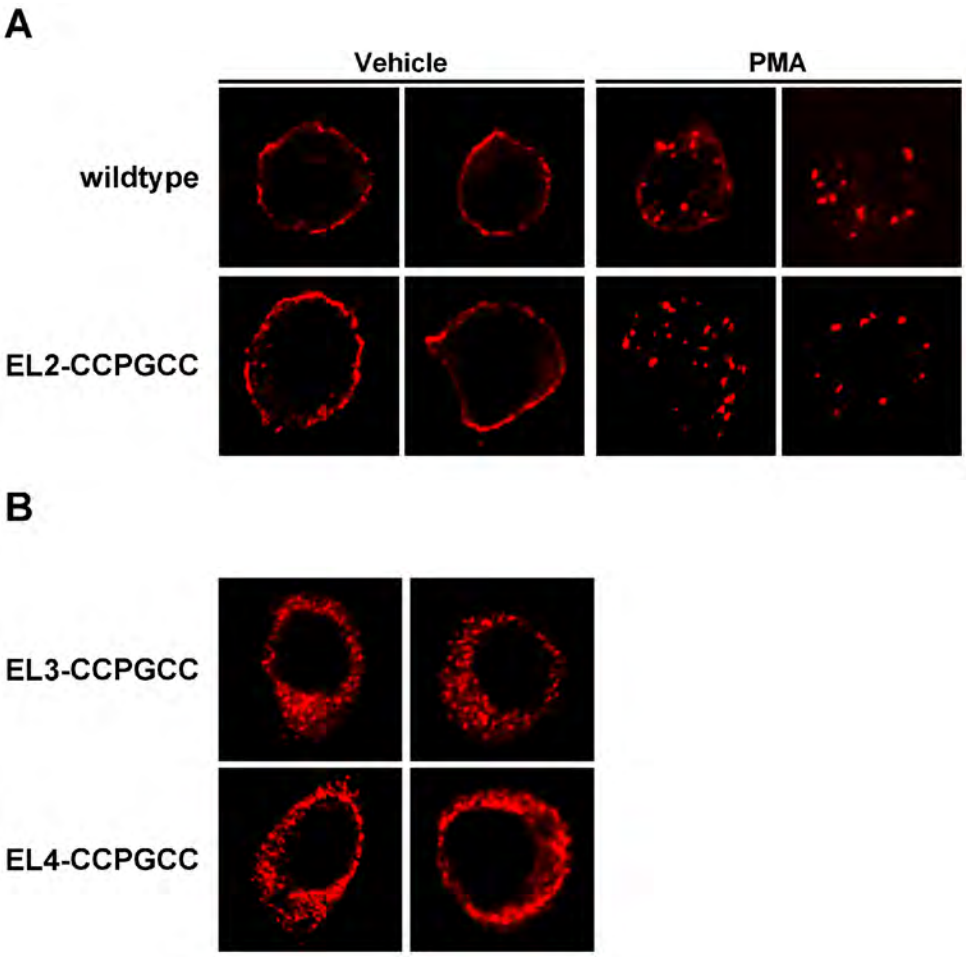

Figure A.4. Cellular distribution of tetracysteine mutant DATs. EL2-CCPGCC DAT is robustly expressed at the cell surface and internalizes in response to PKC activation. *Immunofluorescence microscopy*. Cells were transfected with the indicated constructs and were fixed and stained with rat anti-DAT antibodies as described in *Experimental Procedures*. A representative panel of deconvolved images is presented. A single plane through each cell center is shown. **A.** Effect of PKC activation on EL2-CCPGCC DAT. Prior to fixation, cells were treated with either vehicle or 1µM PMA (37°C, 30min). **B.** Cellular distribution of EL3-CCPGCC and EL4-CCPGCC DAT. Note the lack of either protein at the cell surface.

EL2-CCPGCC DAT exhibit robust DA uptake, albeit somewhat reduced as compared to wildtype, and retained sensitivity to PKC-mediated downregulation, suggesting that this mutant may be amenable to labeling with biarsenic dyes for live imaging studies of DAT trafficking. A recent study indicated that inserting a tetraCys motif at the DAT amino terminus and at position 511 were also well tolerated [232]. However, these are both located on intracellular domains that would require use of a membrane permeant biarsenic dye that would have access to the entire cellular DAT population and would not exclusively label the DAT surface residents. It is also interesting to note that although we reproducibly observe PKC-mediated DAT downregulation in PC12 cells, a recent study by Ericksen *et al* reports lack of PKC-mediated downregulation in primary ventral midbrain neurons prepared from P2 rat pups [226]. This conflicts with previous studies that report PKC-mediated DAT downregulation in adult rat striatal synaptosomes [233], and suggests that either the developmental stage of the dopaminergic neuron or the primary culture environment may influence the ability of DAT to undergo PKC-mediated downregulation.

While our data demonstrate that an extracellular tetracysteine-tag is well tolerated by DAT, they do not demonstrate whether this DAT construct can be labeled with biarsenic dyes. We made several attempts to label EL2-CCPGCC DAT using Lumio brand (Invitrogen) FlAsH reagent, using both standard approaches as well as modified protocols that use extended washes with BAL reagent to reduce non-specific FlAsH binding. All of our labeling attempts

resulted in a high degree of non-specific labeling of non-transfected cells, as well as cells expressing either wildtype or EL2-CCPGCC DAT (not shown). Problems with non-specific FlAsH binding have been described [234,235] and particular issues have been raised regarding the utility and specificity of the commercially available Lumio form of FlAsH [236]. Thus, while our EL2-CCPGCC DAT is a viable DAT form, advances in FlAsH labeling may be required in order to determine the utility of this mutant in future trafficking studies.

DAT residues 192–197 are located between the second and third glycosylation sites of the large second extracellular loop of the protein. This region appears to tolerate amino acid substitution well, as previous studies reported that an extracellular HA epitope was successfully engineered across residues 193–203 [86]. The HA epitope at this locus is accessible for extracellular antibody labeling, suggesting that the much smaller biarsenic dye would also have access to this DAT region. Cysteine conversion of EL3 and EL4 residues flanking the Pro-Gly at positions 288–289 and 387–388, respectively, yielded CCPGCC DAT mutants that were not highly functional. Interestingly, a previous mutagenesis study in which a cysteine-depleted DAT was generated indicated that mutating an existing cysteine in EL3 at position 306, just downstream of the EL3-CCPGCC DAT, resulted in the expression of mature DAT protein [237] that is fully functional [182]. Cys306 is positioned close to the sixth transmembrane segment, suggesting that this region may be more tolerable to structural perturbation.

In summary, we have characterized a functional DAT mutant that encodes a tetraCys motif on the extracellular DAT domain EL2. The ability to introduce cysteines at this locus may have future utility both for NTSEA reagent labeling, as well as for biarsenic dye labeling for live imaging studies. Future studies will directly examine the capacity of this mutant to bind to biarsenic dyes.

EXPERIMENTAL PROCEDURES

Constructs and Mutagenesis - TetraCys motifs flanking existing extracellular Pro-Gly residues were engineered into EL2, EL3 or EL4 DAT extracellular loops by mutating the two residues upstream and downstream of the Pro-Gly residues into cysteines. The amino acids mutated to cysteines were: EL2: 192–193/196–197; EL3: 286–287/290–291; EL4 385–386/389–390. hDAT pcDNA3.1(+) was mutated using the QuikChange Mutagenesis kit (Stratagene). The following mutagenic primers spanning the indicated hDAT cDNA regions were used:

EL2-CCPGCC (577–627)

5′CCCCAACTGCTCGGATTGCTGTCCTGGTTGCTGCAGTG
GAGACAGCTCGG3′ (sense),

5′CCGAGCTGTCTCCACTGCAGCAACCAGGACAGCAATCC
GAGCAGTTGGGG3′(antisense);

EL3-CCPGCC (860–907)

5′CTCCTGCGTGGGGTCTGCTGCCCTGGATGCTGTGACGG
CATCAGAGCA3′ (sense),

5′TGCTCTGATGCCGTCACAGCATCCAGGGCAGCAGACCC

CACGCAGGAG3′(antisense);

EL4-CCPGCC (1156–1205)

5′ CGGGGACGTGGCCAAGTGCTGCCCAGGGTGCTGCTTCATC

ATCTACCCGG3′ (sense),

5′CCGGGTAGATGATGAAGCAGCACCCTGGGCAGCACTTG

GCCACGTCCCCG3′(antisense).

Mutations were confirmed by sequencing (UMASS Medical School Nucleic Acid Facility) and mutagenic regions were subcloned back into the parental hDAT cDNA using the following restriction enzymes: PflMI/BstEII (EL2-CCPGCC), PflMI/ClaI (EL3-CCPGCC), BstEII/ClaI (EL4-CCPGCC).

Cell culture and transfection - PC12 cells were from ATCC as previously described [205] and were cultured at 10% CO_2 in high glucose DMEM supplemented with 5% horse serum, 5% bovine calf serum, 2 mM glutamine and 10^2 U/ml penicillin-streptomycin. Cells were removed from the cultureware by spraying media directly onto the growth surface and triturating. Cells were transiently transfected either with Lipofectamine 2000 (Invitrogen), according to the manufacture's instructions, or by electroporation as previously described [90]. Briefly, 1.2×10^7 cells were collected by centrifugation and resuspended in 0.75 ml electroporation buffer (137 mM NaCl, 5.0 mM KCl, 0.7 mM Na_2HPO_4, 6.0 mM glucose, 20 mM HEPES, pH 7.05) and were mixed with 18.2 µg of the indicated

plasmids. Cells were electroporated at 300 mV, 500 µF, with an exponential decay protocol, using a GenePulser Xcell unit (Biorad, Hercules, CA) with a CE module and 4.0 mm cuvettes. Following 30 min recovery in PC12 media containing 3 mM EGTA, cells were plated onto poly-D-lysine coated plates as indicated. All transfected cells were assayed 48 hrs post-transfection.

Surface Biotinylation and Immunoblotting - Cells were seeded in 6 well plates coated with 0.5 mg/ml poly-D-lysine 48 hours prior to performing assays. For surface biotinylation, cells were washed with phosphate buffered saline supplemented with 1.5 mM $MgCl_2$, 0.2 mM $CaCl_2$ (PBS^{2+}) and surface proteins were covalently labeled biotin by incubating 2×15 min, 4°C with freshly prepared 1.0 mg/ml sulfo-NHS-SS-biotin (Pierce) prepared in PBS^{2+}. Residual biotinylation reagent was quenched by washing cells with and incubating 2×15′, 4°C in PBS^{2+}, 100 mM glycine. Cells were lysed in RIPA buffer (10 mM Tris, pH 7.4, 150 mM NaCl, 1.0 mM EDTA, 0.1% SDS, 1.0% Triton X 100, 1.0% sodium deoxycholate) containing protease inhibitors (1.0 mM PMSF, 1.0 µg/ml each leupeptin, aprotinin and pepstatin), 20 min, 4°C, cellular debris was cleared by centrifugation and protein concentrations were determined with the BCA protein assay (Pierce). Surface (biotinylated) proteins were separated from intracellular (non-biotinylated) proteins by streptavidin batch affinity chromatography using streptavidin-coupled agarose beads (Pierce), incubating overnight, 4°C with rotation. Non-biotinylated proteins in the supernatants were removed and

concentrated by spin filtration using columns with 30 kDa molecular weight cutoff (Millipore). Beads bound to biotinylated proteins were washed three times with RIPA buffer and bound proteins were eluted in 2x Laemmli sample buffer by rotating 30 min, 25°C. Samples were separated on 10% SDS-PAGE gels and were transferred onto nitrocellulose for 1 hour, 100 V, 4°C. Blots were blocked with 5% nonfat dry milk in PBS/0.1% Tween-20 (PBS-T), 45 min, 25°C, and incubated with rat anti-DAT antibody (MAB369, Chemicon, 1:1000) overnight, 4°C. Blots were washed with PBS-T and incubated with HRP-conjugated goat anti-rat antibody (Santa Cruz, 1:5000), 45′, 25°C, following by washing in PBS-T. Blots were developed with Supersignal Dura (Pierce) and immunoreactive bands were detected with a VersaDoc imaging station (Bio-Rad). Non-saturating bands were quantified using Quantity One software and results were analyzed using GraphPad Prism software. Mature:immature protein ratios were calculated by summing mature band (90 kDa) densities in surface and intracellular fractions, and dividing by the immature band (56 kDa) density in the intracellular fraction.

Immunocytochemistry and Microscopy - Transfected cells were seeded on glass coverslips coated with 1.0 mg/ml poly-D-lysine 48 hours prior to fixation and labeling. Cells were treated as indicated, rinsed in PBS and fixed in 4% paraformaldehyde prepared in PBS, 10 min, 25°C. Cells were blocked and permeabilized by incubating in blocking solution (PBS, 1% IgG/Protease-free BSA, 5% goat serum, 0.2% Triton-X-100), 30′, 25°C, followed by incubation with

rat anti-DAT antibody (1:2000 in blocking solution), 45 min, 25°C. Cells were washed with PBS and incubated with Alexa594-conjugated goat anti-rat antibody (1:5000, Molecular Probes), 45 min, 25°C. Cells were washed with PBS, dried and mounted on glass slides with ProLong Gold (Molecular Probes). Immunoreactive cells were visualized as previously described [91] with a Zeiss Axiovert 200 M microscope using a 63X, 1.4 N.A. oil immersion objective and 0.4 µm optical sections were captured through the z-axis with a Retiga-1300R cooled CCD camera (Qimaging) using Slidebook 4.0 software (Intelligent Imaging Innovations). Z- stacks were deconvolved with a constrained iterative algorithm using measured point spread functions for each fluorescent channel using Slidebook 4.0 software. All images shown are single 0.4 µm planes through the center of each cell.

(^{3}H)DA Uptake Assays - Transfected cells were seeded onto 24 well plates coated with 0.5 mg/ml poly-D-lysine and (^{3}H)DA uptake was measured 48 hours post transfection as previously reported [83,90]. Briefly, cells were rinsed and pre-incubated in KRH buffer (120 mM NaCl, 4.7 mM KCl, 2.2 mM $CaCl_2$, 1.2 mM $MgSO_4$, 1.2 mM KH_2PO_4, 0.18% glucose, 10 mM HEPES, pH 7.4) at either for 37°C for 30 min with the indicated drugs. 100 nM desipramine was included in all wells to block endogenous NET activity. Uptake was initiated by adding 1.0 µM (^{3}H)DA (dihydroxyphenylethylamine 3,4-(ring-2,5,6,-^{3}H), Perkin Elmer) containing 10^{-5} M pargyline and 10^{-5} M ascorbic acid. Assays proceeded for 10

min (37°C) and were terminated by rapidly washing cells with ice-cold KRH buffer. Cells were solubilized in scintillation fluid and accumulated radioactivity was determined by liquid scintillation counting in a Wallac Microbeta scintillation plate counter. Non-specific uptake was defined in the presence of 10 μM GBR12909 and averaged <5% of total counts measured. Data analysis was performed using Microsoft Excel and GraphPad Prism Software.